# Chapter 5

# MR/Air Mount Development and Modeling

## 5.1 The Air Spring as a Shock Isolator

An air spring is essentially a sealed pressure vessel, which typically consists of a rubber bladder that is used to contain a volume of pressurized gas. This contained volume of pressurized gas is then used to support a load. The bladder adds little to the overall stiffness of the device and the resulting overall stiffness is almost entirely due to the gas column. Due to its high compressibility the trapped column of gas is inherently low in stiffness and the resulting overall stiffness of the air spring is very low. While the stiffness is low, the air spring is capable of supporting significant loads, thus the natural frequency of the device is very low. This property makes an air springs an ideal vibration isolators.

Furthermore, being essentially a low frequency spring the acceleration transmissibility of an air mount at high frequencies is very low. As a typical ship shock input is relatively high in frequency content the air mount acts as an excellent isolator for this type of input. This is best shown by example. Figure 5.1 shows the response of an isolated mass in terms of absolute acceleration in g's when mounted on a 2 Hz air spring subject to a Floating Shock Platform (FSP) inner bottom input. Figure 5.2 shows the response of the same system to the same input in terms of relative displacement across the mount.

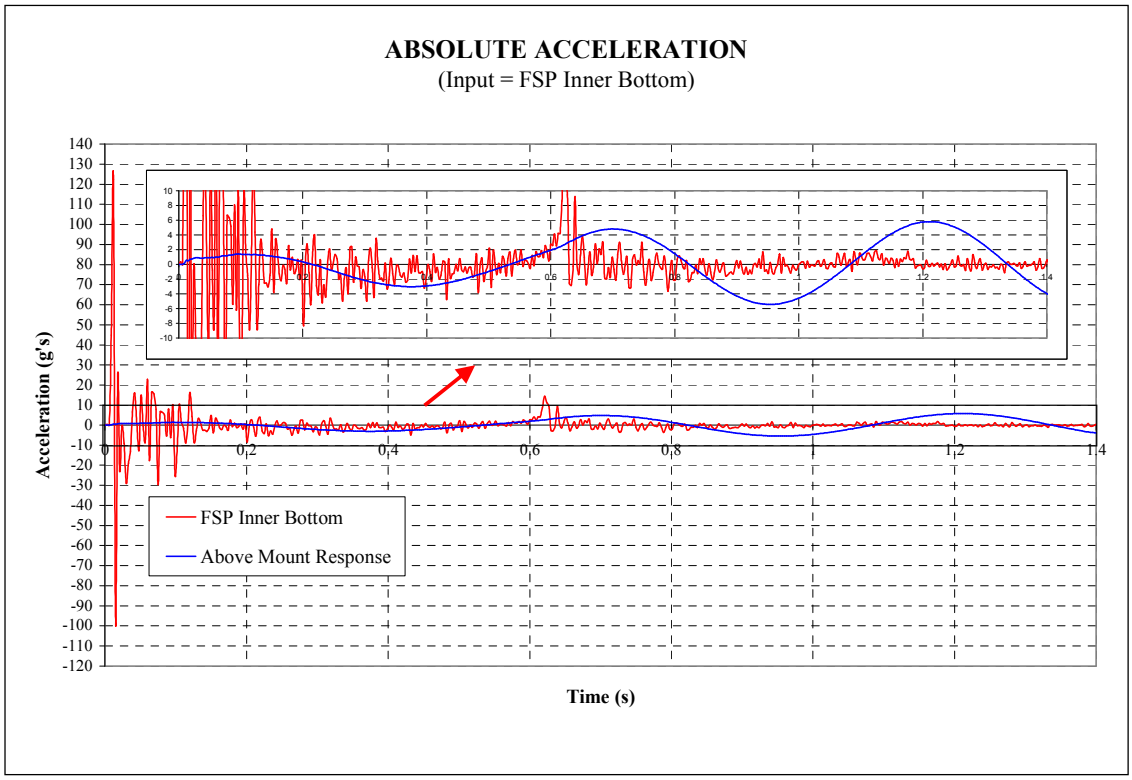


**Figure 5.1**: Absolute Acceleration Response of Equipment on a 2 Hz Air Spring

From Figure 5.1 it is clear that the air spring alone does an excellent job of isolating the simulated equipment. The 5.8 g peak acceleration is sufficient for even the most fragile COTS equipment. The problem arises when you consider Figure 5.2. To achieve the 5.8 g peak acceleration requires that the mount deflect 27.4 inches peak-to-peak. Clearly this large of a displacement is unacceptable and certainly wouldn't be achievable with a typical air spring. What is happening here is that the shock input has excited the mount resonance. Being a low frequency spring the mount in resonance undergoes a large deflection. However, it should be noted that in the early time before the mount has gone into resonance the air spring is an excellent isolator both in terms of transmitted acceleration and mount deflection.

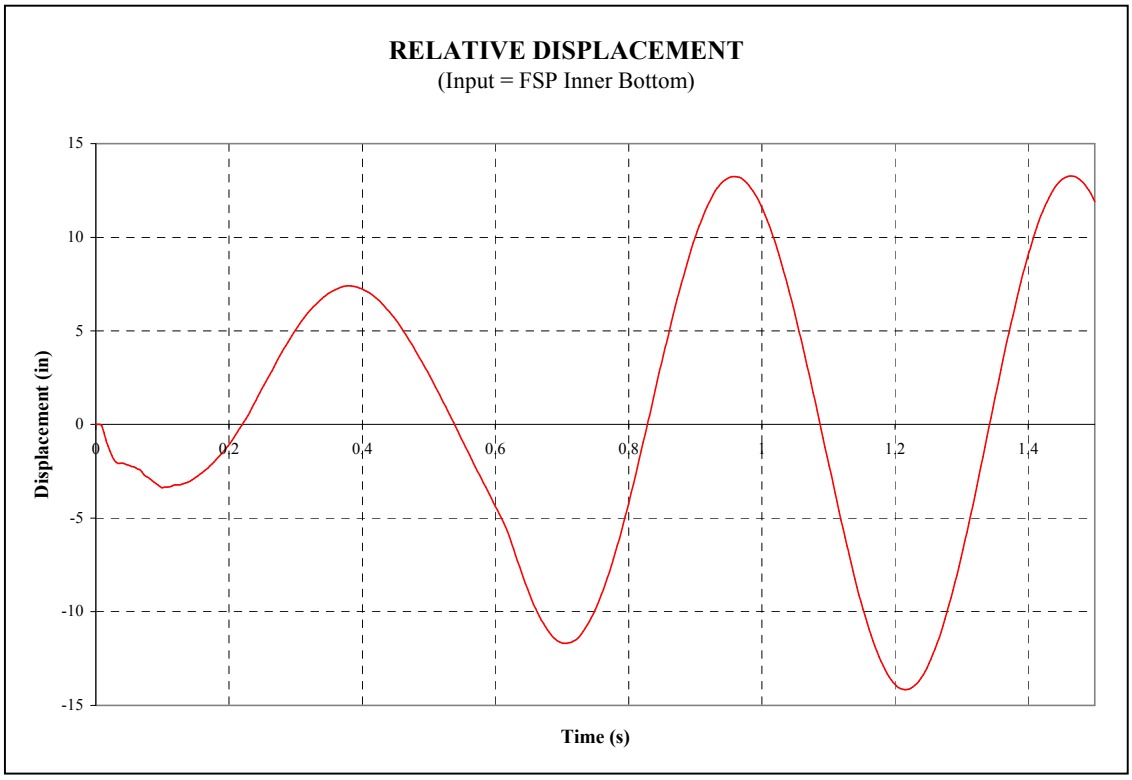


**Figure 5.2**: Relative Displacement of a 2 Hz Air Spring

A first though might be to add a passive damper in an effort to minimize the mount deflections at resonance. The results of adding a passive damper are shown in Figures 5.3 and 5.4.

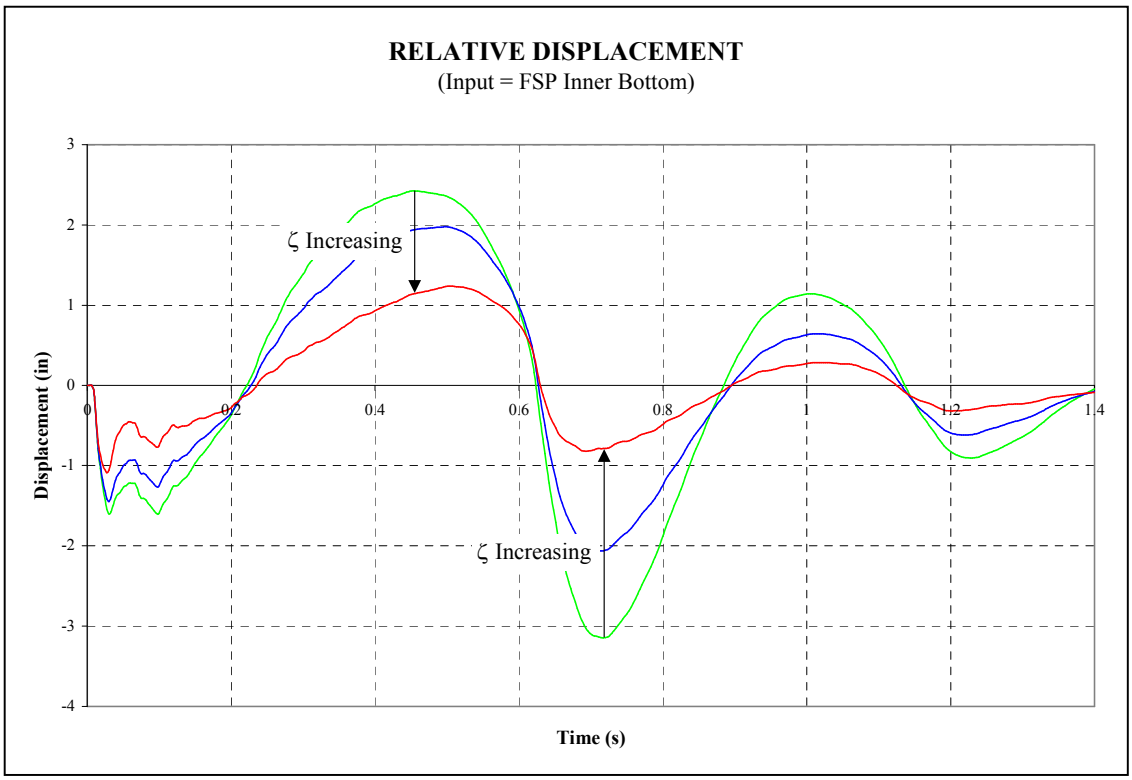


**Figure 5.3**: The Effect of Adding Passive Damping to an Air Spring (Displacement)

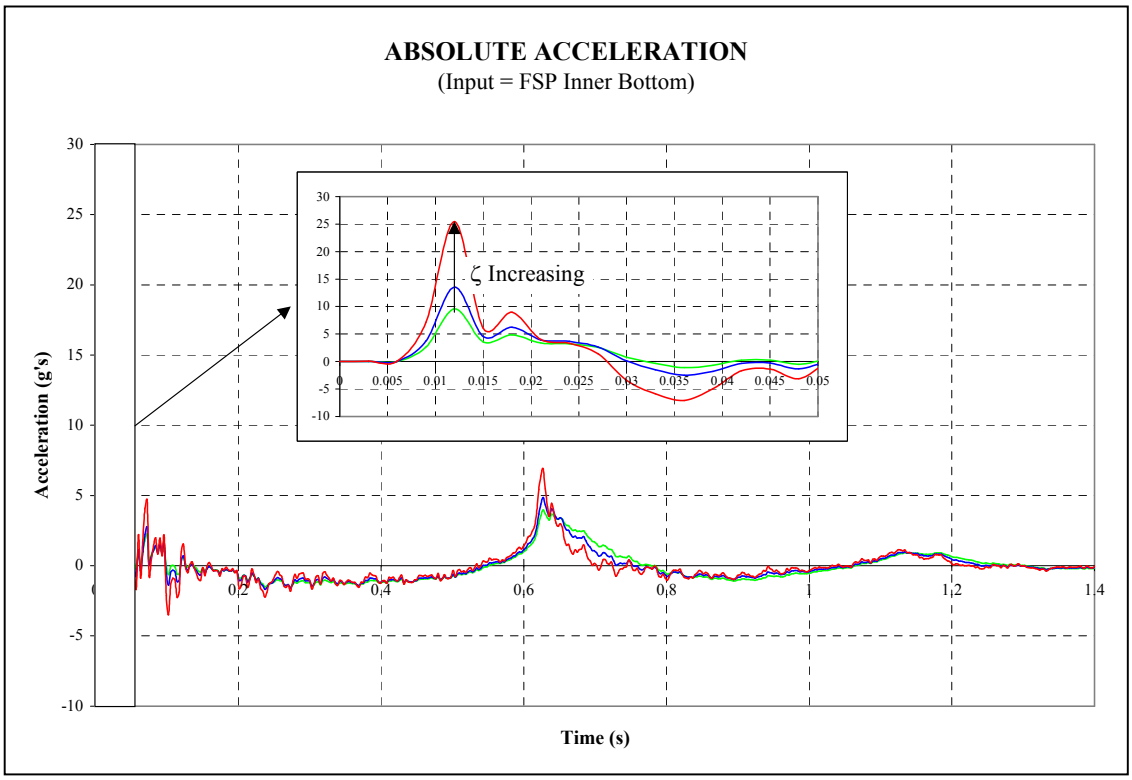


**Figure 5.4**: The Effect of Adding Passive Damping to an Air Spring (Acceleration)

Figure 5.3 shows that adding passive damping does indeed decrease the mount deflections, but as indicated in Figure 5.4 it does so at the cost of increased above mount accelerations. Looking at both figures, to achieve an approximately one inch mount deflection by adding a passive damper results in an above mount acceleration of approximately 25 g's. In most shipboard applications a 25 g above mount response would be unacceptable, but even better performance (actually nearly mathematically optimal performance), can be achieved through the use of a controllable damper in parallel with an air spring. Section 5.2 discusses the development and testing of an isolation system using this concept.

## 5.2 Developing the System Model

To simulate an actual shipboard isolation problem, the model under consideration will be that of an electronic equipment cabinet which consists of an external shell hard-mounted to a ship deck and an internal isolated equipment rack. Note that this is a typical arrangement for shipboard electronic equipment. This model will look at isolation from vertical inputs only and hence can be modeled as single-degree-of-freedom (SDOF). The isolation system under consideration will be modeled as four MR dampers and a single air spring.

To investigate the effectiveness of an air spring/MR damper combination as a combined isolation system requires an accurate model of the highly nonlinear MR damper. One such model that very accurately predicts the response of the MR damper is the so-called Bouc-Wen model. For this numerical study, the MR damper under consideration will be a commercially available model developed by the Lord Corporation (Lord Model RD-1003) which has been adequately characterized in several papers [8, 10, 22-26, 35]. The air spring under consideration is also a commercially available model manufactured by Firestone (Firestone Model 20). The air spring was chosen as its physical dimensions and capacity was a good match for the MR damper. The force-deflection behavior of the air spring was provided by Firestone and incorporated into the

model. It should be noted that over the deflection range of interest the air spring is very nearly linear and therefore will be modeled as a linear spring. The weight of the isolated equipment is 977 lbs. and the natural frequency of the air spring with a 977 lb load is 2.27 Hz. The natural frequency was derived from catalog values for the Firestone air spring with an internal pressure of 50 psig. The complete SDOF model is shown in Figure 5.5.

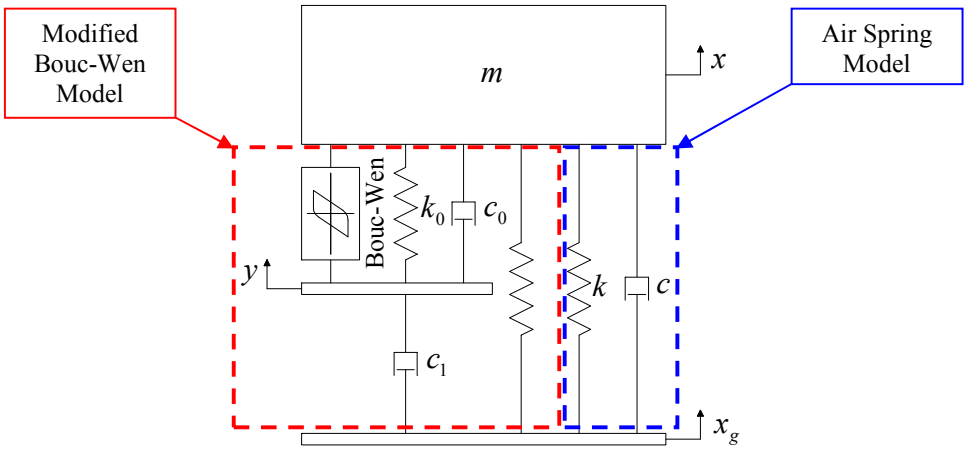


**Figure 5.5**: SDOF System Model

The MR damper imparts a force $f$ on the isolated mass. Therefore, the free-body diagram of the system is as shown in Figure 5.6.

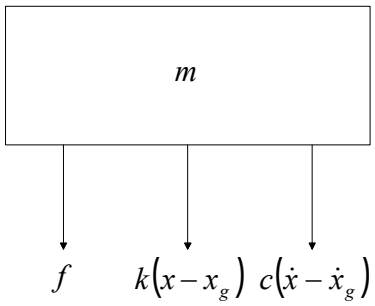


**Figure 5.6**: System Free-Body Diagram

Mathematically the force $f$ applied by the MR damper can be described using the Modified Bouc-Wen model as follows:

$$f = \alpha z + c_0\left(\dot{x} - \dot{y}\right) + k_0\left(x - y\right) + k_1\left(x - x_g\right) \tag{5.1}$$

$$c_1\left(\dot{y} - \dot{x}_g\right) = \alpha z + c_0\left(\dot{x} - \dot{y}\right) + k_0\left(x - y\right) \tag{5.2}$$

$$\dot{z} = -\gamma\left|\dot{x} - \dot{y}\right|z\left|z\right|^{n-1} - \beta\left(\dot{x} - \dot{y}\right)\left|z\right|^n + A\left(\dot{x} - \dot{y}\right) \tag{5.3}$$

Furthermore, to account for the dependence of the damper force on the voltage to the current driver and the resulting magnetic circuit, Spencer, *et al.* [8, 10, 22-26, 35] has suggested the following:

$$\alpha = \alpha_a + \alpha_b u \tag{5.4}$$

$$c_1 = c_{1a} + c_{1b} u \tag{5.5}$$

$$c_0 = c_{0a} + c_{0b} u \tag{5.6}$$

where $u$ is given by

$$\dot{u} = -\eta\left(u - v\right) \tag{5.7}$$

and $v$ is the command voltage sent to the current driver. The parameters used in Equations 5.1 to 5.7 were determined experimentally by Spencer, *et al.* [8, 10, 22, 24] and are as shown in Table 5.1.

| PARAMETER | VALUE | PARAMETER | VALUE |
|---|---|---|---|
| $c_{0a}$ | 8 N·s/cm | $\alpha_a$ | 100 N/cm |
| $c_{0b}$ | 6 N·s/cm·V | $\alpha_b$ | 450 N/cm·V |
| $c_{1a}$ | 290 N·s/cm | $\gamma$ | 363 $cm^{-2}$ |
| $c_{1b}$ | 5 N·s/cm·V | $\beta$ | 363 $cm^{-2}$ |
| $k_0$ | 50 N/cm | $A$ | 301 |
| $k_1$ | 12 N/cm | $n$ | 2 |
| $\eta$ | 190 $s^{-1}$ | | |

**Table 5.1**: Parameters for the MR Damper Model

It is desirable that the plant model be developed in state-space, but for modeling purposes it is unnecessary to develop a state-space model of the MR damper. The equations of motion describing the plant can be derived by considering the free-body diagram in Figure 5.6. Applying Newton's 2nd Law to the mass yields,

$$\overset{+x}{\uparrow} \sum F_m = -k\left(x - x_g\right) - c\left(\dot{x} - \dot{x}_g\right) - f = m\ddot{x} \tag{5.8}$$

which can be rewritten in terms of relative motion with respect to ground through the substitution,

$$x_r = x - x_g \tag{5.9}$$

as,

$$m\ddot{x}_r + c\dot{x}_r + kx_r = -m\ddot{x}_g - f \tag{5.10}$$

Dividing through by $m$ and substituting $c/m = 2\zeta\omega$ and $k/m = \omega^2$ gives,

$$\ddot{x}_r + 2\zeta\omega\dot{x}_r + \omega^2 x_r = -\ddot{x}_g - f/m \tag{5.11}$$

To convert Equation (5.11) to state-space form, let

$$x_1 = x_r \tag{5.12}$$

$$x_2 = \dot{x}_r \tag{5.13}$$

and substitute into Equation (5.11) resulting in,

$$\dot{x}_2 = -2\zeta\omega x_2 - \omega^2 x_1 - \ddot{x}_g - f/m \tag{5.14}$$

and from Equations (5.12) and (5.13),

$$\dot{x}_1 = x_2 \tag{5.15}$$

or, in matrix form,

$$\begin{Bmatrix} \dot{x}_1 \\ \dot{x}_2 \end{Bmatrix} = \begin{bmatrix} 0 & 1 \\ -\omega^2 & -2\zeta\omega \end{bmatrix} \begin{Bmatrix} x_1 \\ x_2 \end{Bmatrix} + \begin{bmatrix} 0 \\ -1/m \end{bmatrix} f + \begin{bmatrix} 0 \\ -1 \end{bmatrix} \ddot{x}_g \tag{5.16}$$

or,

$$\dot{\mathbf{x}} = A\mathbf{x} + B_0 f + E\ddot{x}_g \tag{5.17}$$

Equation (5.16) can also be written in a more compact form by combining $f$ and $\ddot{x}_g$ into a single input vector,

$$\begin{Bmatrix} \dot{x}_1 \\ \dot{x}_2 \end{Bmatrix} = \begin{bmatrix} 0 & 1 \\ -\omega^2 & -2\zeta\omega \end{bmatrix} \begin{Bmatrix} x_1 \\ x_2 \end{Bmatrix} + \begin{bmatrix} 0 & 0 \\ -1 & -1/m \end{bmatrix} \begin{Bmatrix} \ddot{x}_g \\ f \end{Bmatrix} \tag{5.18}$$

or,

$$\dot{\mathbf{x}} = A\mathbf{x} + B\mathbf{v} \tag{5.19}$$

Since the output parameters of interest are the relative displacement across the isolation system and the absolute acceleration of the mass (isolated equipment), the output equation becomes,

$$\begin{Bmatrix} x_r \\ \ddot{x} \end{Bmatrix} = \begin{bmatrix} 1 & 0 \\ -\omega^2 & -2\zeta\omega \end{bmatrix} \begin{Bmatrix} x_1 \\ x_2 \end{Bmatrix} + \begin{bmatrix} 0 & 0 \\ 0 & -1/m \end{bmatrix} \begin{Bmatrix} \ddot{x}_g \\ f \end{Bmatrix} \tag{5.20}$$

or,

$$\mathbf{y} = C\mathbf{x} + D\mathbf{v} \tag{5.21}$$

## 5.3 Control Algorithm Investigation

Several control algorithms for the MR damper were initially investigated in terms of their shock isolation effectiveness. The algorithms considered were control based on Lyapunov Stability Theory, Modulated Homogeneous Friction, Decentralized Bang-Bang control and Linear Quadratic Regulator Optimal control. These algorithms were chosen as they had been proven effective in seismic isolation systems in previous work [23-32, 34-36, 40, 47-51]. As nonlinear control is not an area of expertise of the author, the following brief discussion of the Lyapunov, Modulated Homogeneous Friction and Decentralized Bang-Bang nonlinear controllers borrows heavily from the work of Jansen and Dyke [35,36]. Furthermore, the implementation and modeling of these controllers was done with considerable input from Mr. Michael Mosher of Taylor Devices, Inc. The LQR Optimal Controller will be discussed in the Section 5.3.4.

## 5.3.1 Lyapunov Controller

The Lyapunov controller applies Lyapunov's direct approach to stability analysis to the design of a feedback controller [91]. This approach requires the use of a Lyapunov function $V(\mathbf{z})$, which is a positive definite function of the system states $\mathbf{z}$. According to Lyapunov stability theory, if the rate of change of the Lyapunov function is negative semi-definite, the origin is stable in the sense of Lyapunov. Thus the goal of the Lyapunov controller is to select a control input that will make the Lyapunov function as negative as possible. Leitmann [92] applied Lyapunov's direct approach to the design of a semi-active controller. Leitmann chose a Lyapunov function of the form

$$V(\mathbf{z}) = \frac{1}{2}\|\mathbf{z}\|_P^2 \tag{5.22}$$

where $\|\mathbf{z}\|_P$ is the P-norm of the states defined by

$$\|\mathbf{z}\|_P = [\mathbf{z}'\mathbf{P}\mathbf{z}]^{1/2} \tag{5.23}$$

and $\mathbf{P}$ is a real, symmetric, positive definite matrix. The matrix $\mathbf{P}$ is found using the Lyapunov equation, and the control law that will minimize the Lyapunov function is

$$v_i = V_{\max} H(-\mathbf{z}'\mathbf{P}\mathbf{B}_i f_i) \tag{5.24}$$

where $V_{\max}$ is the maximum voltage applied to the current driver for the MR damper, $H(\cdot)$ is the Heaviside step function, and $f$ is the force applied by the damper.

## 5.3.2 Modulated Homogeneous Friction Controller

The Modulated Homogeneous Friction (MHF) controller was proposed by Inaudi [34]. The concept behind the MHF controller is that at every occurrence of a local extrema in the deformation of the MR damper, i.e., when the relative velocity between the ends of the damper is zero, the normal force applied at the frictional interface is updated to a new value. At each local minima or maxima in the deformation, the normal force, $N(t)$, is chosen to be proportional to the absolute value of the deformation of the MR damper. The control becomes

$$N(t) = g|P[\Delta(t)]| \tag{5.25}$$

where $g$ is a positive gain and the prior-local-peak operator $P[\cdot]$ is defined as

$$P[\Delta(t)] = \Delta(t-s) \tag{5.26}$$

where,

$$s = \{\min x \geq 0 : \dot{\Delta}(t-x) = 0\} \tag{5.27}$$

and $\Delta(t-s)$ is the most recent local extrema in the deformation.

Since this algorithm was developed for use with a variable friction device, the following modifications were necessary to implement it with an MR damper: 1) There is no need to check if the force is greater than $\mu N(t)$, where $\mu$ is the coefficient of friction, since the MR damper is not subject to static friction, and 2) A force feedback loop was used to induce the MR damper to produce an approximate frictional force that corresponds to the desired normal force. Therefore, the goal is to generate a control force with a magnitude of

$$f_n = \mu g \left| P\left[\Delta(t)\right] \right| = g_n \left| P\left[\Delta(t)\right] \right| \tag{5.28}$$

where the constant of proportionality $g_n$ has units of stiffness. The resulting control law is

$$v = V_{\max} H\left(f_n - |f|\right) \tag{5.29}$$

An appropriate choice of $g$ will keep the force $f_n$ within the operating envelope of the MR damper a majority of the time, allowing the force applied by the MR damper to closely approximate the desired force. It should be noted that implementing this controller only requires a measure of the applied force and the relative displacement of the damper.

## 5.3.3 Decentralized Bang-Bang Controller

The Decentralized Bang-Bang controller uses an approach that is similar to that used by McClamroch and Gavin [93]. Using this approach a Lyapunov function is chosen to represent the total vibration energy in the system, i.e., kinetic energy plus potential energy, or

$$V = \frac{1}{2}\mathbf{x}'\mathbf{K}_s\mathbf{x} + \frac{1}{2}\left(\dot{\mathbf{x}} + \Gamma\dot{x}_g\right)'\mathbf{M}_s\left(\dot{\mathbf{x}} + \Gamma\dot{x}_g\right) \tag{5.30}$$

Using an approach that is similar to that used in the design of the Lyapunov controller the resulting control law that will minimize the Lyapunov function is

$$v_i = V_{\max} H\left[-\left(\dot{\mathbf{x}} + \Gamma\dot{x}_g\right)'\Lambda_i f_i\right] \tag{5.31}$$

It should be noted this control law only requires measurement of the relative velocity of the isolated mass and the applied control force.

## 5.3.4 Linear Quadratic Regulator Optimal Controller

Many control algorithms have been suggested in the literature [23-32, 35, 36, 44-51, 56, 57] for the semi-active control of MR dampers. Based on the results of [95, 96] the LQR Optimal Control Algorithm will be used in the simulations as the LQR algorithm showed considerable promise in attenuating ship shock inputs. The basic idea behind the LQR algorithm is the following. Using Linear Quadratic Regulator (LQR) optimal control an optimal control (damper) force can be calculated. This calculated control force is optimal with respect to some cost function as will be discussed later. The problem with the MR damper is that the damper force cannot be specified, only the voltage applied to the current driver. A clever method to get around this problem was suggested by *Spencer, et al*. [23]. *Spencer* suggested the following logic:

- If the actual damper force is less than the optimal damping force AND the Forces have the SAME sign then the voltage applied to the current driver is set to the maximum voltage.
- If the actual damper force equals the optimal damper force then the voltage applied to the current driver remains at the present level.
- Otherwise the voltage applied to the current driver is set to zero.

Mathematically this logic can be described as,

$$v = V_{\max} H\{(f_{opt} - f) f\} \tag{5.32}$$

where $v$ is the applied voltage, $V_{\max}$ is the maximum voltage, $f_{opt}$ is the optimal damper force, $f$ is the measured (or calculated) damper force and $H$ is the Heaviside step function. A block diagram of the control system is shown in Figure 5.7.

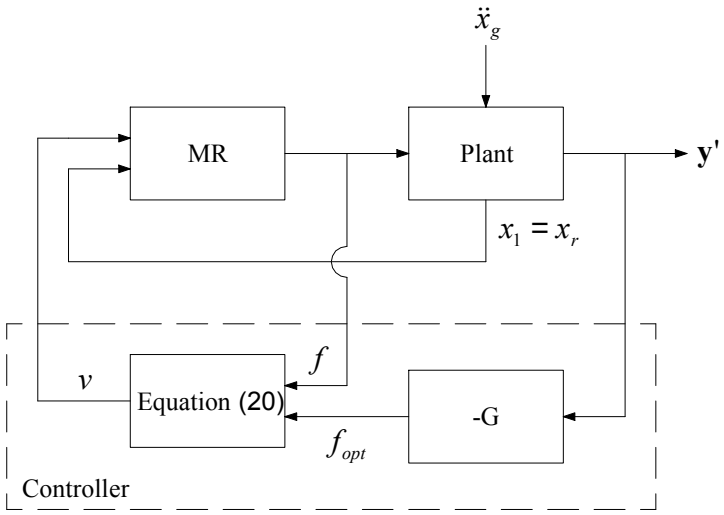


**Figure 5.7**: LQR Optimal Control System Block Diagram

LQR allows the control designer to determine a set of optimal gains that will minimize a user defined cost function. The cost function can be written in terms of the output which allows the designer to explore trade-offs between the actual output and/or the control effort (damper force). Mathematically the cost function to be minimized is,

$$V = \int_0^\infty \mathbf{Q} y^T y + \mathbf{R} u^T u \, dt \tag{5.33}$$

where $y$ is the output (in this case chosen to be the relative displacement across the mount and the above mount absolute acceleration), $u$ is the damper force, $\mathbf{Q}$ is the 2×2 output weighing matrix and $\mathbf{R}$ is the control weighting matrix (a scalar in this application). The calculated optimal gains minimize this cost function. By varying $\mathbf{Q}$ and $\mathbf{R}$ the designer can effectively tune the isolation system to minimize, or explore trade-offs between, the relative displacement across the isolation system, the absolute

acceleration of the isolated mass and/or the damper force. This allows the isolation system to be tuned to minimize a parameter of interest, or re-tuned to account for variations in isolated mass and/or center of gravity of the isolated mass. The former is useful in developing the optimal isolation system for a given piece of equipment and the later is useful for equipment cabinets that contain equipment that has been replaced and/or upgraded. With an 18 month typical refresh for electronic equipment it is certain that the isolation system for an equipment rack will need to be re-evaluated and/or replaced many times during its lifetime.

Note that the controller can only control the damper force, not the base excitation. Therefore, the optimal damper force will be calculated assuming the damper force is the only input to the isolated mass. The optimal gain vector was calculated using the MATLAB® function lqry.m which calculates the optimal gains using output weighing. The specific output and control weighing matrices used were,

$$\mathbf{Q} = \begin{bmatrix} 800000 & 0 \\ 0 & 1 \end{bmatrix} \qquad (5.34)$$
$$\mathbf{R} = 0.3$$

These weighing matrices were determined by roughly weighing the above mount acceleration and mount deflection equally and then fine tuning the matrix values by trial and error to optimize the isolation performance. The MATLAB program used to calculate the gains is shown in Appendix A. Running the program resulted in the following output,

```
» mrairfsf
Enter (1) for analog, (2) for digital -> 1
G =
 -873.7542  -72.8961
```

Therefore, the gain vector used was,

$$\mathbf{G} = \begin{bmatrix} -873.7542 & -72.8961 \end{bmatrix} = \begin{bmatrix} g_1 & g_2 \end{bmatrix} \tag{5.35}$$

Once the optimal gain vector $\mathbf{G}$ is known, the optimal damping force can be calculated from,

$$f_{opt} = \mathbf{G}\mathbf{x} = g_1 x_1 + g_2 x_2 \tag{5.36}$$

which can then be used with the measured (or calculated) damper force and Equation (5.32) to determine the input voltage $v$ to the current driver. The damper force can be measured, or calculated from the equations of motion using,

$$f = m\left(\ddot{x} + 2\zeta\omega\,\dot{x}_r + \omega^2 x_r\right) \tag{5.37}$$

Calculating the damper force is preferable as no means for measuring the actual damper force is then necessary which would lead to the need for additional sensors. It should be noted that calculating the damper force is straightforward in the SDOF case, but would be more difficult in the multi-degree-of-freedom case.

## 5.3.5 Controller Performance Evaluation

To evaluate the shock isolation performance of the four control algorithms discussed above with "ship-like" shock inputs a simulation was performed with the SDOF model. The simulations were performed in MATLAB® using the code shown in Appendix A. The base input to the model was derived from the response of a 13 Hz deck fixture on the Floating Shock Platform (FSP). In order to avoid driving the damper past its stroke limit of ±1.00 in (±2.54 cm), the input to the model was scaled to provide a 1g peak input in terms of acceleration units. The scaled input expressed in terms of velocity is shown in Figure 5.8.

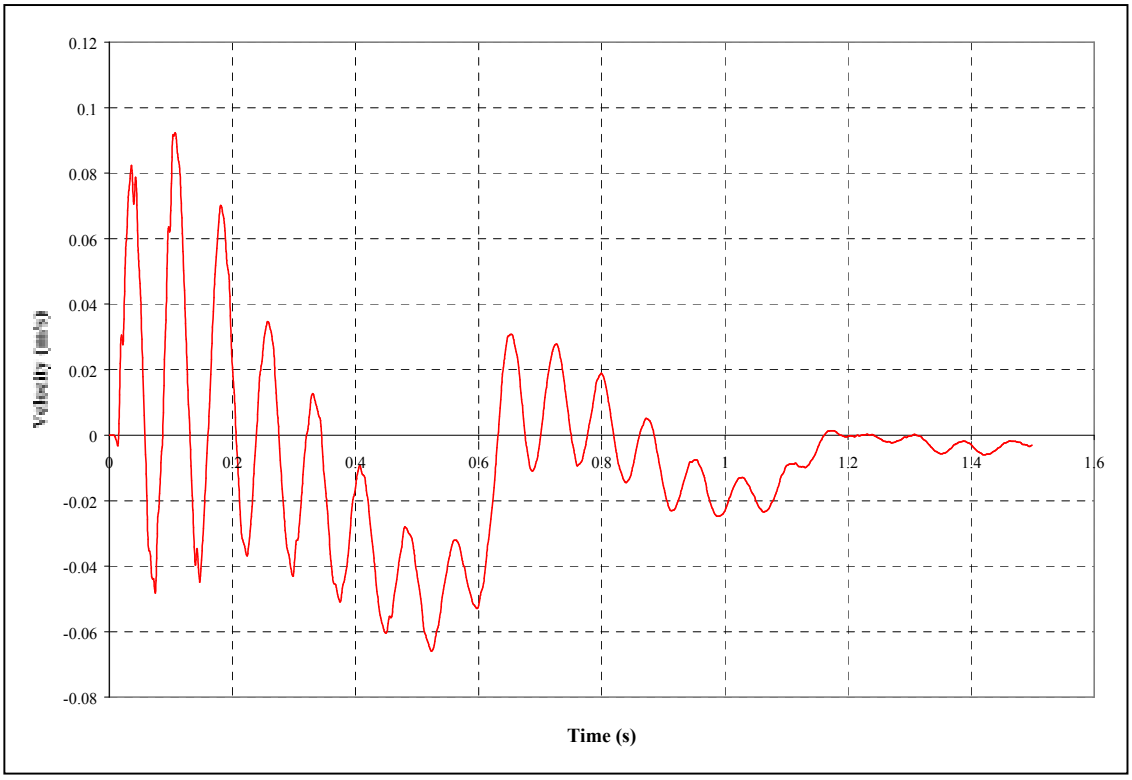


**Figure 5.8**: Scaled Base Input Used in Algorithm Comparison Simulations

In shipboard isolation systems the performance parameters of interest are typically the above mount absolute acceleration and the relative displacement across the mount. The former is of interest as this represents the acceleration level to which the isolated equipment or structure is subjected. The later is of interest as it represents the mount deflection which is critical due to rattle space requirements. The simulation results are shown below. Figure 5.9 shows the absolute acceleration for each of the control algorithms considered and the air spring without additional damping. Figure 5.10 shows the relative displacement across the mount for the same cases.

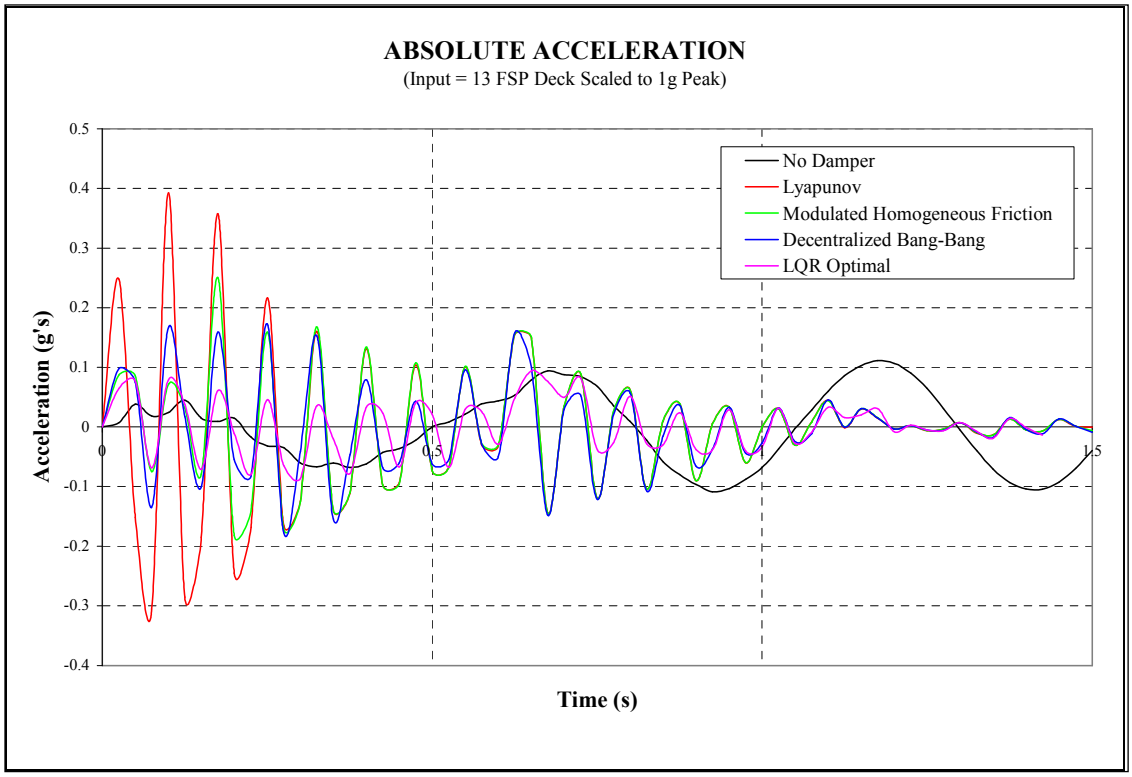


**Figure 5.9**: Controller Acceleration Response Comparison

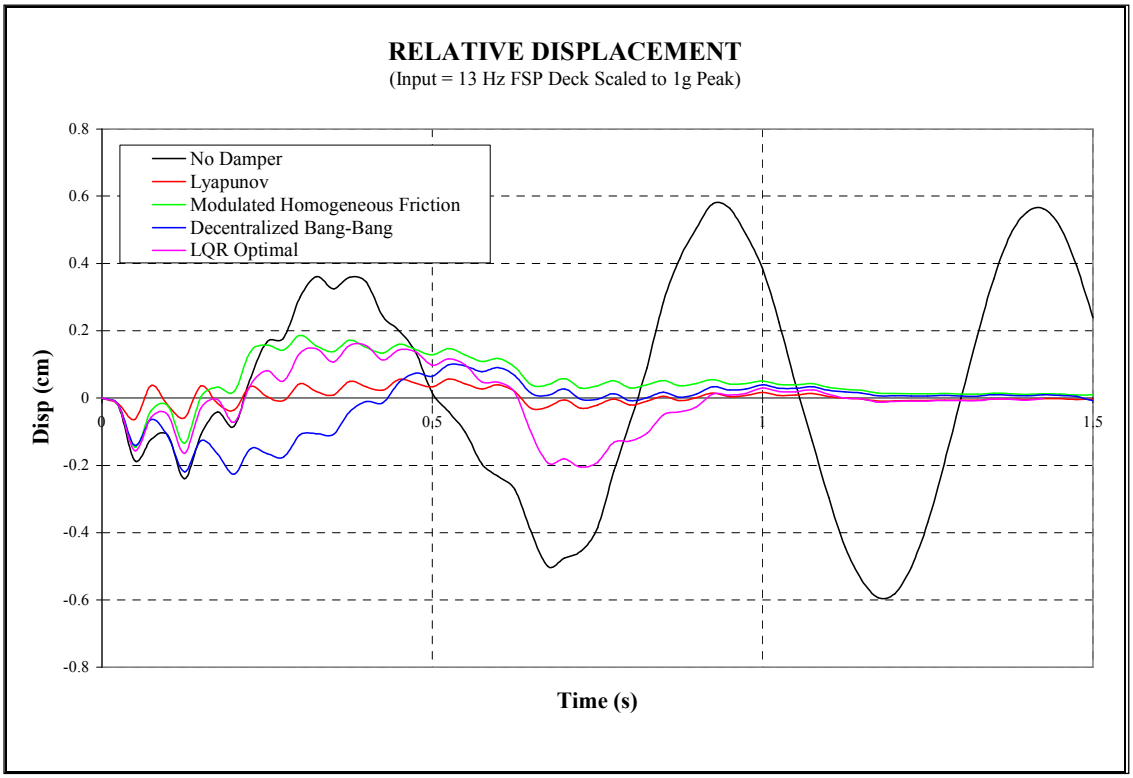


**Figure 5.10**: Controller Displacement Response Comparison

From the figures it is clear that the air spring without additional damping provides excellent shock isolation, but the shock event excites the mount resonance resulting in considerable relative displacement. Using the Lyapunov controller resulted in a significant decrease in relative displacement, but it does so at the expense of significantly increased above mount accelerations. The Modulated Homogeneous Friction and Decentralized Bang-Bang controller offered similar mediocre performance. The best performance in terms of minimizing both absolute acceleration and relative displacement was achieved with the LQR Optimal controller. The LQR Optimal Controller achieved above mount acceleration levels that were lower that the air spring alone while still achieving reasonable relative displacement values. The peak responses for all cases are shown in Figure 5.11.

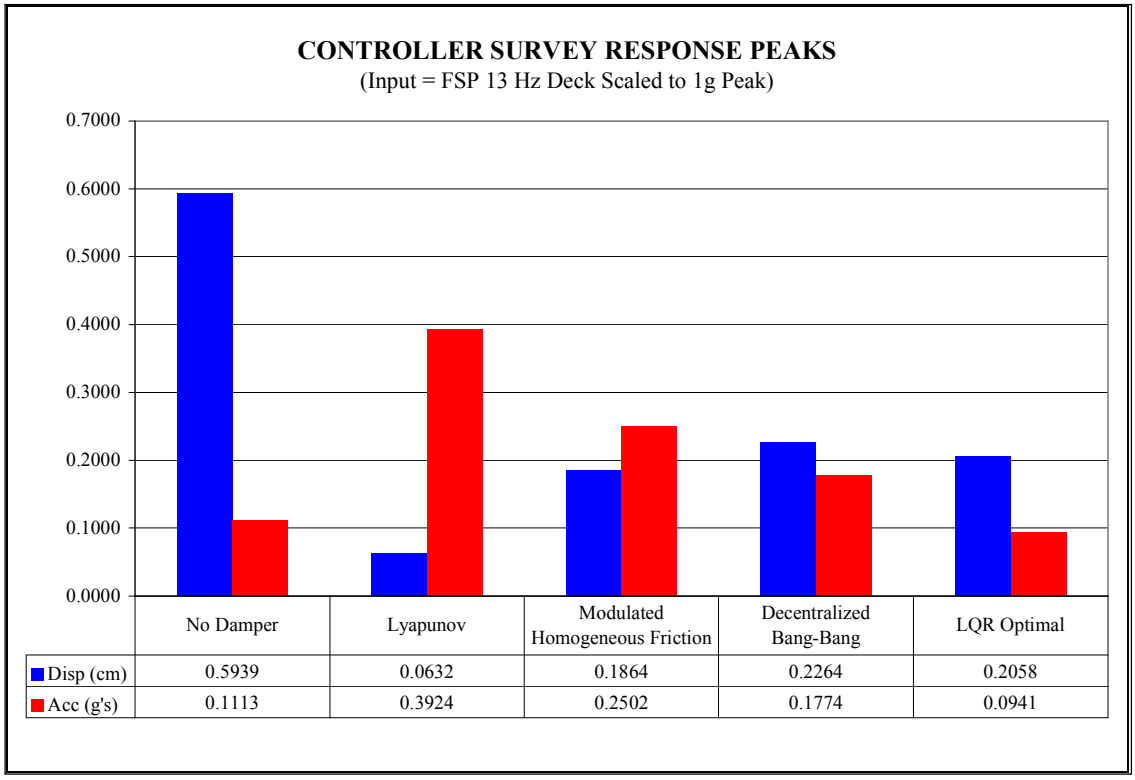


| | No Damper | Lyapunov | Modulated Homogeneous Friction | Decentralized Bang-Bang | LQR Optimal |
|---|---|---|---|---|---|
| Disp (cm) | 0.5939 | 0.0632 | 0.1864 | 0.2264 | 0.2058 |
| Acc (g's) | 0.1113 | 0.3924 | 0.2502 | 0.1774 | 0.0941 |

**Figure 5.11**: Displacement and Acceleration Peak Comparison

Another advantage to the LQR Optimal controller is the ability to trade-off performance in terms of relative displacement and above mount absolute acceleration

while maintaining a reasonable control effort in terms of damper force. This is a useful feature that allows the mount to be electronically "tuned" to a desired performance threshold. In a shipboard application, the limiting factor could be the above mount acceleration for a particularly fragile piece of isolated equipment or it could be relative displacement if particularly stringent rattle space limitations are imposed. Typically both of these performance metrics are considered.

## 5.3.6 Velocity Feedback Controller

One of the problems with the LQR optimal controller is the number of sensors required to implement it. As a minimum, the relative displacement and/or velocity across the mount and the damping force must be measured. One alternative is to use an observer to estimate the required signals. While this is certainly a viable solution, another alternative is to use a velocity transducer to measure the relative velocity and integrate the signal to get the relative displacement. Adding an accelerometer to measure the above mount absolute acceleration permits the damping force to be calculated in real time. Unfortunately implementing this still requires a minimum of two sensors. Obviously for a production unit the number of sensors required per mount must be minimized due to the high cost of sensors. In an effort to minimize the number of sensors required, while still achieving an isolation performance similar to that achieved by the LQR optimal controller, another controller was developed by considering the energy loss per cycle in the mount. Being a relatively low cycle event, shipboard shock requires that the isolation system maximize the energy loss per cycle. The problem is that this must be done while still maintaining adequate vibration isolation performance. Thus just adding a damper that can dissipate large amounts of energy per cycle is not adequate as such a device tends to transmit a considerable amount of energy to the isolated equipment during shock inputs.

Several simple controllers were considered that could achieve a significant amount of the performance of the LQR optimal controller using only one sensor. The

best performance was achieved by feeding back a voltage to the MR damper current drivers that was proportional to the relative velocity across the mount as shown in Figure 5.12.

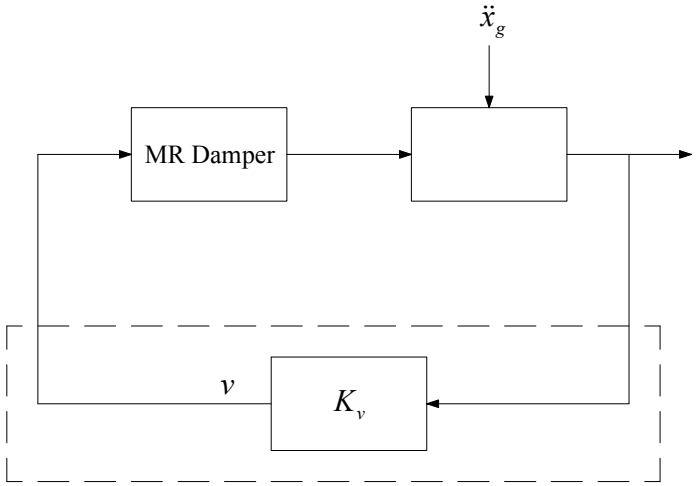


**Figure 5.12**: Velocity Feedback Control System Block Diagram

This controller only requires a measure of the relative velocity across the mount which can easily be measured with a Linear Velocity Transducer (LVT). The energy loss per cycle is plotted in Figure 5.13 for the velocity feedback and LQR optimal controllers. The damper force shown is for four MR dampers and the input is a 1.0 inch (2.54 cm) amplitude sinusoid at a frequency of 60 rad/s.

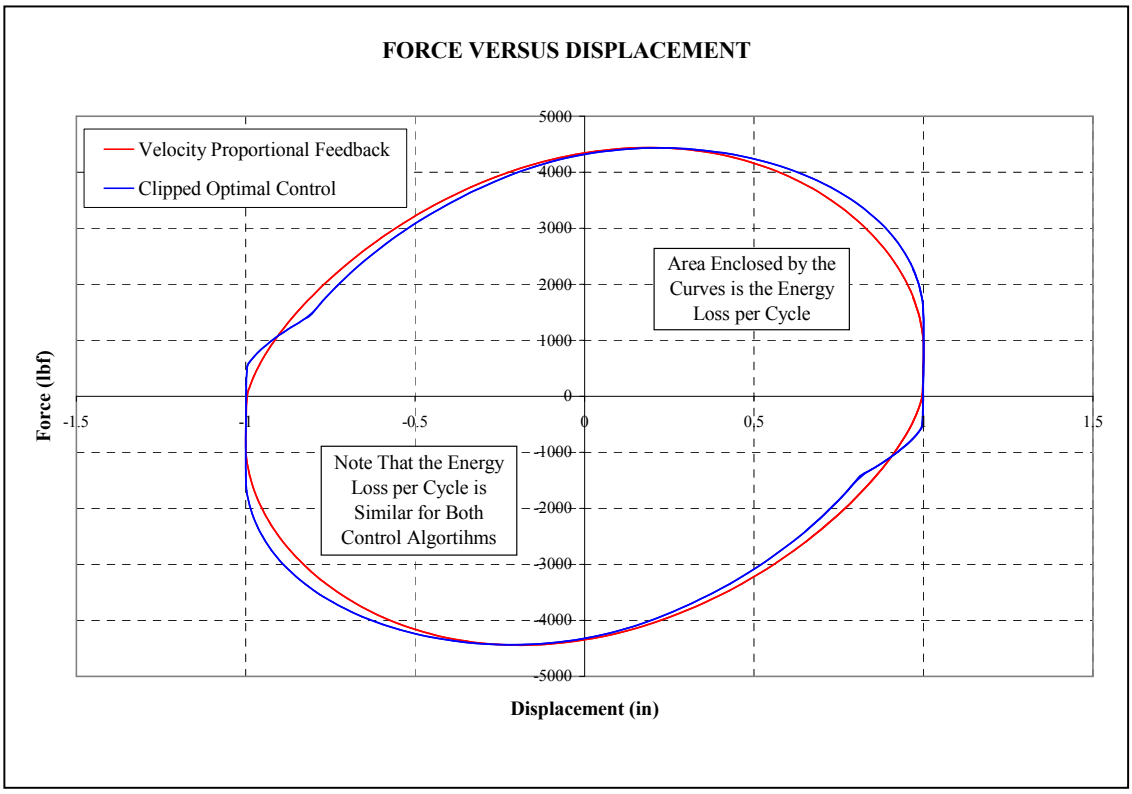


**Figure 5.13**: Comparison of Energy Loss per Cycle

Figure 5.13 shows that the energy loss per cycle is very similar for both of the controllers. The constant of proportionality (Gain $K_v$) was set to provide the peak voltage (3.75V) to the current driver at the peak estimated relative velocity. Since two drops heights were to be used in the test, two gains were determined to provide the peak voltage to the current drivers at the expected peak velocity. For the smaller of the two drops a peak velocity of 50 in/s was used and for the larger of the two drops a peak velocity of 100 in/s was used. These two particular drop heights were used in an attempt to develop base excitations that were similar in magnitude to the Floating Shock Platform (FSP) inner bottom and a typical mid-frequency FSP deck fixture. Therefore, the gain used for the smaller drop was,

$$V = K_{v_1}\dot{x} \Rightarrow K_{v_1} = \frac{V}{\dot{x}} = \frac{3.75V}{50\,in/s} = 0.075V \cdot s/in \tag{5.38}$$

and the gain used for the larger drop was,

$$V = K_{v_2}\dot{x} \Rightarrow K_{v_2} = \frac{V}{\dot{x}} = \frac{3.75V}{100\,in/s} = 0.0375V \cdot s/in \tag{5.39}$$

Therefore, for the smaller drop the voltage applied to the current driver was $V = 0.075\dot{x}$ and for larger drop the voltage applied to the current driver was $V = 0.0375\dot{x}$. The performance of this and the LQR optimal controller will be discussed in Section 6.4.

## 5.3.7 Acceleration Limiting Bang-Bang Controller

One additional controller was developed too late to be included in the shock testing to be discussed in the next section. The controller was designed by consideration of typical shipboard shock isolation goals. The goal of any shipboard shock isolation system is to minimize the mount deflection while simultaneously limiting the above mount absolute acceleration to some prescribed value. If these goals are considered a controllable damper can be programmed to provide maximum damping during a shock event to minimize mount deflection and switch to minimum damping when the above mount absolute acceleration nears some preset cut-off value. Mathematically this controller can be described as,

$$V = \begin{cases} V_{\max}, & |\ddot{x}| < A \\ 0, & |\ddot{x}| \geq A \end{cases} \tag{5.40}$$

where $V$ is the voltage applied to the MR damper current driver, $V_{\max}$ is the voltage applied to MR damper current driver that results in the peak damping force, $\ddot{x}$ is the measured above mount absolute acceleration, and $A$ is the preset maximum desired above mount acceleration.

This algorithm can be easily implemented with an MR damper and only requires an accelerometer for sensing and a simple on-off controller. In effect this controller provides the optimal performance for a shipboard shock application. The performance of this controller will be shown by simulation in Section 6.7.

# Chapter 6

# MR/Air Mount Testing and Validation

## 6.1 Shock Isolation Performance

In order to test the shock isolation performance of the subject isolation system, it was desired to develop a test method and test device that could impart a true base excitation input. Typical drop test machines do not provide a base excitation, but drop a weight onto the isolation system, or the isolated mass. While this might be acceptable for characterization testing of the mount, the resulting input is applied above mount which is contrary to the application of shock inputs in shipboard applications. There are two significant problems with the traditional drop test approach for testing this mount. First is that the resulting input is incorrect. Second, an air spring must be constantly loaded by the supported mass or the mount can blow itself apart.

In this test the desire was to provide a test condition that was most like a shipboard condition. This required providing a shock input to the base while avoiding inputs to the isolated mass. One method to accomplish this is to drop the entire mount assembly, including the isolated mass. With that in mind a new drop test fixture was designed and fabricated.

## 6.2 Drop Test Fixture Design

The drop test fixture consists of two drop weights weighing 977 lbs. (443 kg) each that are guided on two 1.5 in. (3.8 cm) diameter linear shafts by eight bearing blocks machined from one in. (2.54 cm) thick oil-filled UHWM plate. The drop weights measure 12 in. (30.5 cm) by 12 in. (30.5 cm) by 24 in. (61.0 cm) and were constructed

from four in. (10.2 cm) thick ASTM A-36 steel plate that is welded on four sides to form as close to a solid block as possible. This was done to minimize any ringing of the individual plates which could induce spurious inputs into the data. The mount to be tested is directly attached to the upper and lower drop weights by eight 5/8 in. (15.9 mm) hex head cap screws. To shock test the mount the entire assembly consisting of the two drop weights and the attached mount is picked up and dropped onto the 1.25 in. (3.18 cm) thick ASTM A-36 steel impact plate. To minimize ringing due to the impacting steel surfaces a 1/4 in. (6.35 mm) thick rubber pad was bonded to the top of the impact plate. The impact plate itself was fillet welded on four sides to a 3 in. (7.62 cm) thick ASTM A-36 steel plate which was in turn bolted to a 3 in. thick base plate using four 1.125 in. (28.6 mm) hex head cap screws. The base plate itself was leveled and welded to an existing steel plate that is imbedded into the asphalt pavement behind the Newport News Shipbuilding test facility. The drop test fixture is shown in Figure 6.1 and detailed drawings of the test fixture are shown in Appendix A.

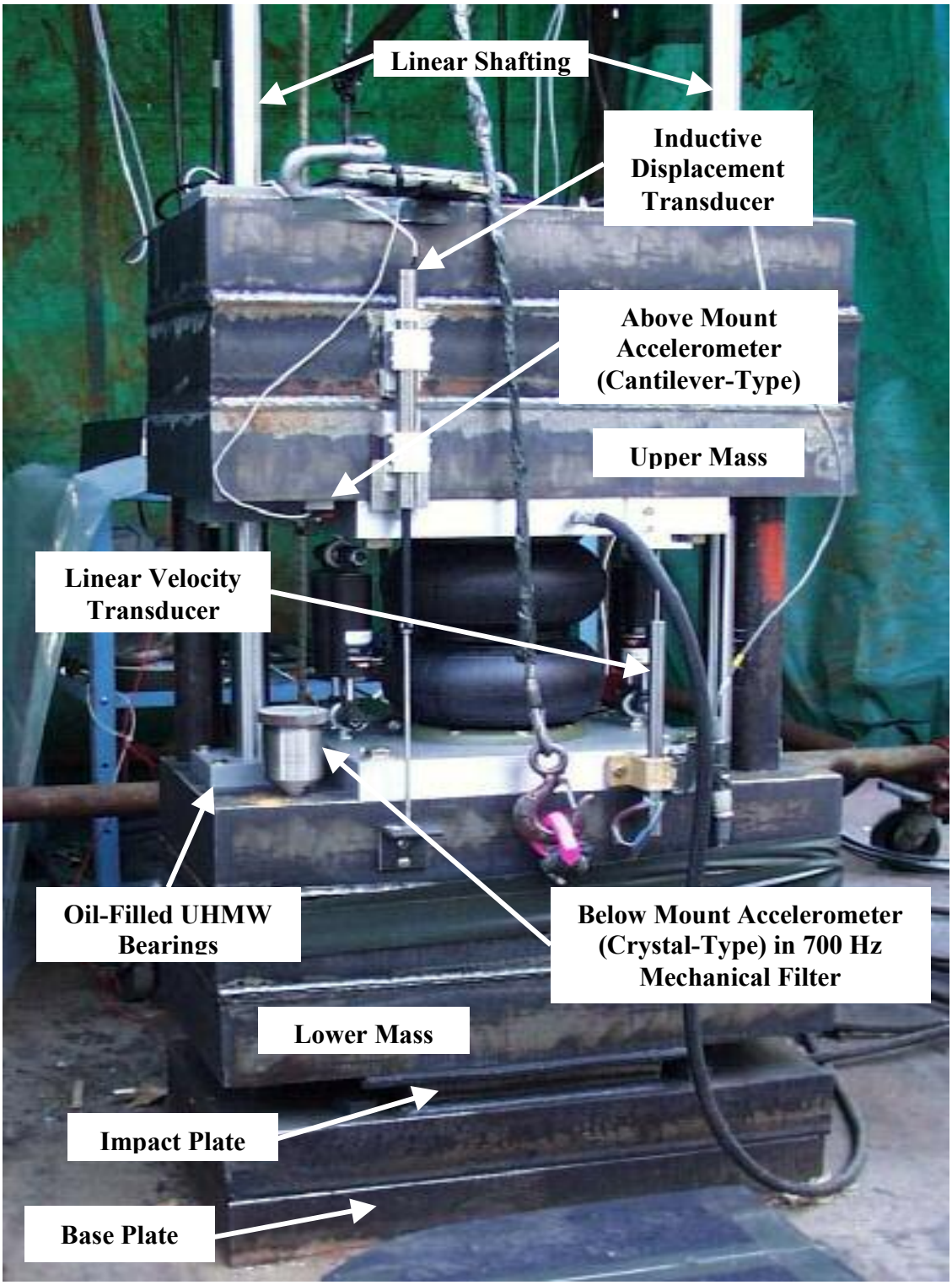


**Figure 6.1**: Drop Test Fixture Assembly

## 6.3 Drop Test Procedure

The drop tests are performed by picking up the entire mount assembly with the two attached masses using a forklift. The test arrangement is shown in Figure 6.2.

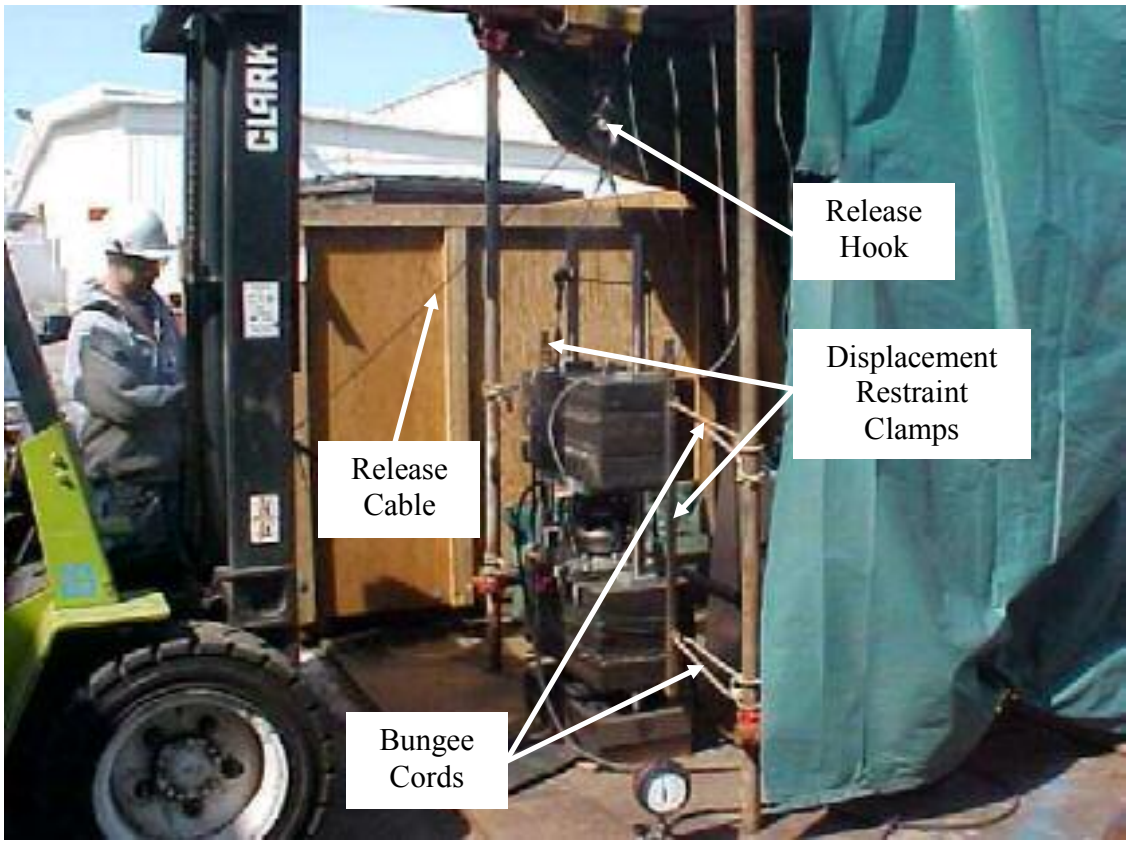


**Figure 6.2**: Drop Test Operation

The assembly is dropped using a manual release hook. During early testing it was determined that if unrestrained the air spring tended to push the two masses apart during the free fall phase of the drop. This provided an advantage to the isolation system by providing more available stroke for the dampers by effectively "cocking" the mount. The result is an unrealistic performance improvement that wouldn't occur in an actual mount application. In actual shipboard use the mount would typically be at static deflection only just prior to a shock event. In order to provide the most realistic test a displacement restraint clamp was developed that fixed the mount at zero relative displacement until impact. This was done by placing a pair of clamps from the top of the upper weight stack

to the bottom of the lower weight stack. The displacement restraint system is shown in Figure 6.2. Upon impact the mount compresses and the Bungee cords pull the clamps away from the drop weights thus allowing the mount to be excited from zero relative motion and then to oscillate freely following the initial excitation.

The mount prototype consists of an air spring in parallel with four MR dampers as shown in Figure 6.3. The dampers were mounted in pairs using ball-joint rod ends as shown in Figure 6.4. This was done to eliminate moment loading of the damper rod ends which can lead to failure of the damper rod and/or seals. Although this test was constrained to be single-degree-of-freedom, the use of ball-joint rod ends and/or skewing the dampers at an angle would allow the linear dampers to provide a multi-degree-of-freedom damping force.

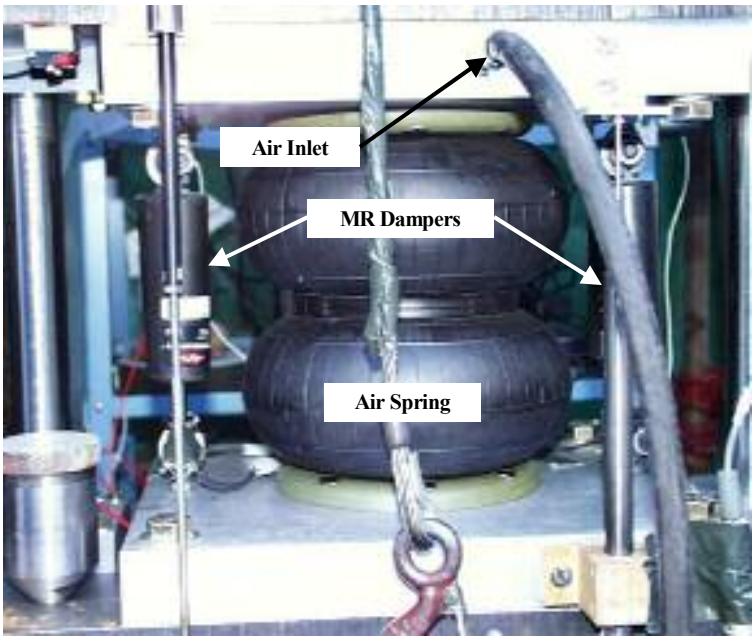


**Figure 6.3**: MR/Air Mount Technology Demonstrator

**Figure 6.4**: MR Damper Pair Detail

## 6.4 Drop Test Data Acquisition and Control Instrumentation

The control of the MR dampers, as well as the data acquisition, was performed using a dSpace digital control system based on the dSpace DS1104 PPC Controller board. The DS1104 board provides four 16 bit multiplexed A/D channels, four 12 bit A/D channels and eight 16 bit D/A channels. The dSpace ControlDesk software provides the interface between the instrumentation and the digital controller which is developed in Simulink®. MATLAB's® Real Time Workshop converts the Simulink® model to C code which is then loaded onto the dedicated real time processor (RTP) on the DS1104 board. When the controller is loaded and running on the RTP the host operating system is only used for communication between ControlDesk and the controller. This is important as the RTP can provide very high sampling rates when not burdened by the overhead of running the Windows® operating system.

The host computer was a Dell Optiplex GX400 PC with a 1.5 GHz CPU and 512 MB of RAM. Data was captured and stored initially on the PC's 40 GB hard drive and then written to CD-ROM. The data was sampled and the controller was operated at a 20 kHz sampling rate. This over-sampling was done as it was unclear what the actual duration of the shock event would be, but it was expected to be on the order of milliseconds. A 20 kHz sampling rate would give 20 samples per millisecond which seemed reasonable for capturing the shock data adequately and providing real time control of the dampers. The dSpace data acquisition and control set-up is shown in Figure 6.5.

**Figure 6.5**: dSpace Data Acquisition and Control Set-up

The interface between the dSpace equipment and the dampers and instrumentation was provided by a dSpace CLP1104 Connector Panel. The CLP1104 panel and the associated connections to the external components are shown in Figure 6.6.

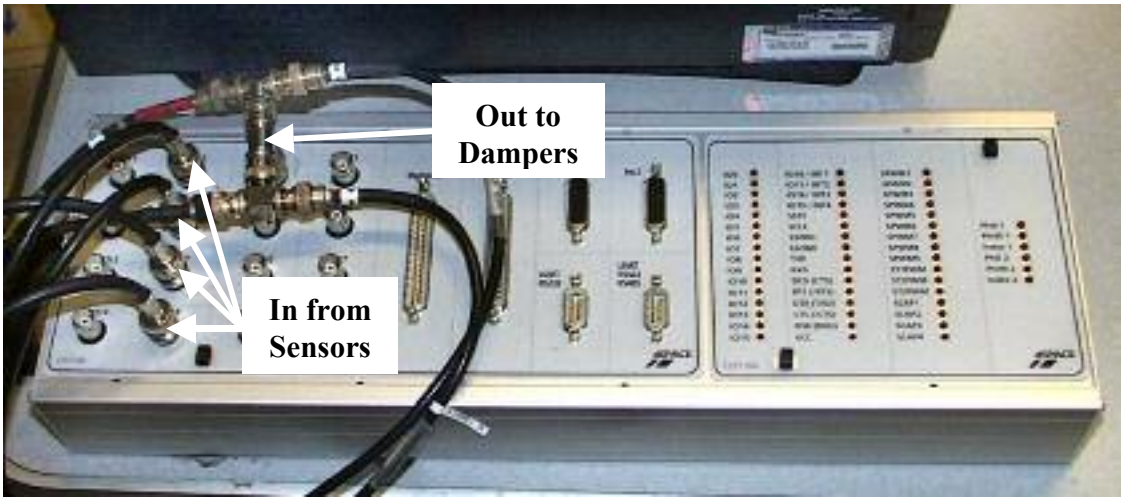


**Figure 6.6**: dSpace Connector Panel Layout

The data acquired during the test included below mount absolute acceleration (base excitation), above mount absolute acceleration and relative displacement and velocity across the mount. For control purposes the relative velocity was high pass filtered at 5 Hz and integrated to obtain relative velocity as will be explained later. The displacement transducer was used to verify the integrated velocity.

The direct displacement data was acquired using a Data Instruments Model FS4000 Inductive Displacement Transducer. Signal conditioning was provided by a Data Instruments Fastar Signal Processor. The Data Instruments inductive displacement transducer was chosen for its fast response time which has been determined to exceed traditional Linear Variable Differential Transformers (LVDTs). Relative velocity was measured directly with a TransTek Model 0113-0000 Linear Velocity Transducer (LVT). The TransTek LVT is essentially a powerful magnet attached to an extension rod which moves inside a set of coils. The motion of the magnet inside the coils induces a voltage in the coils that is proportional to the relative velocity of the magnet with respect to the coils. This allows direct measurement of relative velocity and since the LVT generates its own power it does not require additional signal conditioning. However, to more effectively control the output of the LVT the signal was routed through an Ectron Model 563H amplifier prior to entering the dSpace interface panel. This resulted in a ± 175 in/s (445 cm/s) full-scale measurement capability.

The above mount absolute acceleration, or response, was measured using an Endevco Model 7290A-30 accelerometer. The Model 7290A-30 is a cantilever-type, DC-coupled variable capacitance accelerometer capable of measuring accelerations of ±30 g. The accelerometer signal was also routed through an Ectron Model 563H amplifier resulting in a ±20 g measurement capability. This was considered adequate as simulations showed the peak expected above mount accelerations would be approximately 5 g's.

The below mount absolute acceleration, or base excitation, was measured using an Endevco Model 7701-50 piezoelectric accelerometer. The Model 7701-50 is AC-

coupled and is capable of measuring shock induced accelerations of up to 10,000 g's. Signal conditioning for the accelerometer was provided by a Endevco Model 2775A Charge Amplifier. After passing through the charge amplifier the resulting output range was ±300 g. Piezoelectric crystal-type accelerometers are ideal for measuring high g excitations, but shock pulses tend to excite the resonance of the crystal. Since the below mount accelerometer will be subjected to very short duration shock pulses the accelerometer was mounted in a 700 Hz mechanical filter whose damping ratio was approximately 0.2. The mechanical filter is essentially a rigid stainless steel can with a protruding thread that is screwed into the object whose accelerations are to be measured. The accelerometer itself is mounted in an aluminum cylinder which is sandwiched between two elastomer pads and inserted into the can. A cap on the external can compresses the pads resulting in a very effective mechanical filter. The filter only allows excitations that are well below the 26 kHz resonant frequency of the crystal to pass thus avoiding exciting the crystal resonance. The sensor locations are shown in Figure 6.1 and the signal conditioning equipment is shown in Figure 6.7.

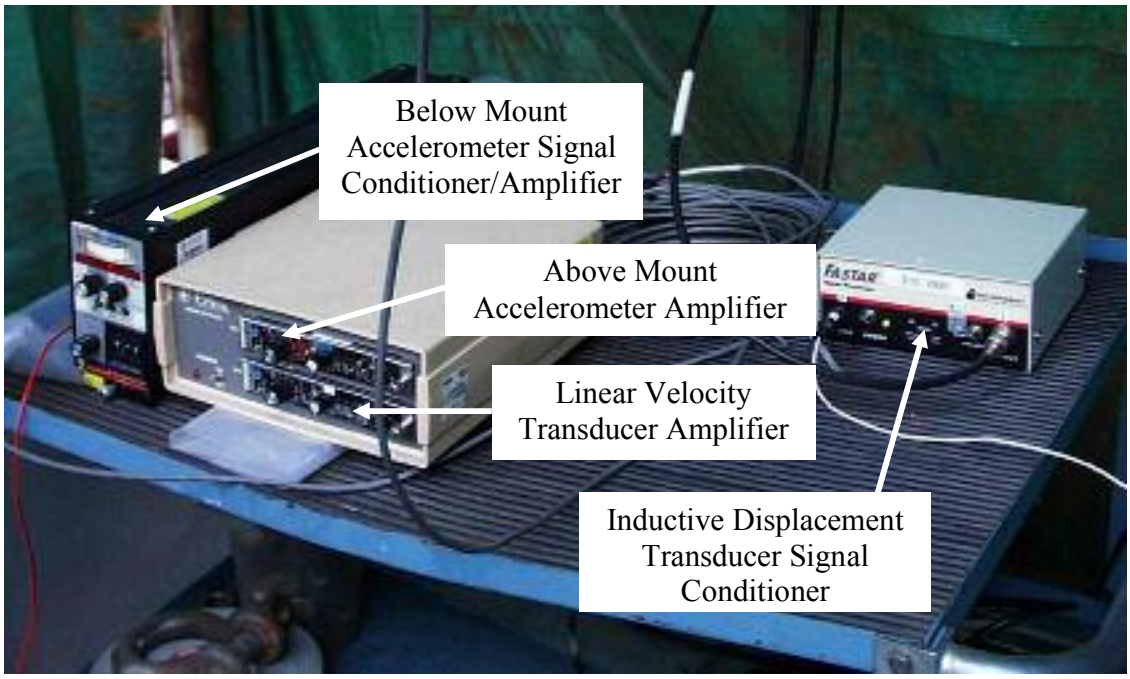


**Figure 6.7**. Drop Test Signal Conditioning Equipment

The four MR dampers are driven by a common D/A channel as shown in Figure 6.6. The dampers require a variable current source. This is supplied by individual Lord Rheonetic Wonder Box Device Controllers for each damper. The Wonder Box is essentially a linear current driver that outputs a current that is proportional to an applied input voltage. The Wonder Box accepts inputs of 0-5 V and outputs 0.4 amps/V above 0.6 V, resulting in a peak current output of 1.5 amps with an input of 3.75 V. Each Wonder Box requires a 12 V, 1.5 amp power supply which was provided by four Digikey T931-P5P-ND power supplies, one supplying each current driver. The MR damper current driver arrangement is shown in Figure 6.8.

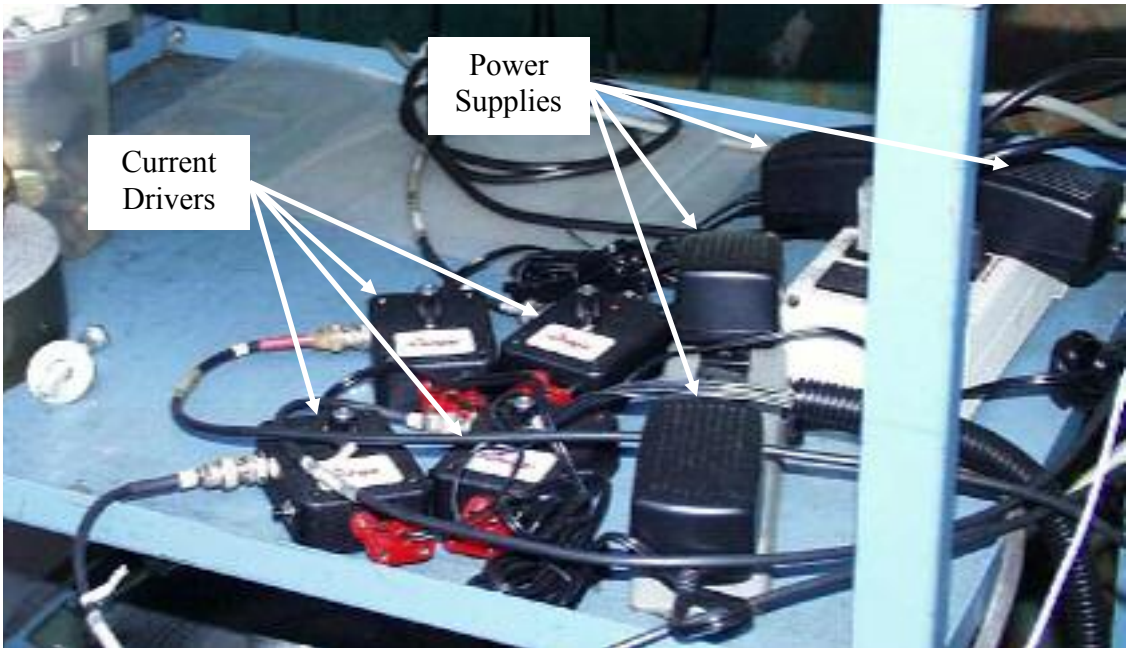


**Figure 6.8**. MR Damper Current Drivers and Power Supplies

The control system was implemented digitally using dSpace rapid control prototyping hardware and software. For control a measure of the above mount acceleration, and the relative displacement and velocity across the mount was required. The above mount acceleration was measured with a cantilever-type accelerometer and a Linear Velocity Transducer (LVT) was used to obtain the relative velocity across the mount. This signal was high-pass filtered to eliminate any DC bias and then integrated to obtain the relative displacement across the mount for use by the controller. This was

done in an attempt to minimize the number of sensors required to do the actual control. In addition to the accelerometer measuring the above mount acceleration a crystal-type accelerometer in a 700 Hz mechanical filter was used to measure the base input. The mechanical filter was implemented to avoid exciting the accelerometer crystal resonance. In addition, an inductive displacement transducer measured the relative displacement across the mount to verify the accuracy of the integrated LVT signal.

## 6.5 Drop Test Results

Two drops heights (One and two inches) were utilized to develop base excitations that were similar in magnitude to the FSP inner bottom and a typical mid-frequency FSP deck fixture. Since it is difficult to achieve identical base excitations from drop-to-drop, the results for each test will be considered separately. This inconsistency stems from the difficulty of achieving consistently identical drop heights using a forklift. Also the dynamics introduced by the quick-release hook can easily vary from test to test.

The test series consisted of two drops at both drop heights using each controller. This was done to ensure test repeatability. In addition two additional tests were performed at each drop height using fixed voltages to the MR damper current drivers. The two cases considered were 0 V and 3.75 V applied to the current drivers, corresponding to the minimum and maximum damper force, respectively. This was done to bound the performance limits that could be achieved with the controlled MR/Air mount. It would be expected that the minimum above mount acceleration would be achieved with the damper voltage off (V = 0) and the minimum mount deflection would be achieved with maximum damper voltage (V = 3.75). This is exactly what was observed in the tests. Furthermore, it would be expected that the controllers would provide performance that was somewhere between these two extremes. By providing an

optimal damping force the controllers should provide an optimal balance between above mount response acceleration and mount deflection.

Figure 6.9 shows the response acceleration versus the base input for the LQR Optimal Controller after the 1 in. drop. Figure 6.10 plots the associated relative displacement for the same input. Figures 6.11 and 6.12 plot the same data for the Velocity Feedback Controller.

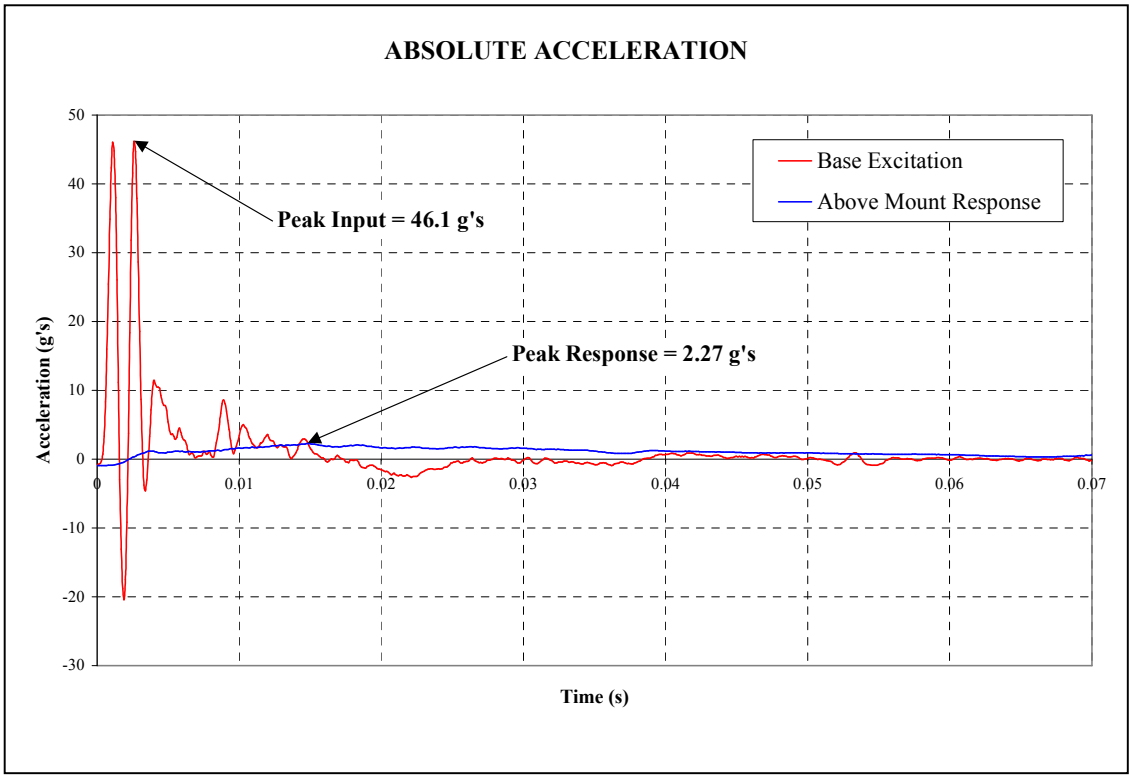


**Figure 6.9**: Acceleration Response to 1in. Drop with LQR Optimal Controller

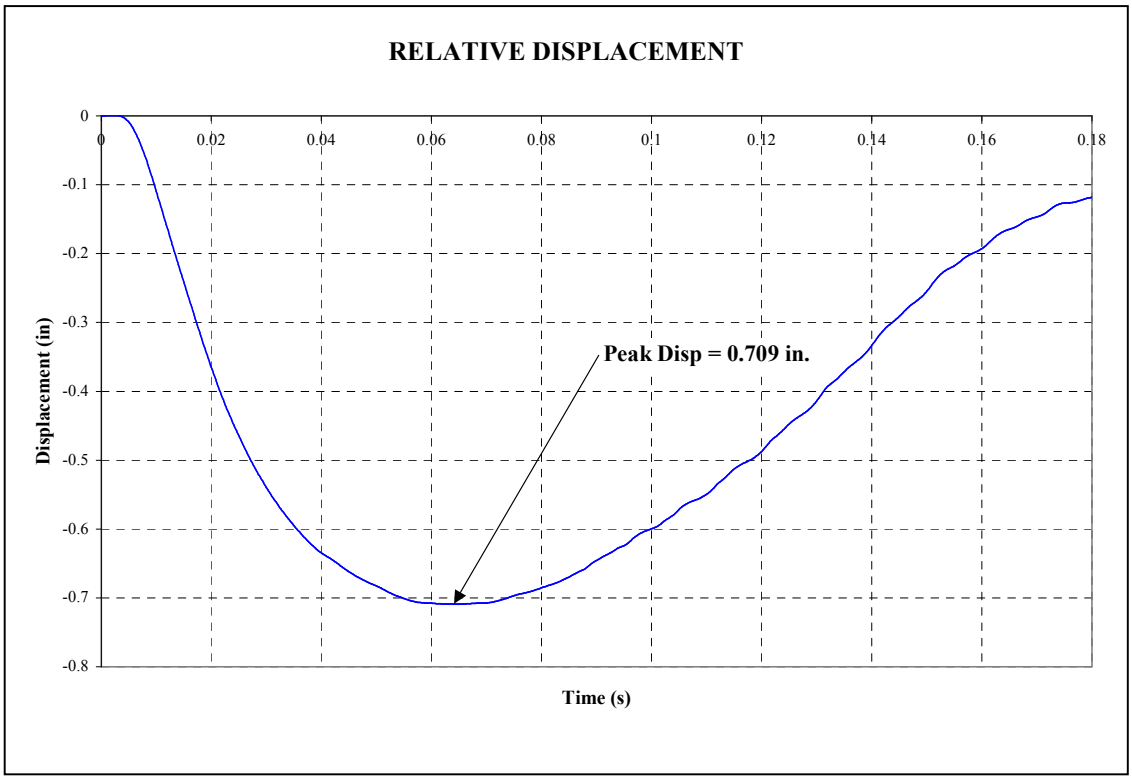


**Figure 6.10**: Displacement Response to 1in. Drop with LQR Optimal Controller

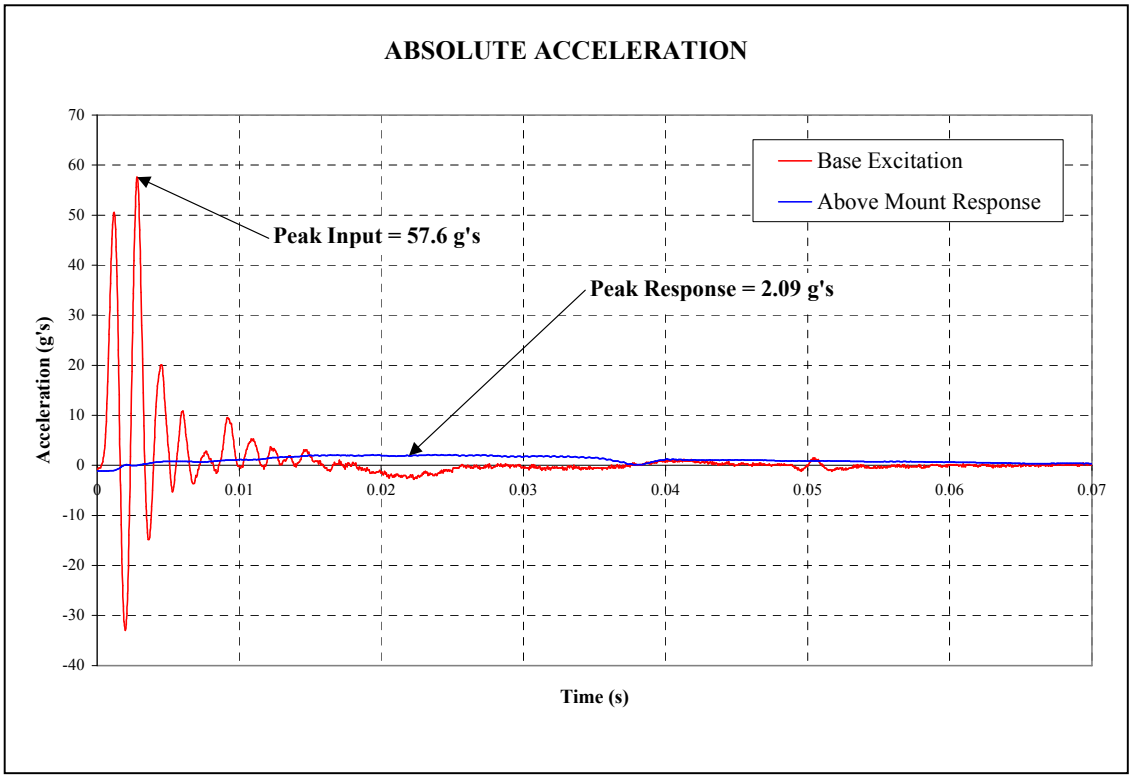


**Figure 6.11**: Acceleration Response to 1in. Drop with Velocity Feedback Controller

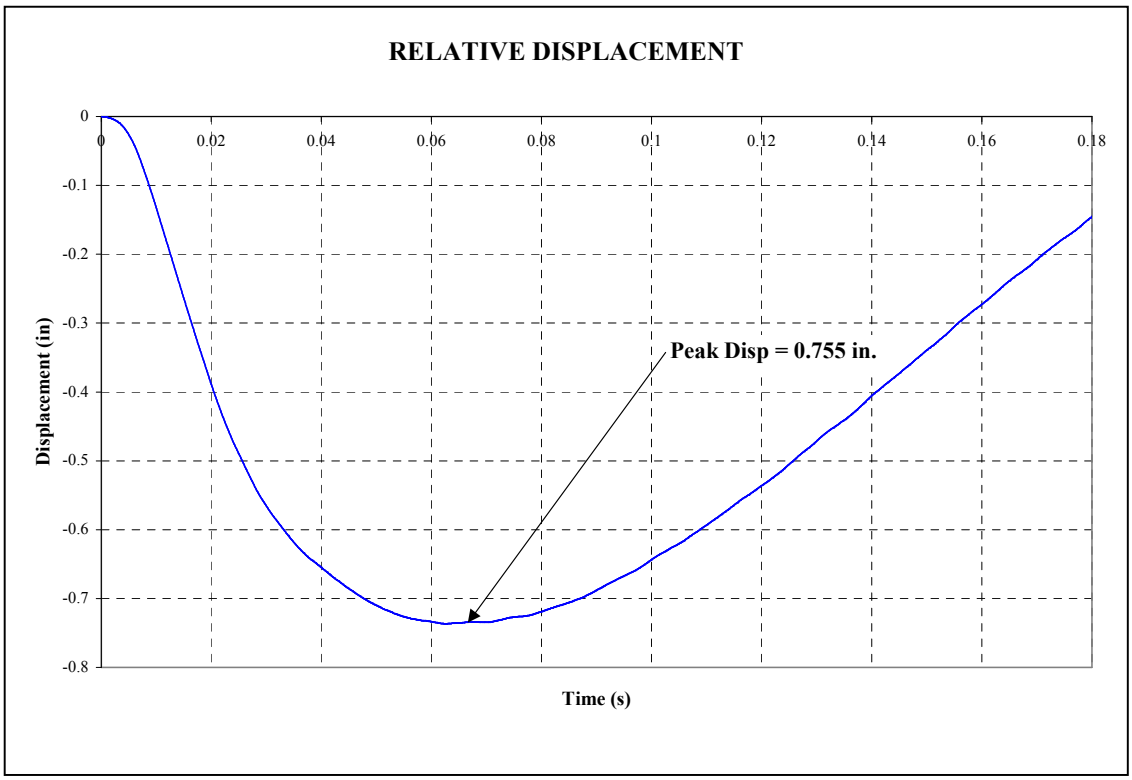


**Figure 6.12**: Displacement Response to 1in. Drop with Velocity Feedback Controller

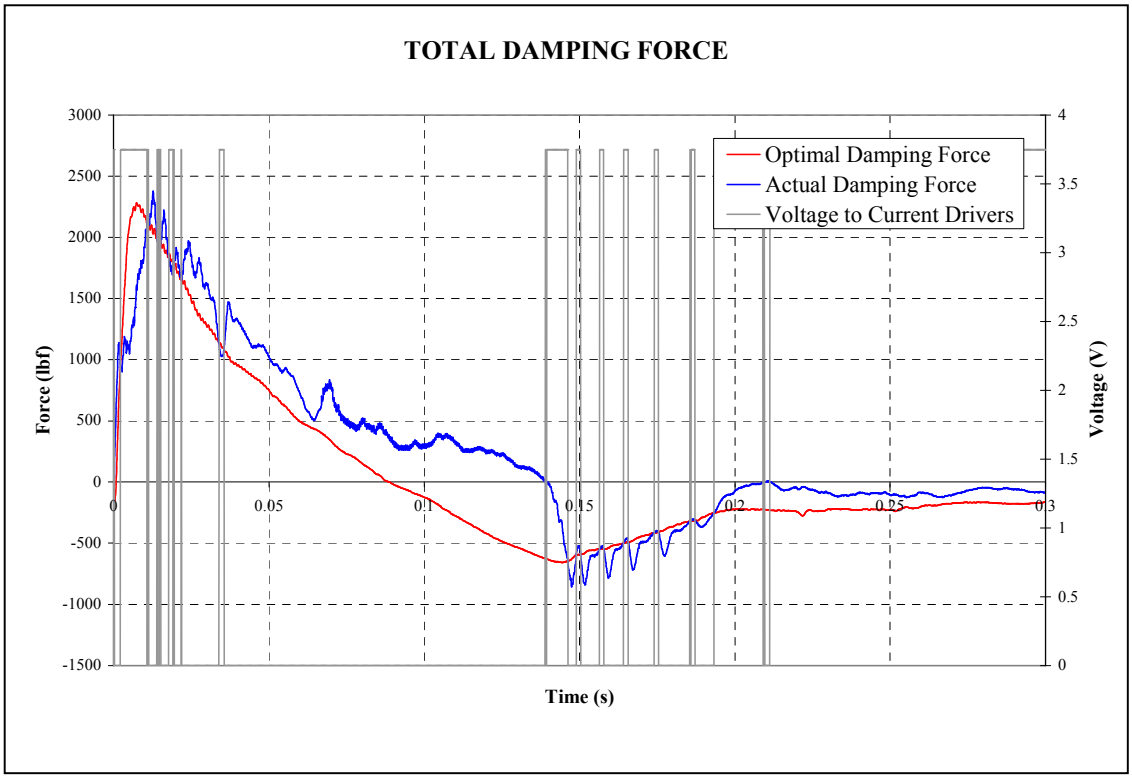


**Figure 6.13**: Damping Force for 1 in. Drop with LQR Optimal Controller

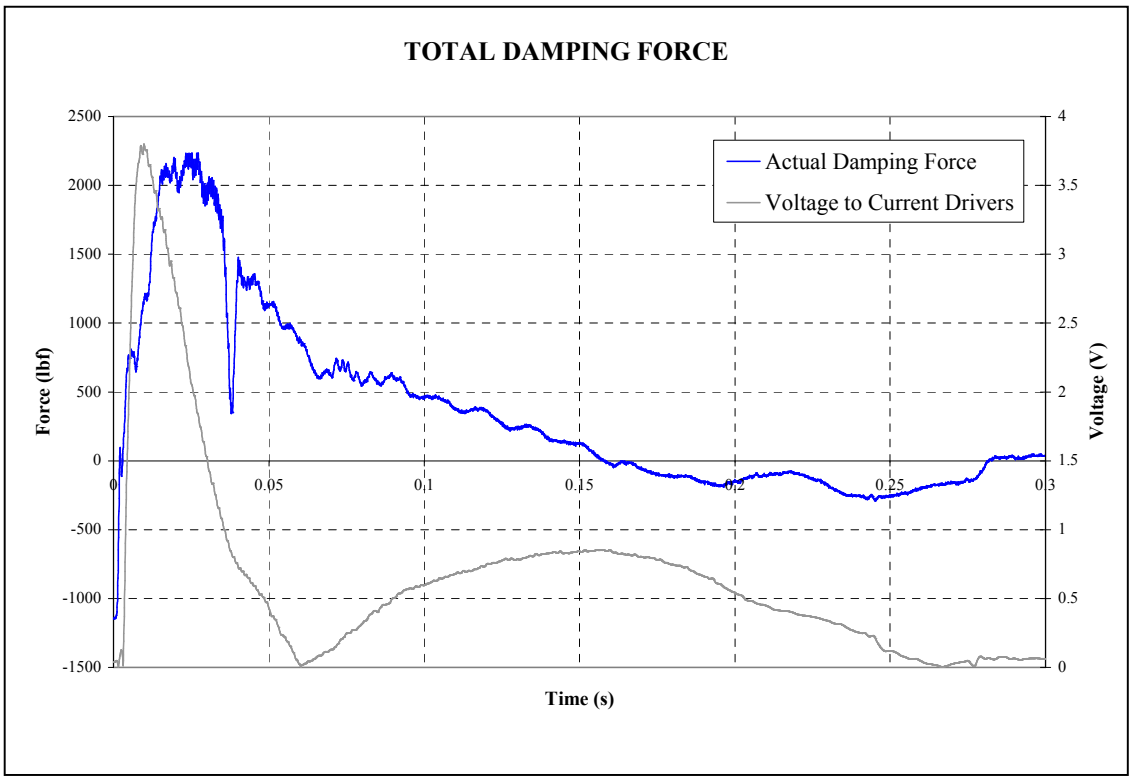


**Figure 6.14**: Damping Force for 1 in. Drop with Velocity Feedback Controller

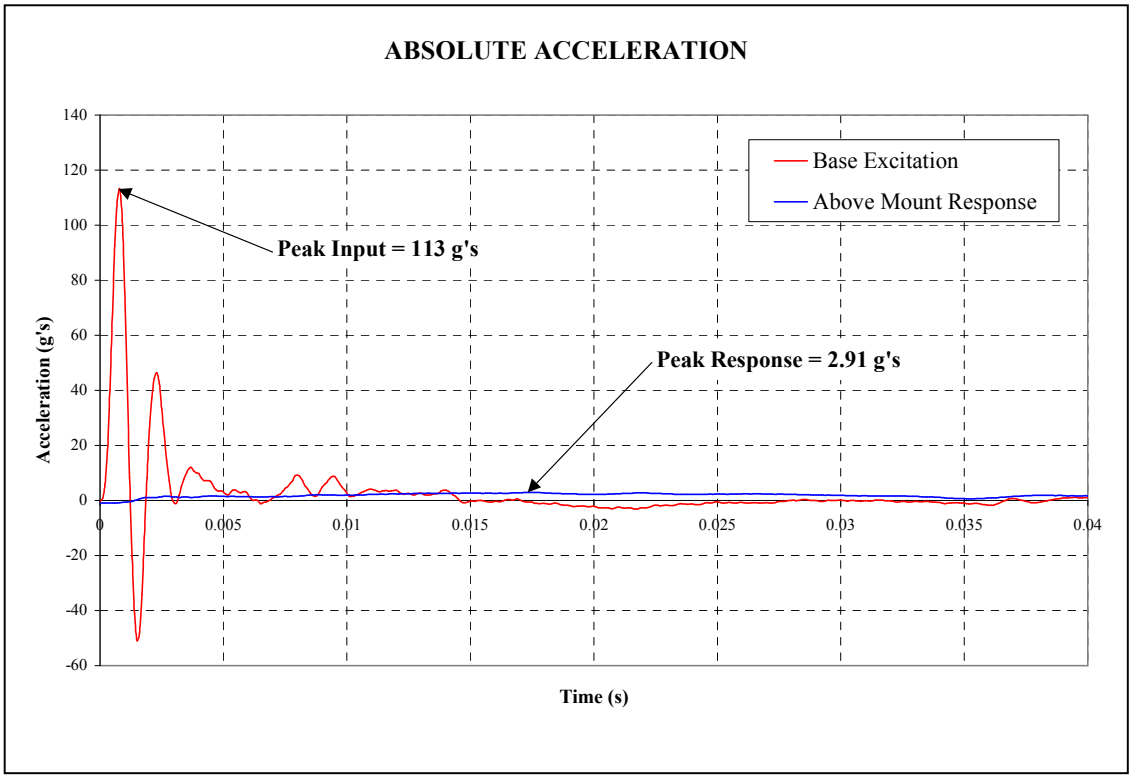


**Figure 6.15**: Acceleration Response to 2 in. Drop with LQR Optimal Controller

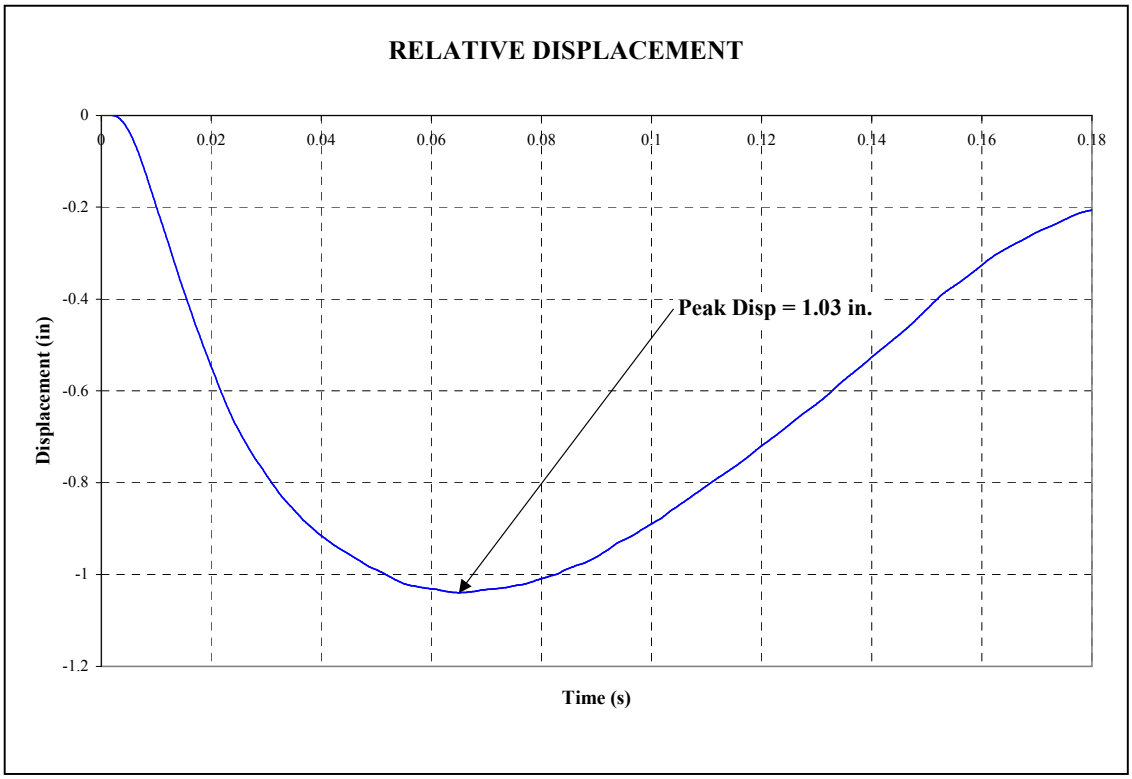


**Figure 6.16**: Displacement Response to 2 in. Drop with LQR Optimal Controller

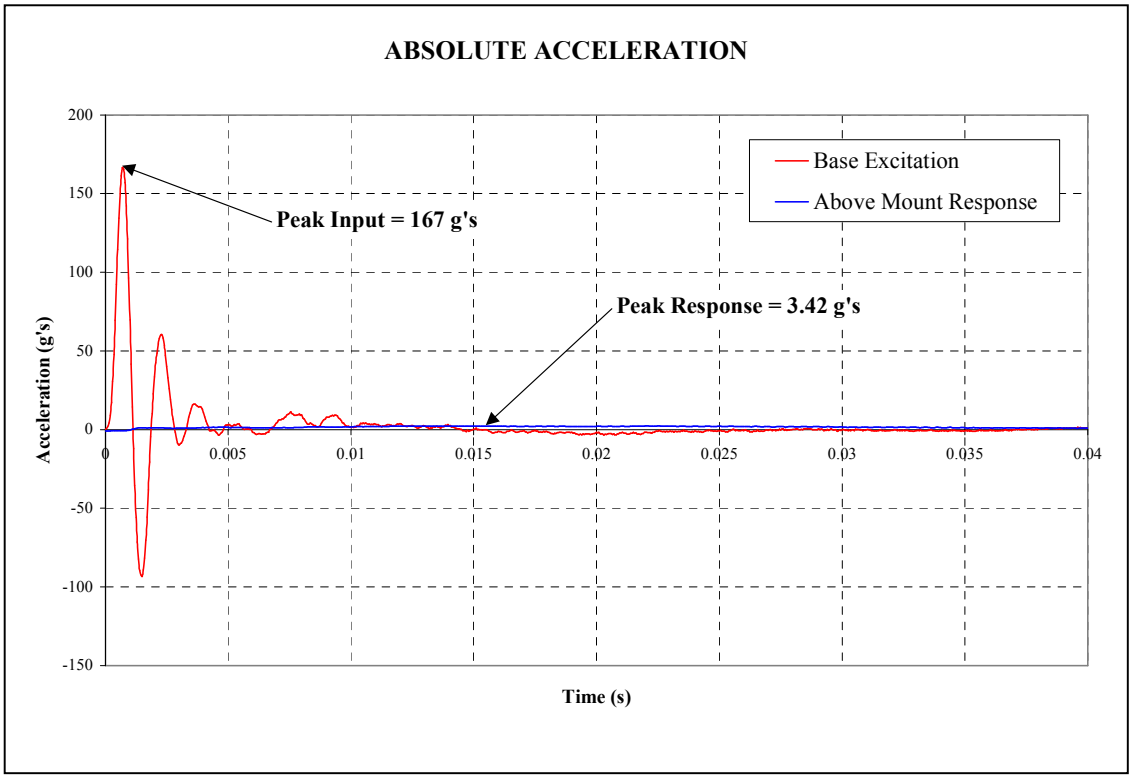


**Figure 6.17**: Acceleration Response to 2 in. Drop with Velocity Feedback Controller

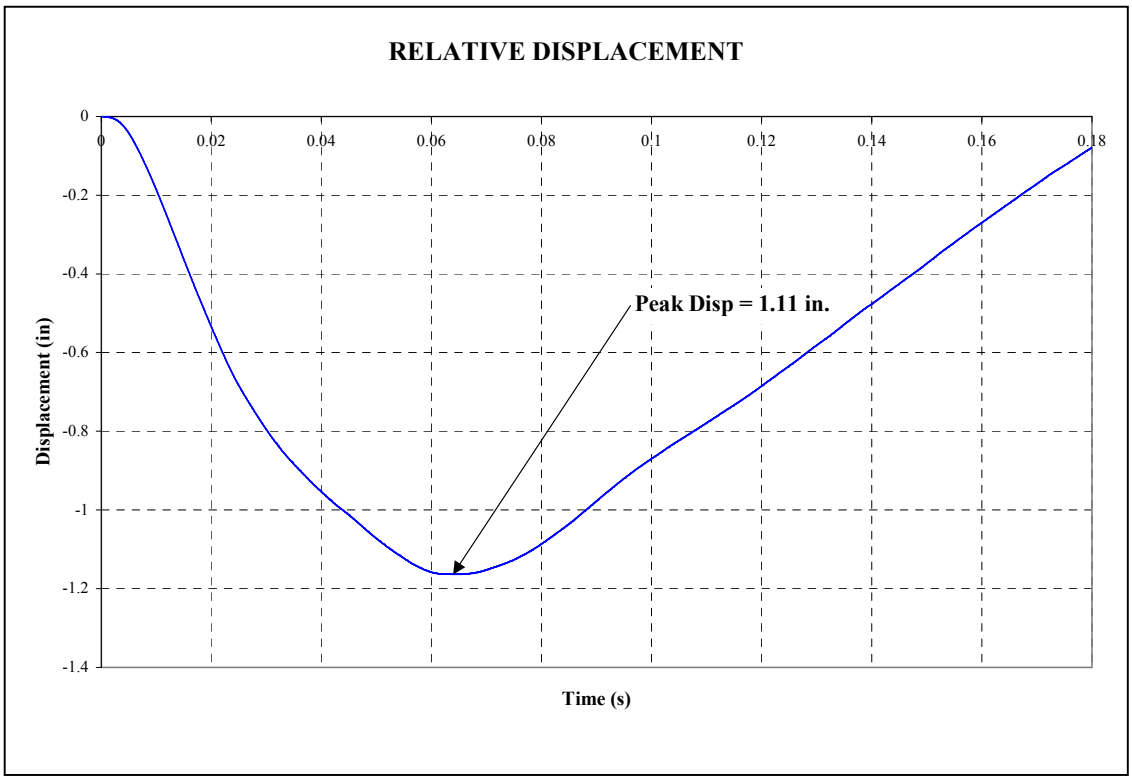


**Figure 6.18**: Displacement Response to 2 in. Drop with Velocity Feedback Controller

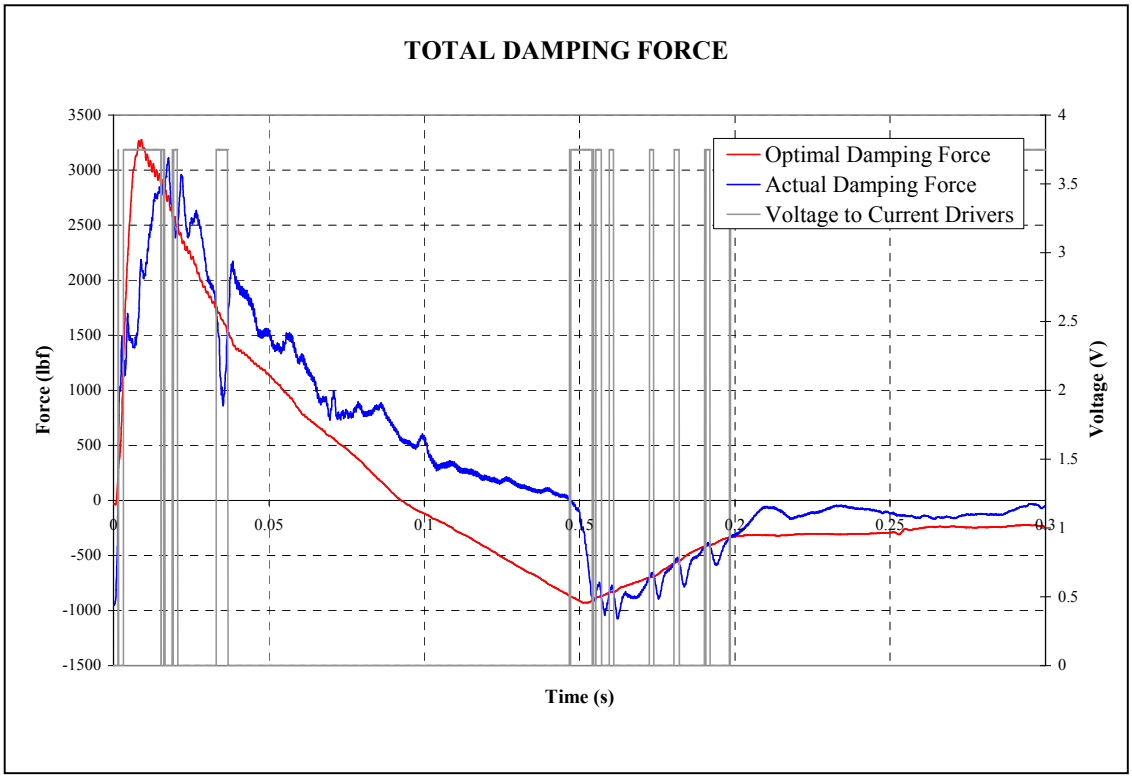


**Figure 6.19**: Damping Force for 2 in. Drop with LQR Optimal Controller

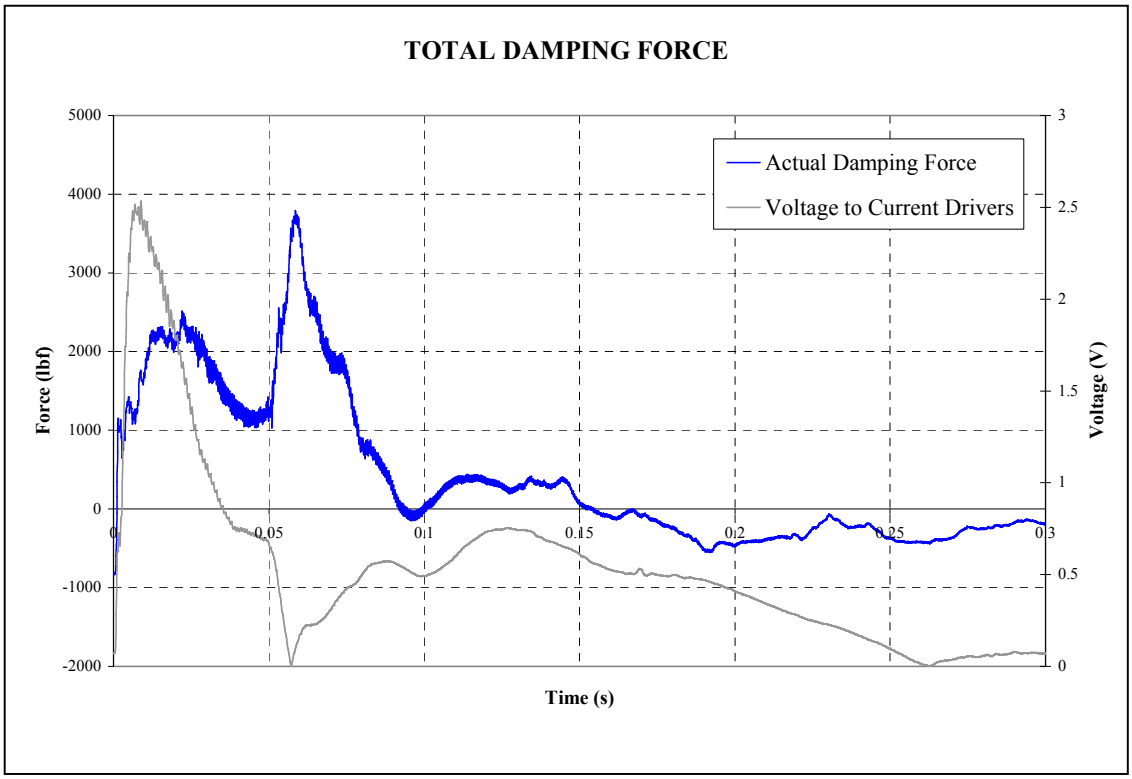


**Figure 6.20**: Damping Force for 2 in. Drop with Velocity Feedback Controller

Figure 6.13 is a plot of the actual damping force from the four dampers versus the optimal damping force using the LQR Optimal Controller. Overplotted is the command voltage to the MR damper current drivers. Figure 6.14 is a plot of the total damping force for the four damper with the Velocity Feedback Controller. As can be seen both of the controllers provide a significant reduction in transmitted acceleration with a simultaneous minimal mount deflection.

Figure 6.15 is a plot of the response acceleration versus the base input for the LQR Optimal Controller after the 2 in. drop. Figure 6.16 plots the associated relative displacement for the same input. Figures 6.17 and 6.18 plot the same data for the Velocity Feedback Controller. Figure 6.19 is a plot of the actual damping force from the four dampers versus the optimal damping force using the LQR Optimal Controller. Also plotted is the command voltage to the MR damper current drivers. Figure 6.20 is a plot of the total damping force for the four dampers with the Velocity Feedback Controller. Again it is clear that both of the controllers provide a significant reduction in transmitted acceleration with a simultaneous minimal mount deflection. A summary of the mount performance with both inputs is shown in Table 6.1.

| Drop Height | LQR OPTIMAL CONTROLLER | | | VELOCITY FEEDBACK CONTROLLER | | |
|---|---|---|---|---|---|---|
| | Base Input | Above Mount Response | Mount Deflection | Base Input | Above Mount Response | Mount Deflection |
| 1 in. | 46.1 g's | 2.27 g's | 0.709 in. | 57.6 g's | 2.09 g's | 0.755 in. |
| 2 in. | 113 g's | 2.91 g's | 1.03 in. | 167 g's | 3.42 g's | 1.11 in. |

**Table 6.1**: Drop Test Response Comparison

It should be noted that the 46.1 g peak input seen in the test series is approximately equivalent to the peak input seen on a mid-frequency FSP deck fixture. The 113 g peak input seen in the test series is the same order of magnitude as the peak inner bottom acceleration of the Floating Shock Platform (FSP) and the 167 g peak input exceeds the

peak inner bottom acceleration of the FSP. As can be seen in Figure 6.21 these inputs have amplitudes that are similar to those experienced during typical FSP shock tests.

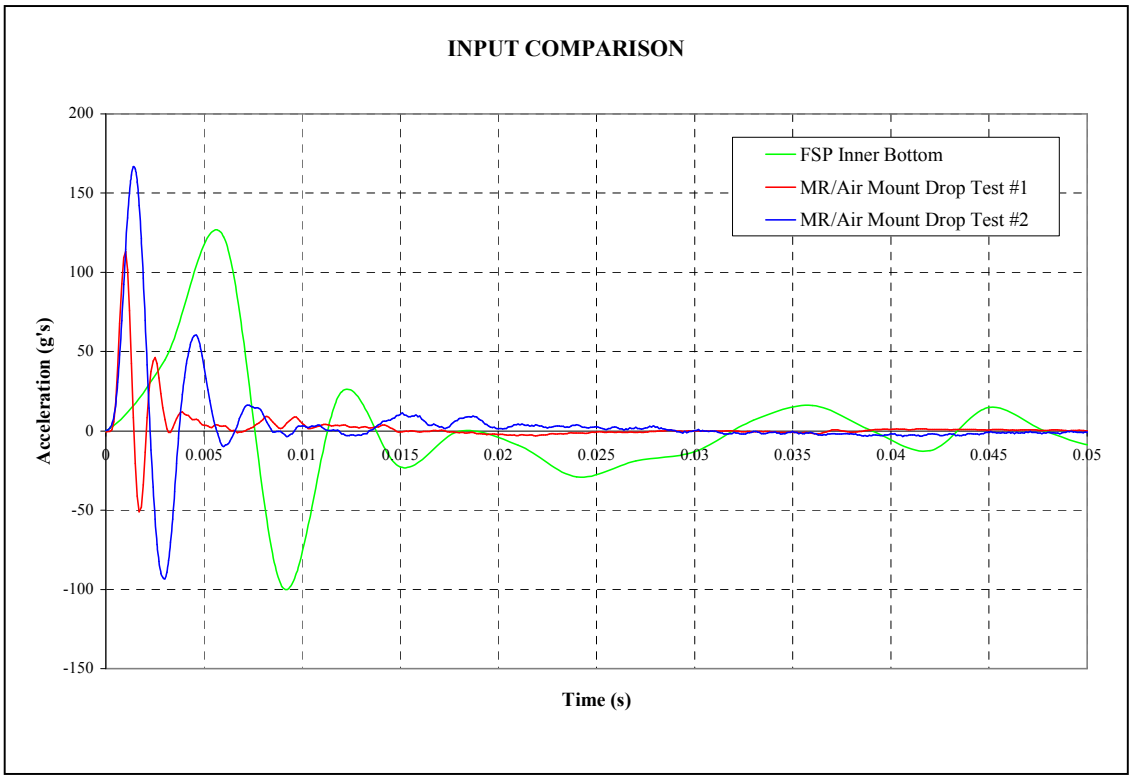


**Figure 6.21**: Comparison of FSP Inputs to MR/Air Mount Test Input

## 6.6 Model Validation

For the model of the isolation system to be useful for developing more complex multi-degree-of-freedom models that would more effectively capture the motion of an isolated piece of equipment, it is necessary to have a validated model. Furthermore, having a validated model allows the consideration of performance of other controllers without re-testing. In an attempt to validate the model discussed in Section 6.2, the experimental data from several of the drop tests was overplotted with the analytical data generated by the model using the below mount acceleration data from the drop tests as the input to the model. All of the numerical simulations were performed using the MATLAB® and/or Simulink® models shown in Appendix A. A typical comparison of

experimental and analytical data is shown in Figures 6.22, 6.23 and 6.24, representing a comparison of relative displacement, relative velocity and absolute above mount acceleration, respectively. For these particular plots the input was the 1 in. drop and the velocity feedback controller was used. Similar plots confirmed the accuracy of the model for the LQR optimal controller and the larger drops.

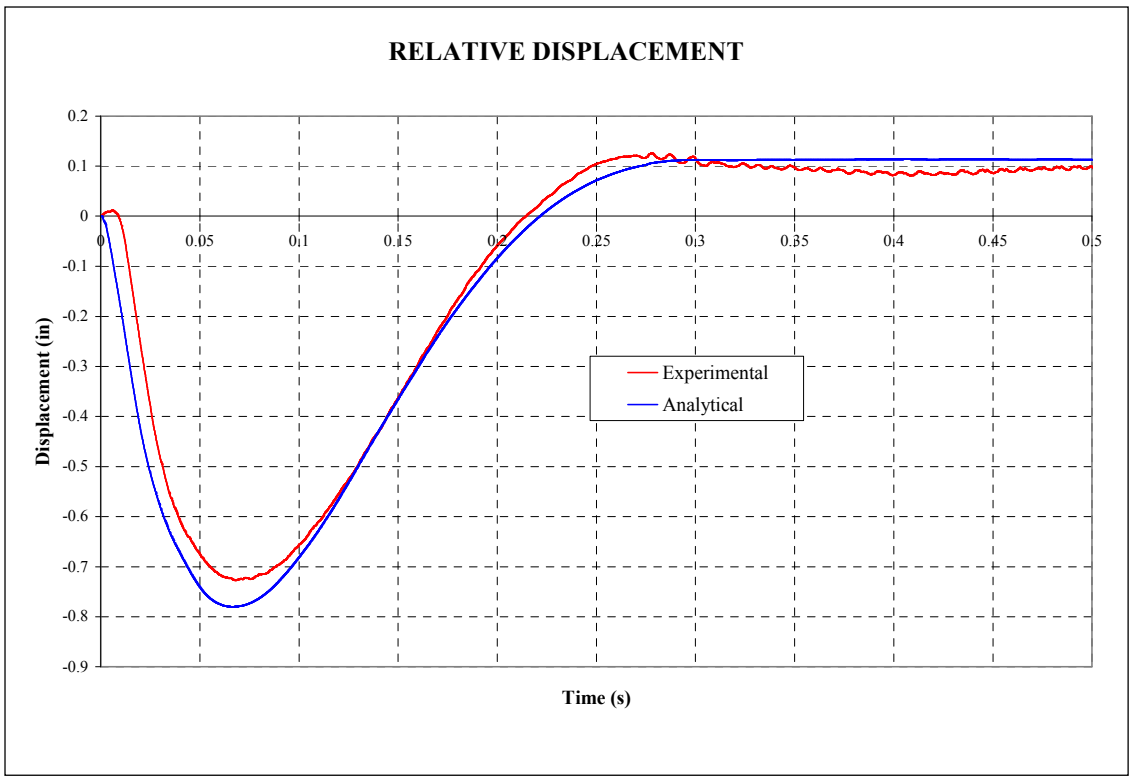


**Figure 6.22**: Experimental and Analytical Data Comparison (Relative Displacement)

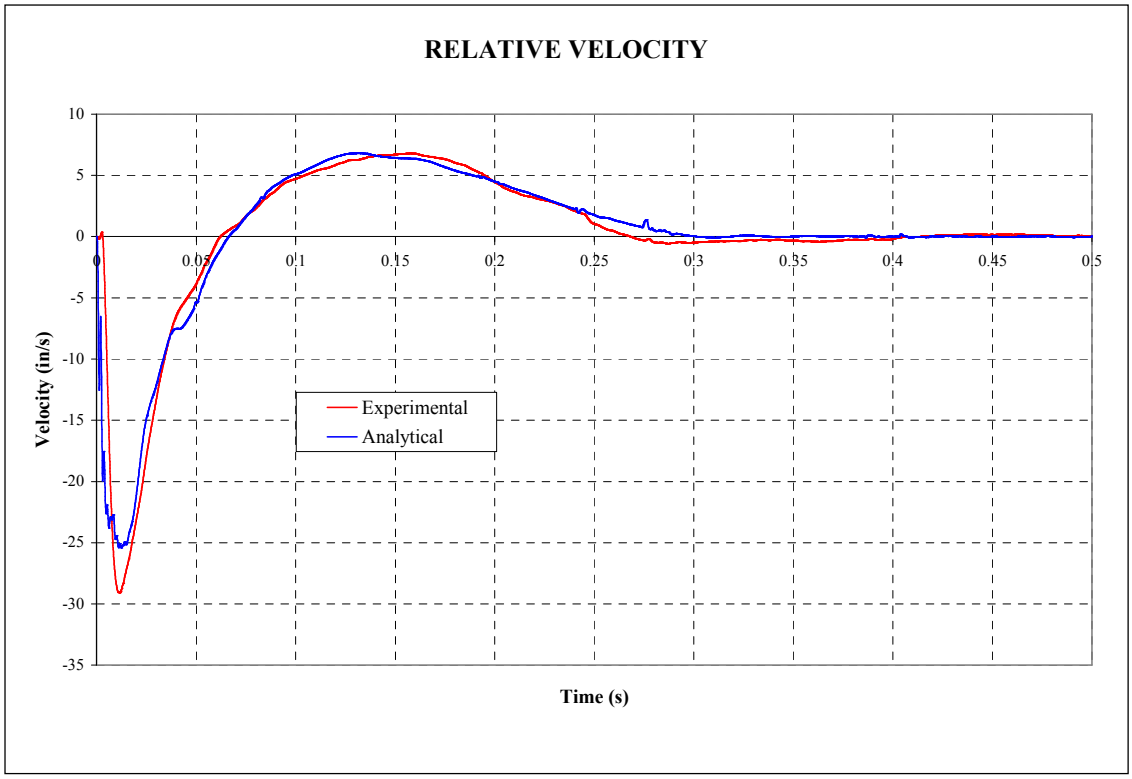


**Figure 6.23**: Experimental and Analytical Data Comparison (Relative Velocity)

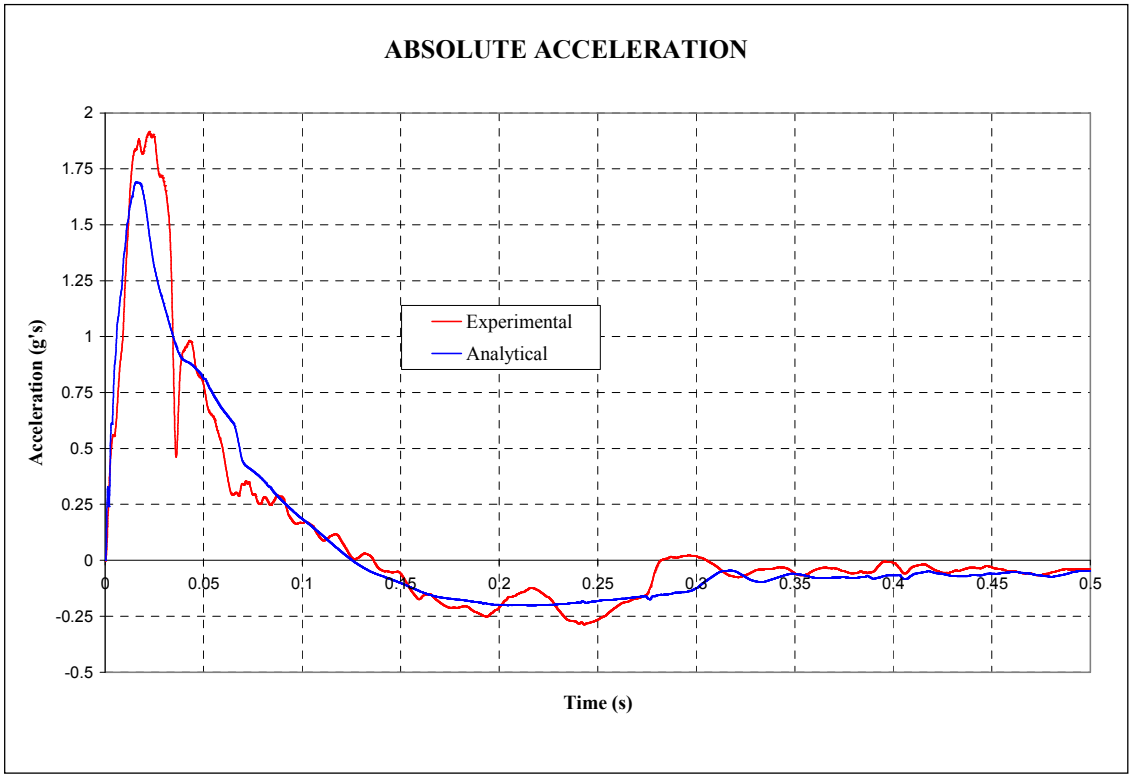


**Figure 6.24**: Experimental and Analytical Data Comparison (Absolute Acceleration)

From the figures it can be seen that the model is accurately tracking the response from the drop tests. In terms of relative displacement the model was within 0.05 in. of the experimental data. This is considered within the range of experimental error. It should be noted that while the restraint clamps did a reasonable job of maintaining a minimum relative displacement of the mount prior to impact, they did not completely zero the initial relative displacement. This can be seen in the Figure 6.22. Including a more accurate representation of the initial conditions in the simulation would lead to even better agreement between the analytical and experimental data. However, the simulation data was considered accurate enough to ensure confidence in the predictive capability of the model.

The acceleration plots were within 0.22 g with the exception of an unexplainable spike that appeared on all of the above mount acceleration data to varying degrees. This spike can be seen in Figure 6.24 at t = 0.036 s. One of the theories proposed to explain this spike was that it may occur when the clamps holding the masses together release. However, the spike was not seen in the displacement and velocity data. This suggests that the spike may be due to some anomaly in the accelerometer. Other than this strange spike the experimental and analytical data was in excellent agreement for all of the tests. Considering the difficulty of appropriately matching the inputs and initial conditions for the model with the experimental inputs, and the complexity of the model, the validation was considered to be very successful. The analytical results were certainly very capable of accurately predicting the mount deflection and above mount absolute acceleration necessary for mount performance predictions.

## 6.7 Acceleration Limiting Bang-Bang Controller Performance

Since the concept for this controller was developed after the drop test series had been completed it was necessary to investigate its performance using the validated model. The concept behind the controller is very simple, but it appears to be ideal when

considering the performance goals of a shipboard shock isolation system. Shipboard isolation systems typically support a component that has a prescribed acceleration limit. That being the case it would be ideal if it were possible to select the above mount response in terms of an acceleration limit. Furthermore, shipboard environments, particularly submarines, have strict rattle space requirements due to the premium on space. Therefore, the ideal shipboard isolation system would allow the user to select the above mount acceleration limit while providing the absolute minimum mount excursion. This is the concept behind the Acceleration Limiting Bang-Bang Controller.

The controller simply supplies the maximum voltage to the MR damper current driver, therefore producing the maximum damping force, unless the acceleration $\ddot{x}$ exceeds some prescribed limit. Mathematically the controller can be described as shown in Equation 5.40.

The controller can easily be implemented and requires only an accelerometer for sensing the response acceleration. It is anticipated that during normal operation, i.e., when the ship is not being attacked, the voltage to the current drivers would be set to zero and then automatically switched to the control scheme when the acceleration exceeds some preset limit. The controller would then remain in control of the applied voltage until the threat has been removed at which time the voltage to the current drivers would be reset to zero. This would minimize the possibility that long term exposure to a magnetic field could magnetize the ferrous particles in the MR fluid.

To determine the performance of this controller a series of simulations was performed using the validated model. Figure 6.25 shows the effect of the controller on limiting the above mount absolute acceleration to a prescribed level. It can be seen that the MR damper can respond fast enough to limit the acceleration. Of course the actual performance would be dependent on sizing the damper appropriately to provide the required range of damping forces to effectively limit the acceleration. Figure 6.26 shows the corresponding relative displacements across the mount. Clearly shown is the classic displacement-acceleration trade-off. As the requested acceleration limit decreases the mount deflection increases to accommodate the added displacement required of a more

gradual deceleration of the equipment. Overall the controller shows considerable promise for use in a shipboard shock isolation system.

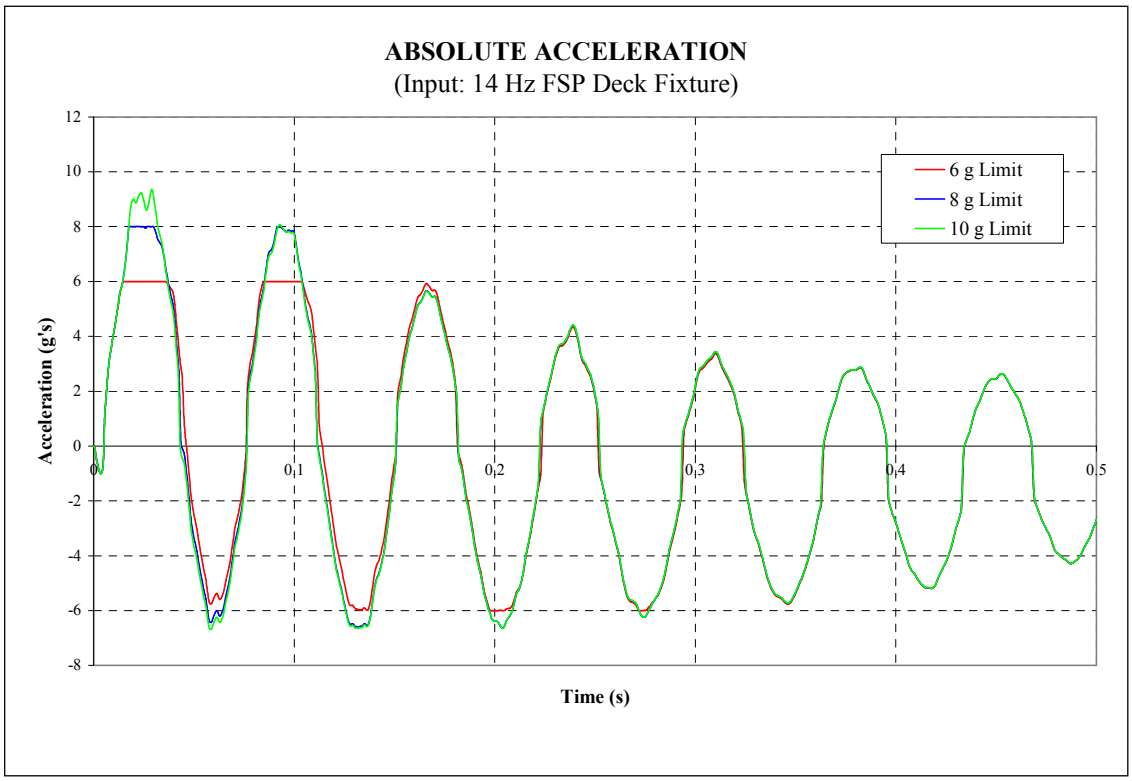


**Figure 6.25**: Above Mount Acceleration with Acceleration Limiting Controller

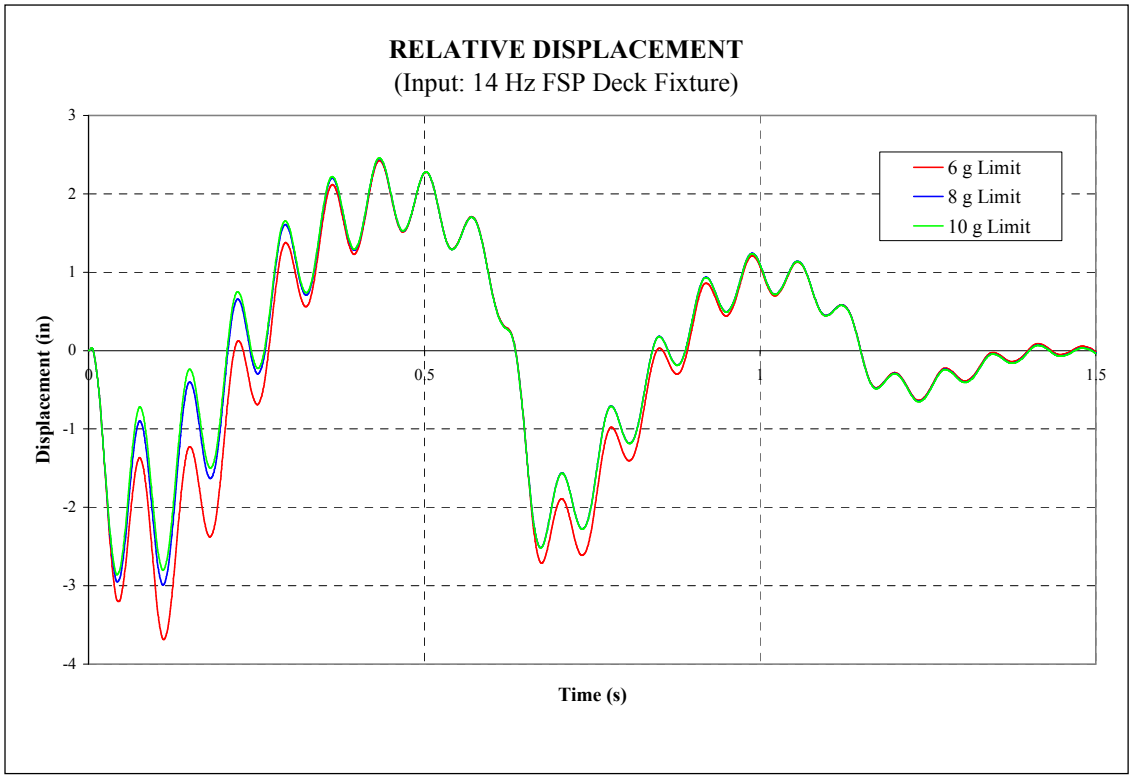


**Figure 6.26**: Mount Deflection with Acceleration Limiting Controller

## 6.8 Controller Performance Comparison

In order to compare the performance of the controllers a simulation was performed using the validated model and the three best performing controllers, 1) LQR Optimal, 2) Velocity Feedback and 3) Acceleration Limiting Bang-Bang Controllers. The input to the model was the vertical component from actual FSP test data. In this test the FSP was equipped with a 14.27 Hz deck fixture. Figure 6.27 shows the resulting relative displacement across the mount with the three controllers. From the figure it can be seen that while the controllers achieved very similar deflections during the initial transient, the Acceleration Limiting Bang-Bang controller achieved the lowest relative displacement of the three controllers during the bubble pulse. Figure 6.28 shows the corresponding above mount absolute acceleration. Again from the figure it appears that the Acceleration Limiting Bang-Bang controller achieves the lowest above mount

acceleration. Furthermore, this controller allows the acceleration limit to be preset to some prescribed level. This is particularly useful for isolating COTS equipment which may have different fragility levels.

Figure 6.29 compares the resulting total damping force for the three controllers. From the figure it is clear that the controllers definitely result in significant differences in the form of the applied damping force. Figures 6.30, 6.31, and 6.32 show the damping force for each controller with the voltage (×1000) applied to the MR damper current drivers overlaid. Again it is clear that the three control algorithms take a very different approach to controlling the dampers, while providing similar performance. This suggests that it is not necessary to utilize complex control algorithms to achieve excellent isolation performance with these dampers.

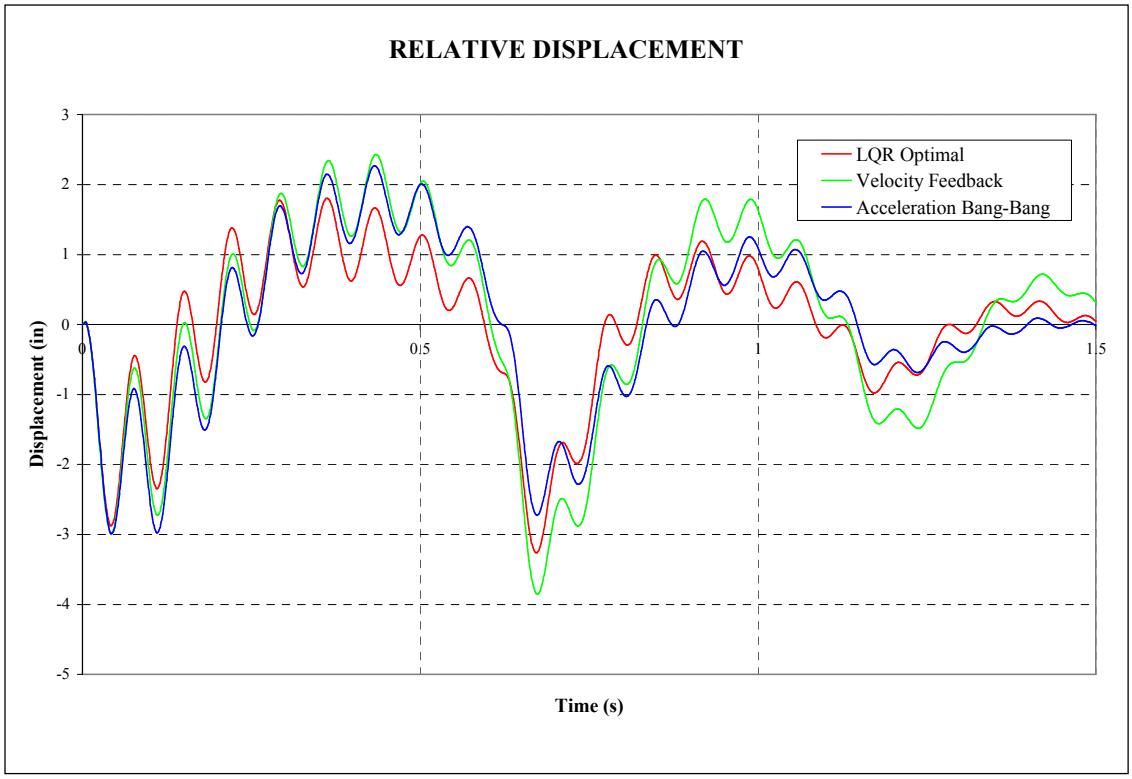


**Figure 6.27**: Comparison of Mount Relative Displacements

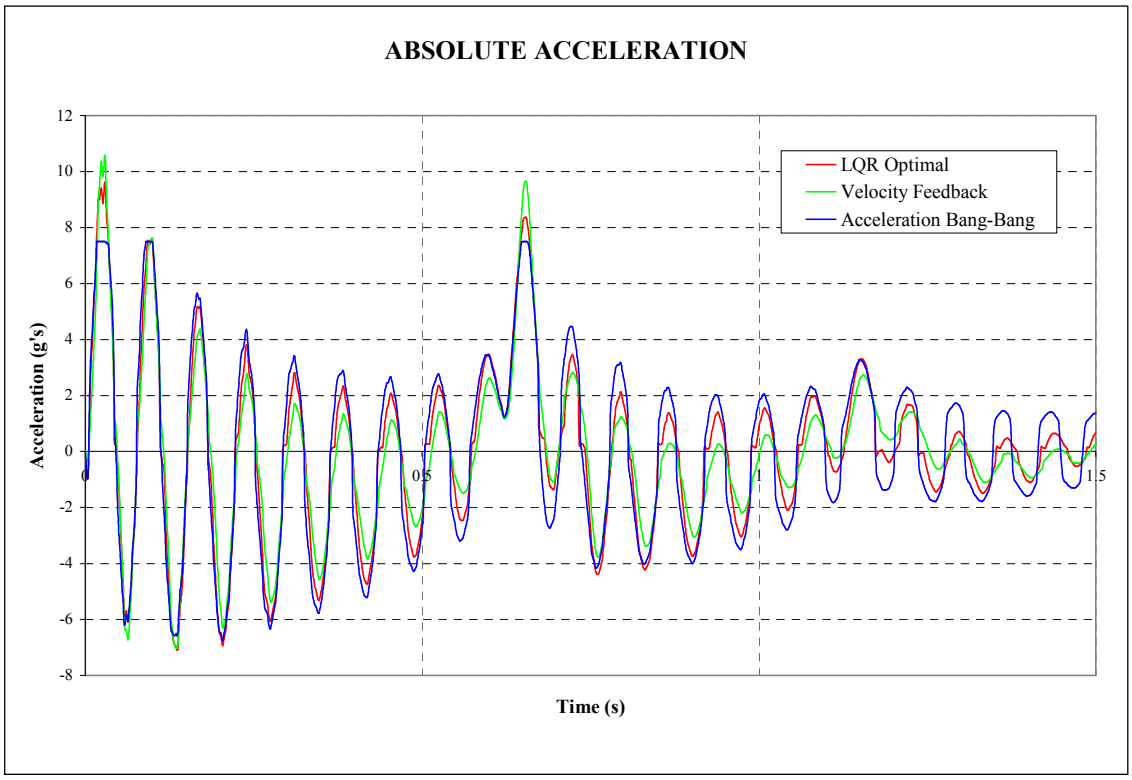


**Figure 6.28**: Comparison of Above Mount Absolute Acceleration

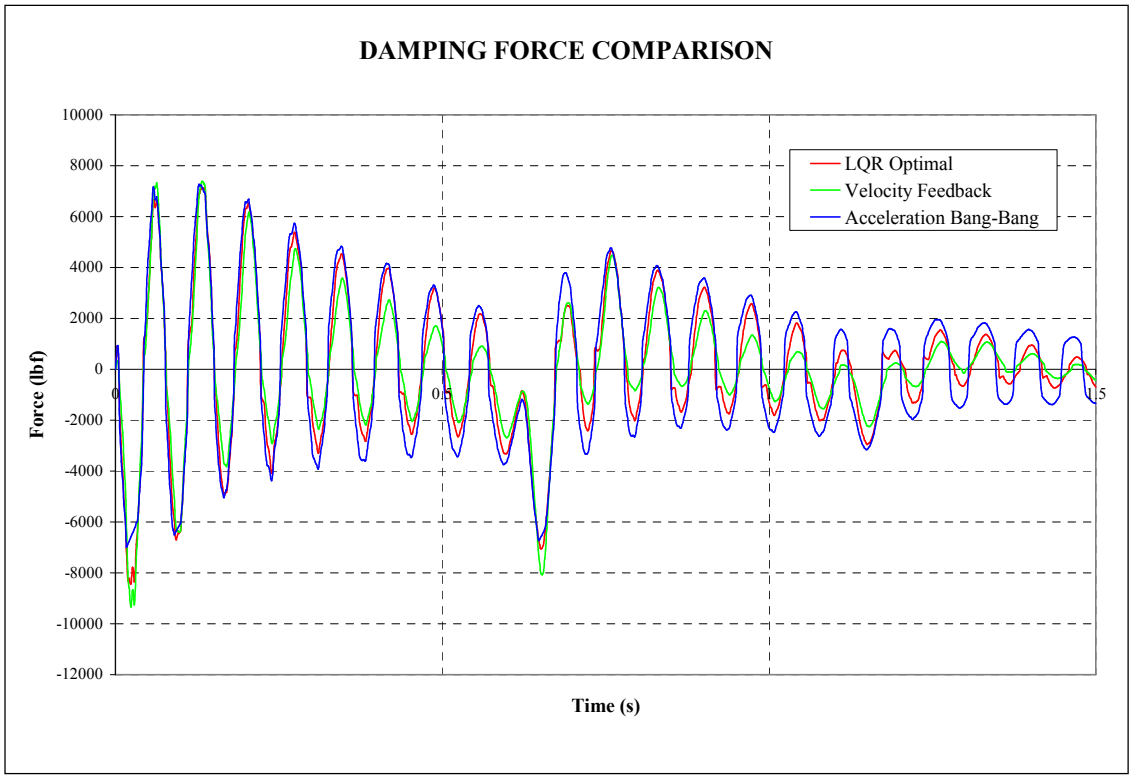


**Figure 6.29**: Controller Damping Force Comparison

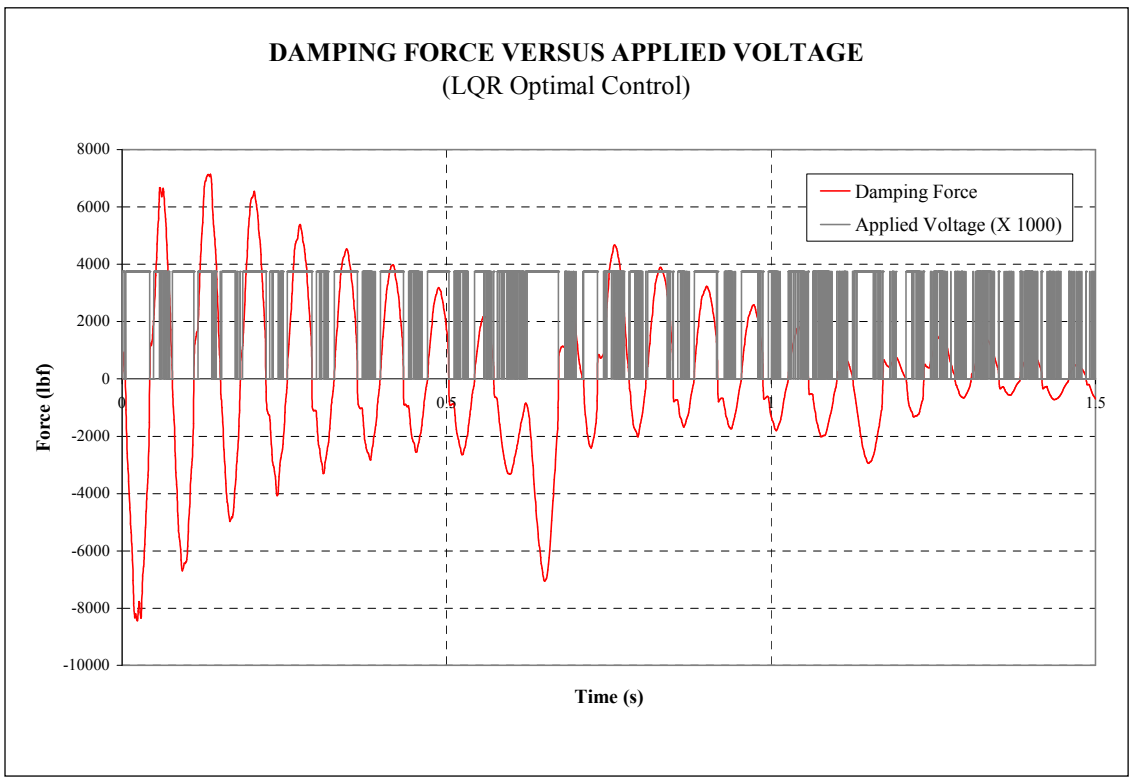


**Figure 6.30**: Damping Force and Control Voltage with LQR Controller

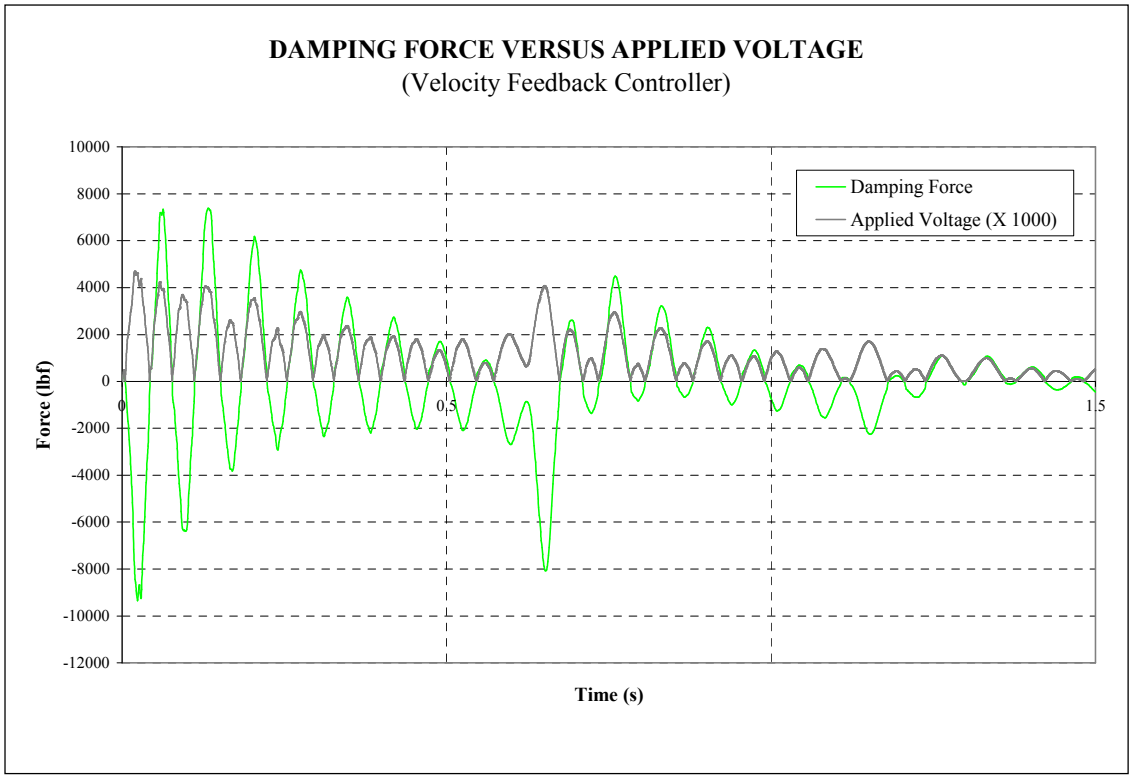


**Figure 6.31**: Damping Force and Control Voltage with Velocity Feedback Controller

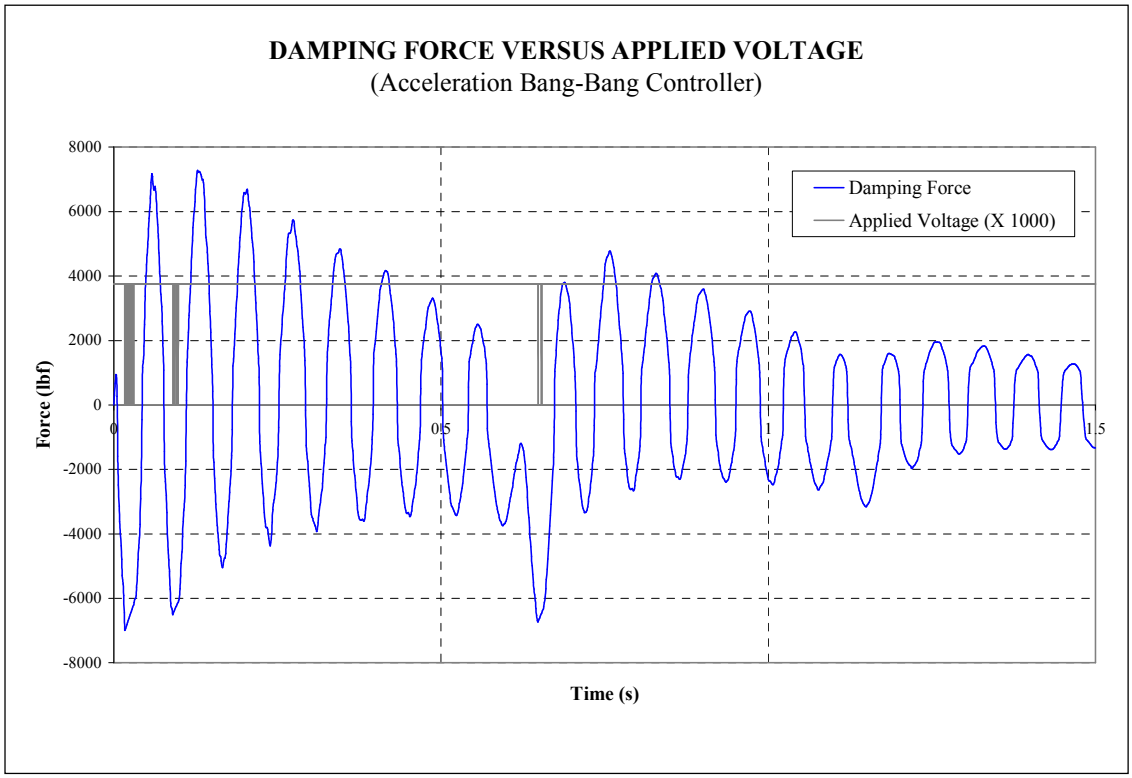


**Figure 6.32**: Damping Force and Control Voltage with Bang-Bang Controller

# 6.9 MRAM Performance Case Studies

Shipboard isolation systems can be roughly divided into three categories based on their intended application. These categories are (1) Equipment level isolation, (2) Equipment raft isolation and (3) Deck isolation. Equipment level isolation is intended to isolate individual pieces of equipment, equipment raft isolation is intended to isolate rafts containing multiple pieces of equipment, and deck isolation is intended to isolate entire decks. Obviously these categories are not all inclusive and overlap occurs between the various categories, but these types of isolation hold in general. In order to determine the performance of the subject isolation system in each of these categories, three case studies were developed in an attempt to determine how the performance varies with the size of the isolated mass. In all three cases the Acceleration Bang-Bang controller will be utilized and the input velocity is from a 14 Hz DSF on a FSP during an actual test. The inputs used in the case studies is shown in Figure 6.33. The three test cases are discussed in detail in the next section.

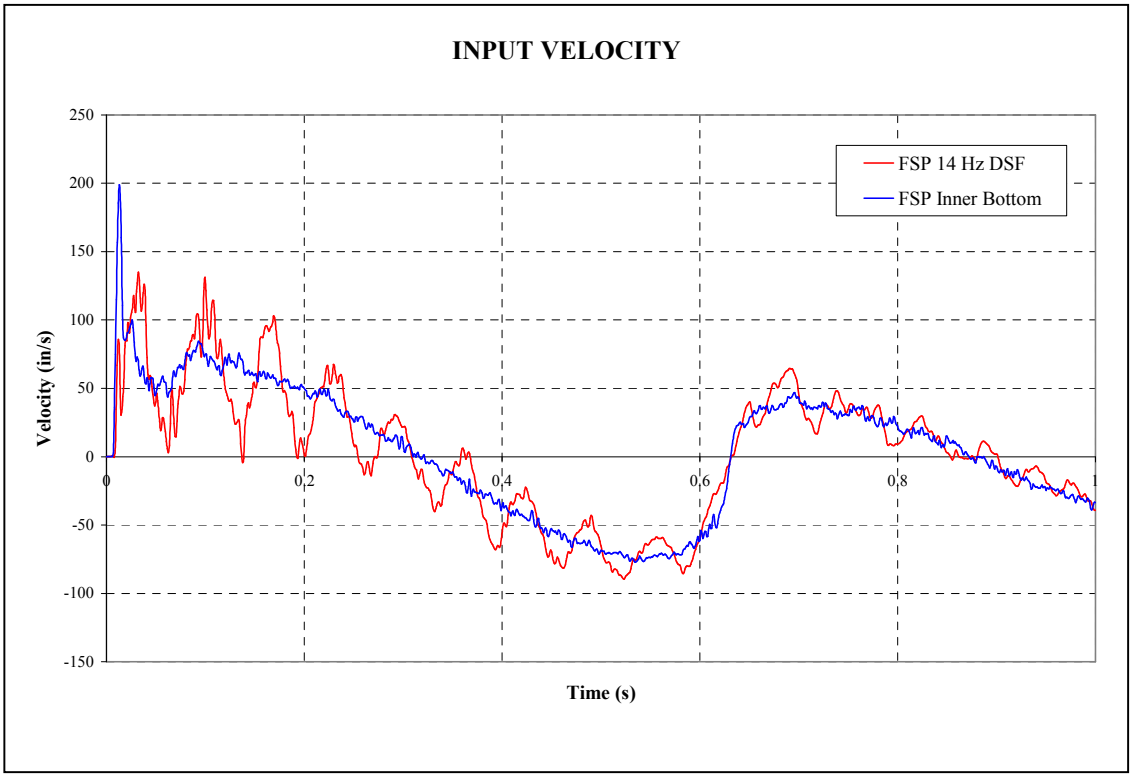


**Figure 6.33**: Input Used in Performance Case Studies

## 6.9.1 Equipment Level Isolation Performance

The first test case involves the shock isolation of a hypothetical 1000 lb electronic equipment cabinet with a 2 Hz air spring and four MR dampers. The model is otherwise equivalent to the single degree-of-freedom base excitation model considered previously. The response displacement of this model to the FSP 14 Hz DSF input is shown in Figure 6.34. The corresponding response accelerations are shown in Figure 6.35. The simulation was run twice for the preset acceleration limits of 5 and 15 g peak. The response displacement with a FSP inner bottom input is shown in Figure 6.36. The corresponding response accelerations are shown in Figure 6.37. Again the simulation was run twice for the preset acceleration limits of 5 and 15 g peak.

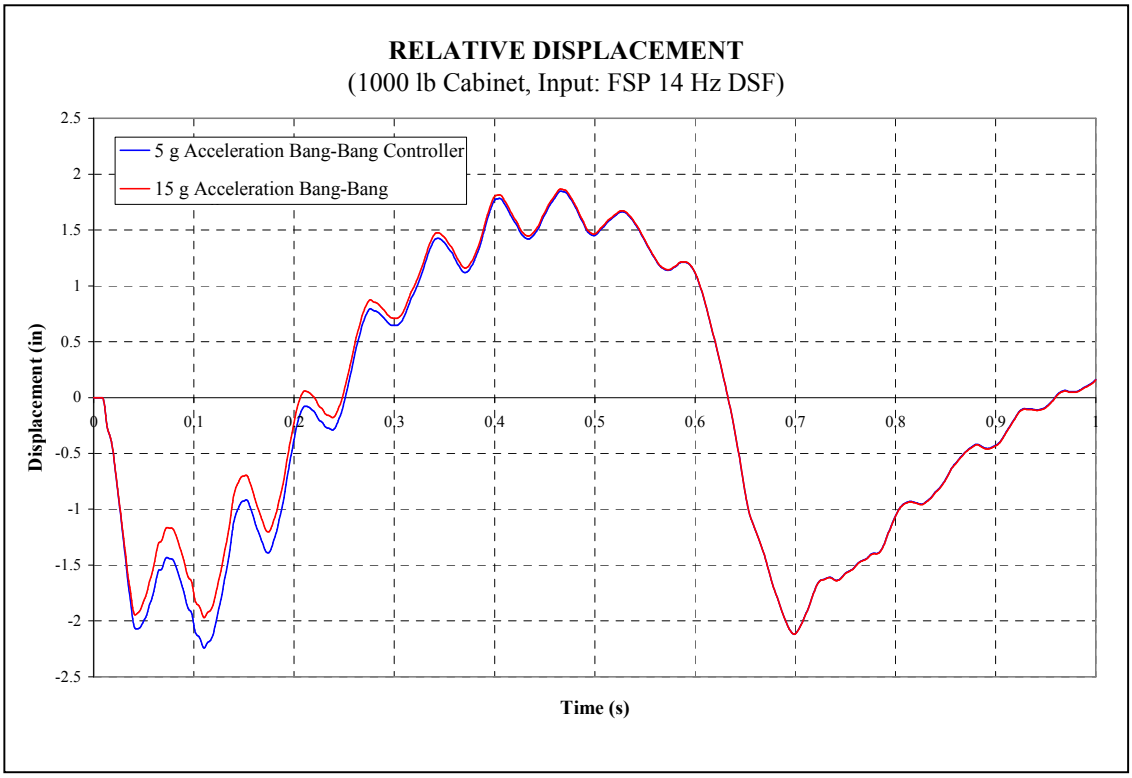


**Figure 6.34**: Case Study 1 (Relative Displacement, FSP DSF Input)

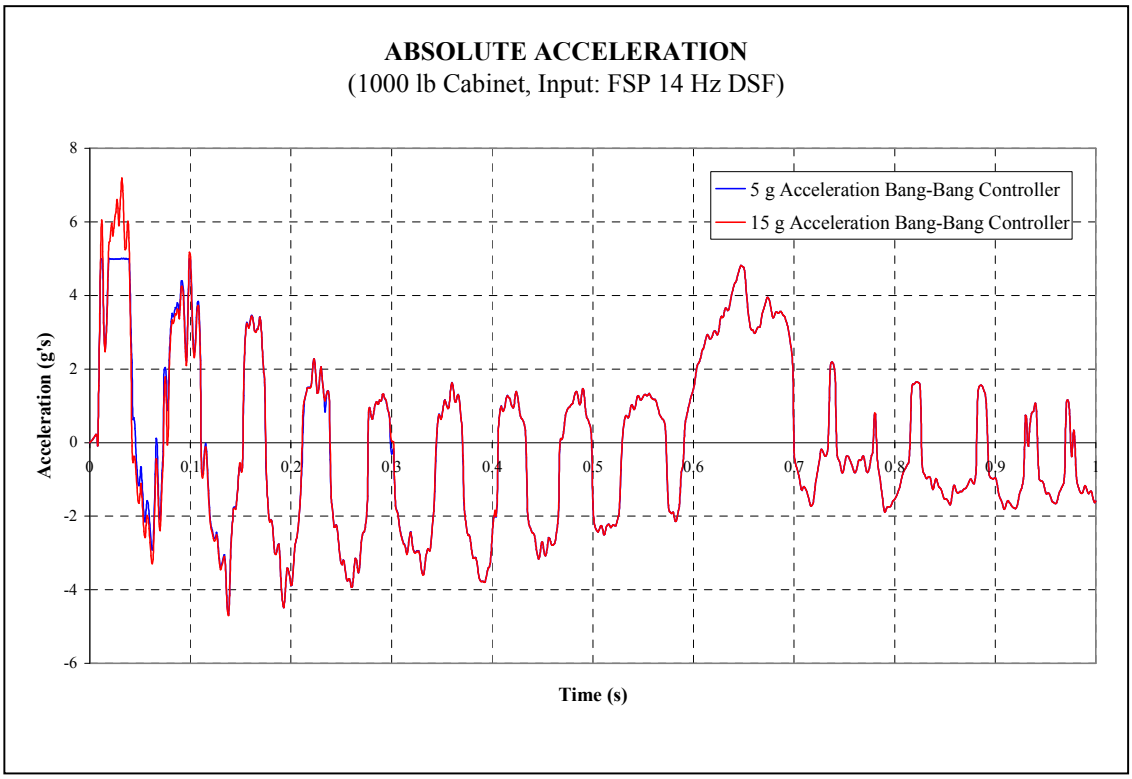


**Figure 6.35**: Case Study 1 (Absolute Acceleration, FSP DSF Input)

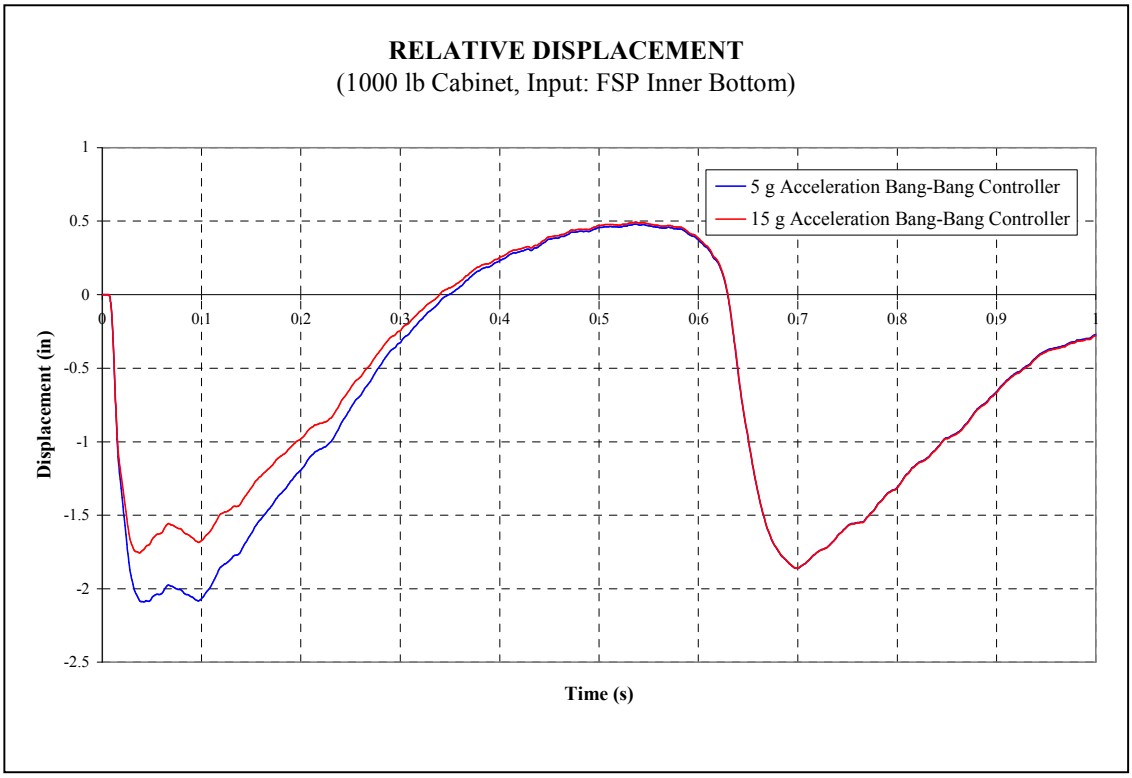


**Figure 6.36**: Case Study 1 (Relative Displacement, FSP Inner Bottom Input)

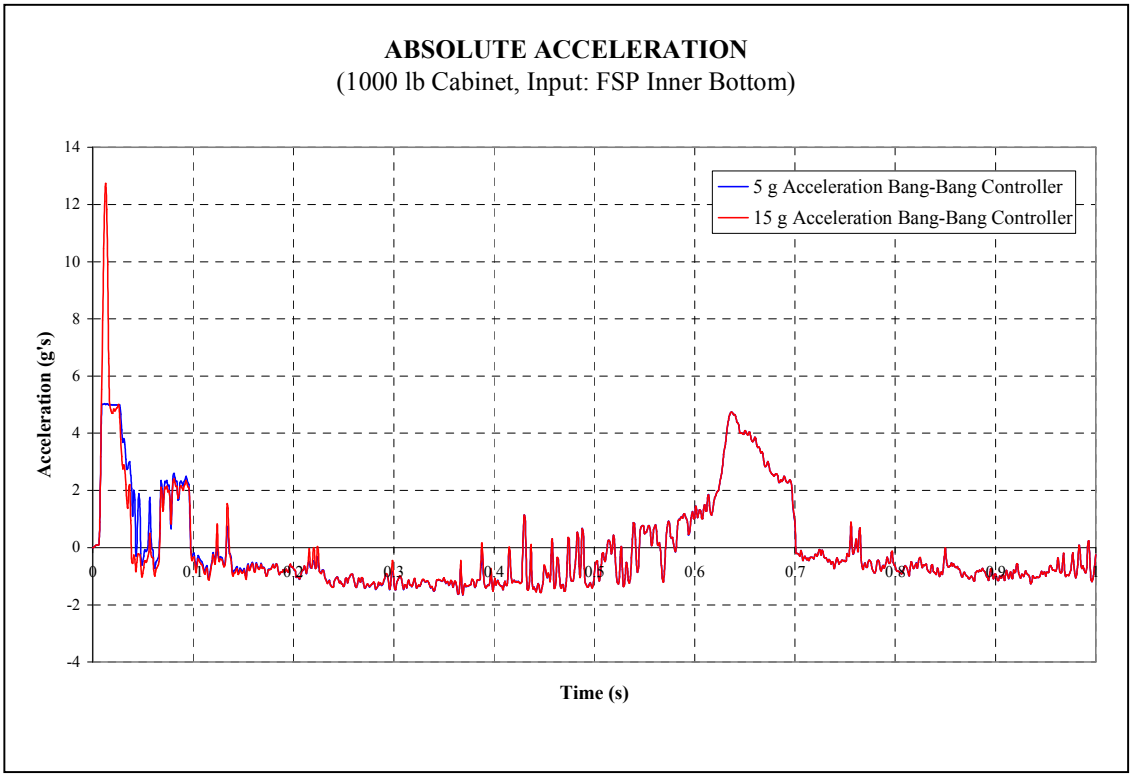


**Figure 6.37**: Case Study 1 (Absolute Acceleration, FSP Inner Bottom Input)

From the figures it can be seen that the response in terms of both above mount acceleration and relative displacement is excellent. It should be noted that the typical response to these inputs using a standard passive mount would be approximately 15 g's above mount with 3 inches of deflection. Therefore, in comparison, the response of the subject isolation system is a significant improvement over current passive technologies. It should also be noted that the isolation system is capable of limiting the above mount response to 5 g's, which is the current, unofficial design goal in shipboard isolation system design. It is anticipated that an isolation system that could achieve 5 g's above mount could minimize, or even eliminate, qualification testing of shipboard COTS equipment. This is based on ongoing fragility testing of COTS equipment which suggests that any COTS equipment can survive a 5 g input.

## 6.9.2 Equipment Raft Isolation Performance

The second test case involves the shock isolation of a hypothetical 10,000 lb equipment raft using a 2 Hz air spring system and 80 MR dampers. The large number of dampers is necessary to generate the required damping force. Since the only validated damper model available is that of the Lord damper used in this study, increasing the number of dampers is the only option to generate greater damping forces. Figure 6.38 shows how the peak damping force versus displacement behavior varies as the number of dampers is increased.

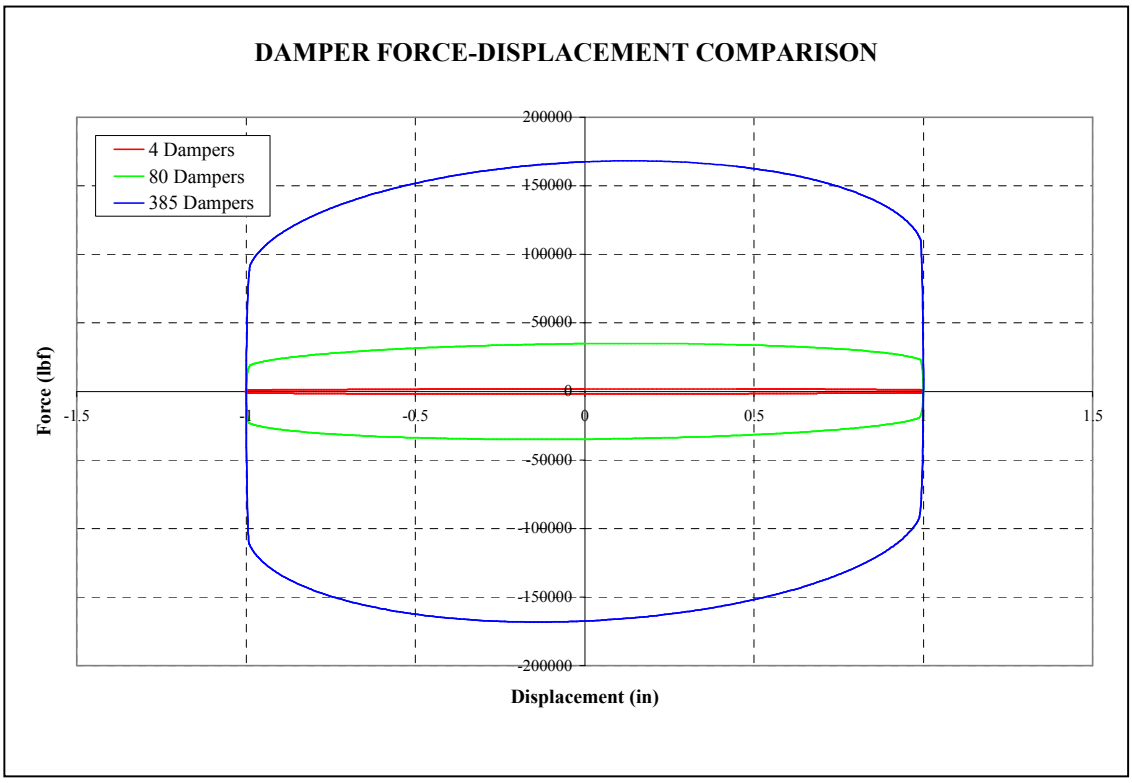


**Figure 6.38**: Damper Force versus Displacement Behavior

The model is otherwise equivalent to the single degree-of-freedom base excitation model considered previously. The response displacement of this model to the FSP 14 Hz DSF input using a 15 g limiting Acceleration Bang-Bang controller is shown in Figure 6.39. The corresponding response accelerations are shown in Figure 6.40. The simulation was run twice for the preset acceleration limits of 5 and 15 g peak. The response displacement of this model to the FSP 14 Hz DSF input using a 5 g limiting Acceleration Bang-Bang controller is shown in Figure 6.41. The corresponding response accelerations are shown in Figure 6.42. The response displacement of the model to an FSP Inner Bottom input using a 15 g limiting Acceleration Bang-Bang controller is shown in Figure 6.43. The corresponding response accelerations are shown in Figure 6.44. The response displacement of the model to an FSP Inner Bottom input using a 5 g limiting Acceleration Bang-Bang controller is shown in Figure 6.45. The corresponding response accelerations are shown in Figure 6.46. Note that the response plots were combined for test cases 2 and 3.

From the figures it can be seen that the isolation system does an excellent job of isolating both of the inputs. For the DSF inputs the 5g Bang-Bang controlled isolation system achieved a response of <2.5 inches while successfully limiting the above mount acceleration to 5 g's. The 15g controlled system achieved a response of <1.5 inches and an above mount response of <12 g's. For the inner bottom inputs the 7g Bang-Bang controlled isolation system achieved a response of <1.8 inches while successfully limiting the above mount acceleration to 7 g's. The 15g controlled system achieved a response of <1.4 inches while limiting the above mount response to 15 g's.

## 6.9.3 Deck Isolation Performance

The final test case involves the shock isolation of a hypothetical 50,000 lb deck using a Newport News developed air spring system (LPAM) and 385 MR dampers. This very large number of dampers is necessary to generate the required damping force. Again, since the only validated damper model available is that of the Lord damper used in this study, increasing the number of dampers was the only option to generate the large damping forces required.

As in the pervious cases, the model is otherwise equivalent to the single degree-of-freedom base excitation model considered previously. The response displacement of this model to the FSP 14 Hz DSF input using a 15 g limiting Acceleration Bang-Bang controller is shown in Figure 6.39. The corresponding response accelerations are shown in Figure 6.40. The simulation was run twice for the preset acceleration limits of 5 and 15 g peak. The response displacement of this model to the FSP 14 Hz DSF input using a 5 g limiting Acceleration Bang-Bang controller is shown in Figure 6.41. The corresponding response accelerations are shown in Figure 6.42. The response displacement of the model to an FSP Inner Bottom input using a 15 g limiting Acceleration Bang-Bang controller is shown in Figure 6.43. The corresponding response accelerations are shown in Figure 6.44. The response displacement of the model to an

FSP Inner Bottom input using a 5 g limiting Acceleration Bang-Bang controller is shown in Figure 6.45. The corresponding response accelerations are shown in Figure 6.46.

Curiously the response of the Case 3 simulations was very similar to the Case 2 simulations. Again from the figures it can be seen that the isolation system does an excellent job of isolating both of the inputs. For the DSF inputs the 5g Bang-Bang controlled isolation system achieved a response of <2.5 inches while successfully limiting the above mount acceleration to 5 g's. The 15g controlled system achieved a response of <1.5 inches and an above mount response of <12 g's. For the inner bottom inputs the 7g Bang-Bang controlled isolation system achieved a response of <1.8 inches while successfully limiting the above mount acceleration to 7 g's. The 15g controlled system achieved a response of <1.4 inches while limiting the above mount response to 15 g's.

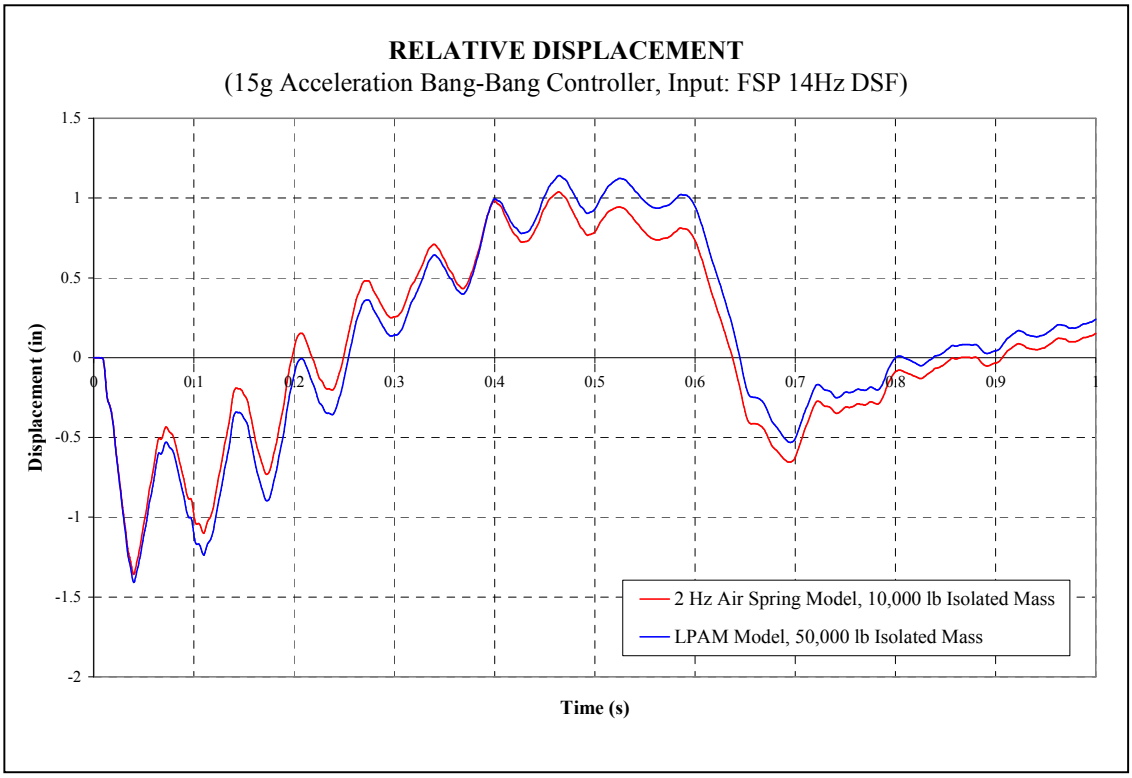


**Figure 6.39**: Case Study 2 & 3 (Relative Displacement, 15g Controller, FSP DSF Input)

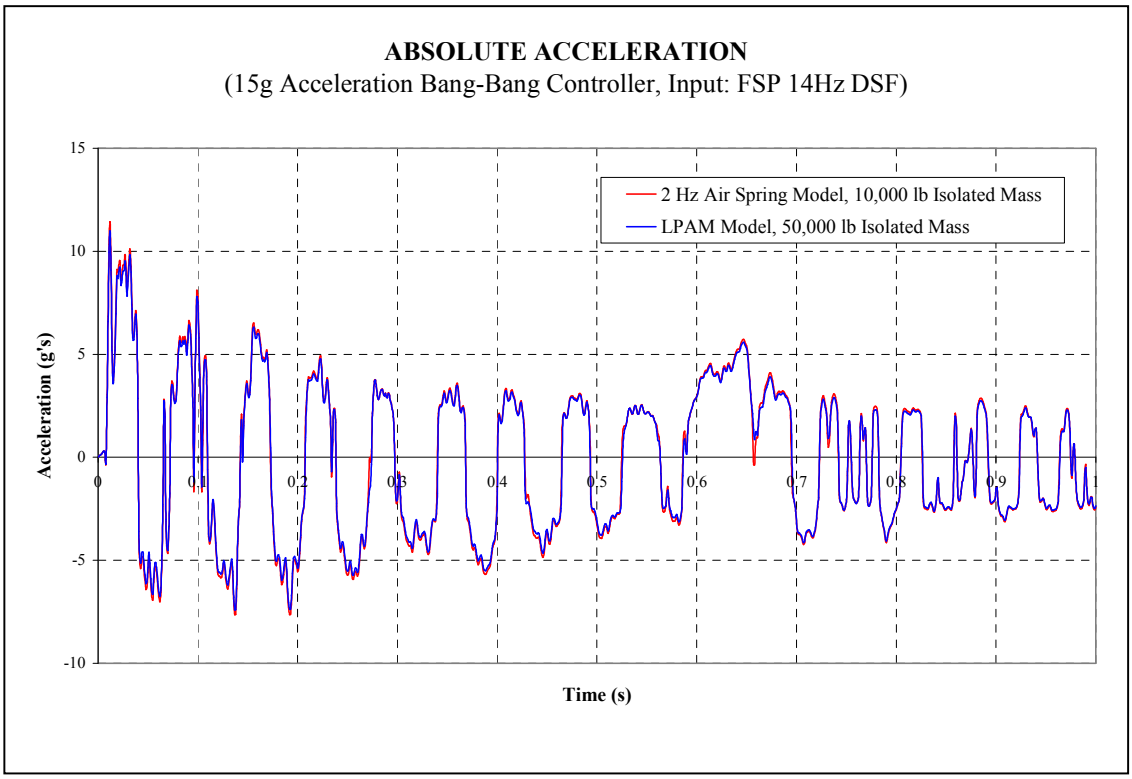


**Figure 6.40**: Case Study 2 & 3 (Absolute Acceleration, 15g Controller, FSP DSF Input)

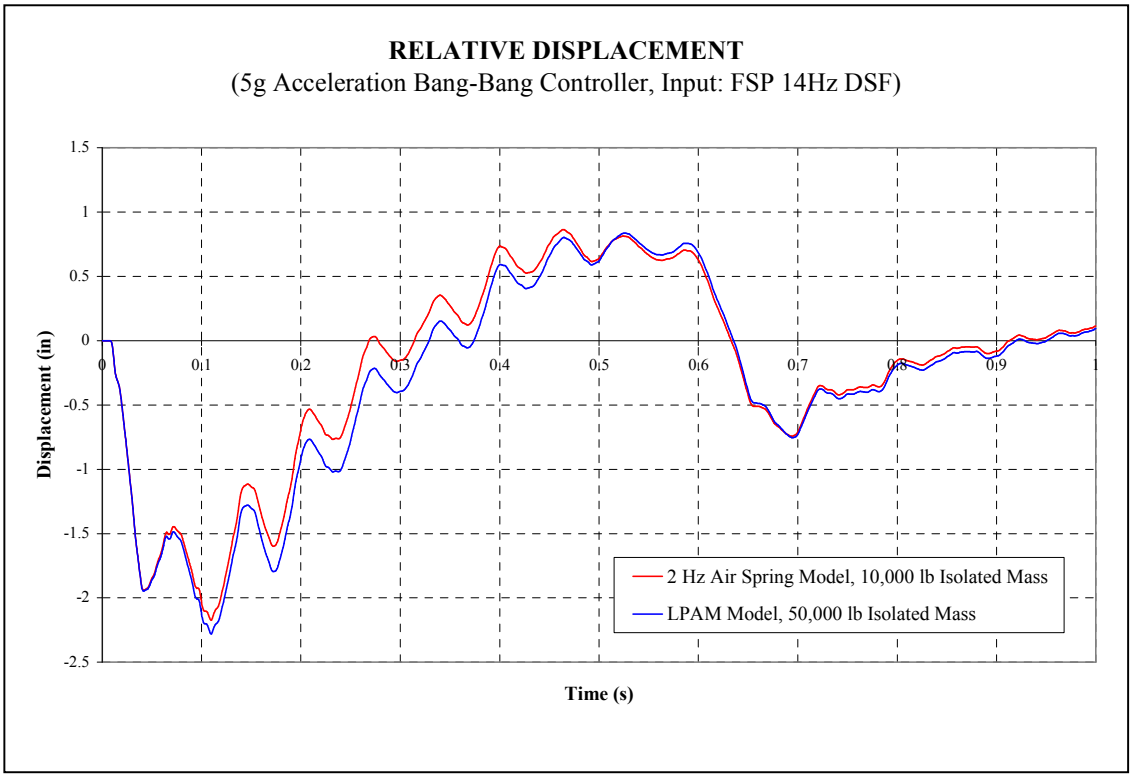


**Figure 6.41**: Case Study 2 & 3 (Relative Displacement, 5g Controller, FSP DSF Input)

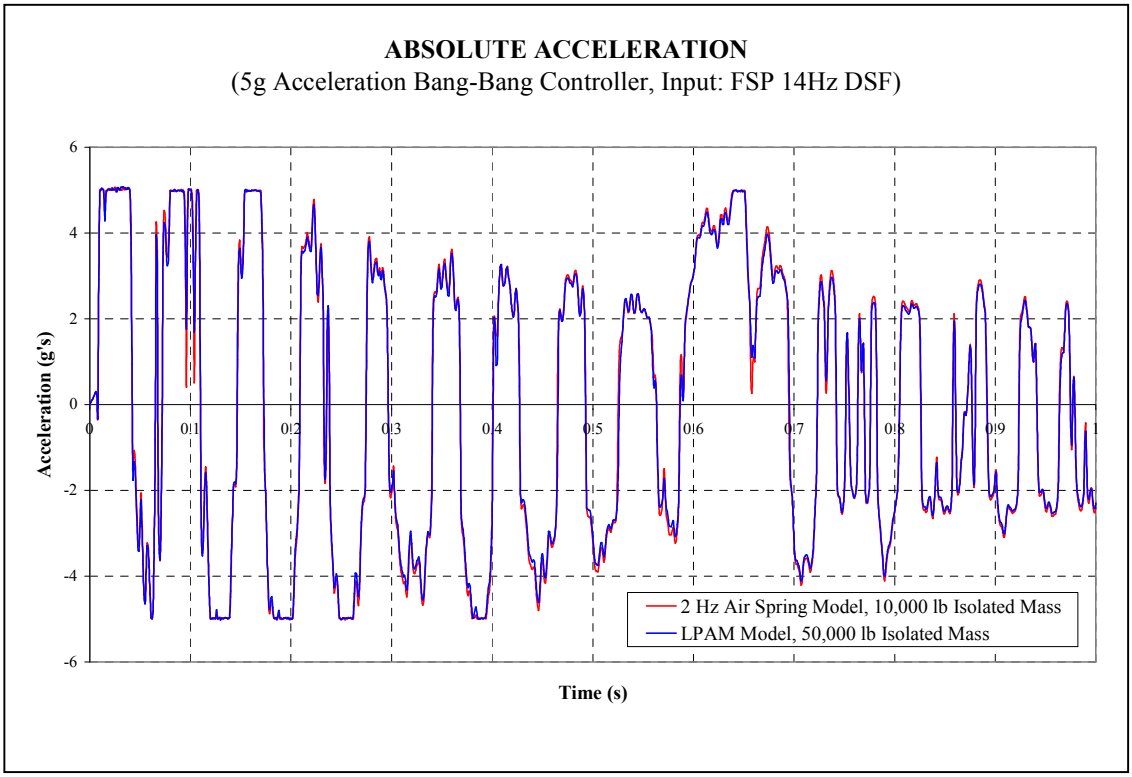


**Figure 6.42**: Case Study 2 & 3 (Absolute Acceleration, 5g Controller, FSP DSF Input)

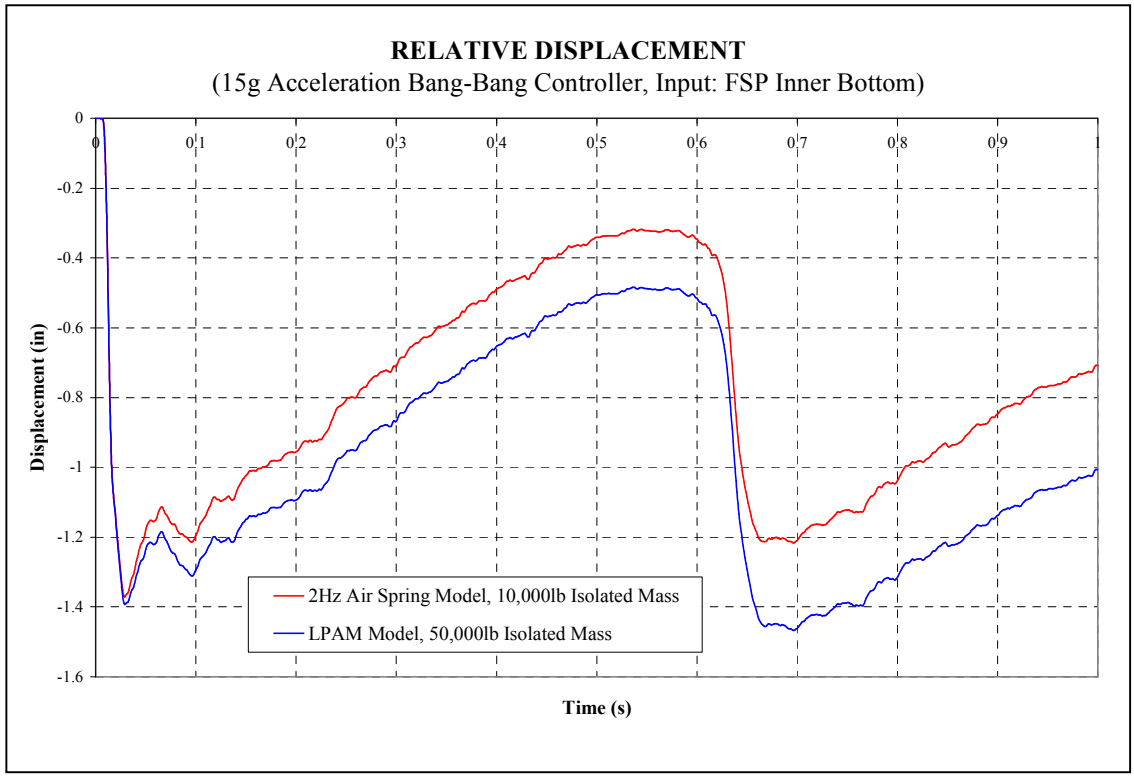


**Figure 6.43**: Case Study 2 & 3 (Relative Displacement, 15g Controller, FSP IB Input)

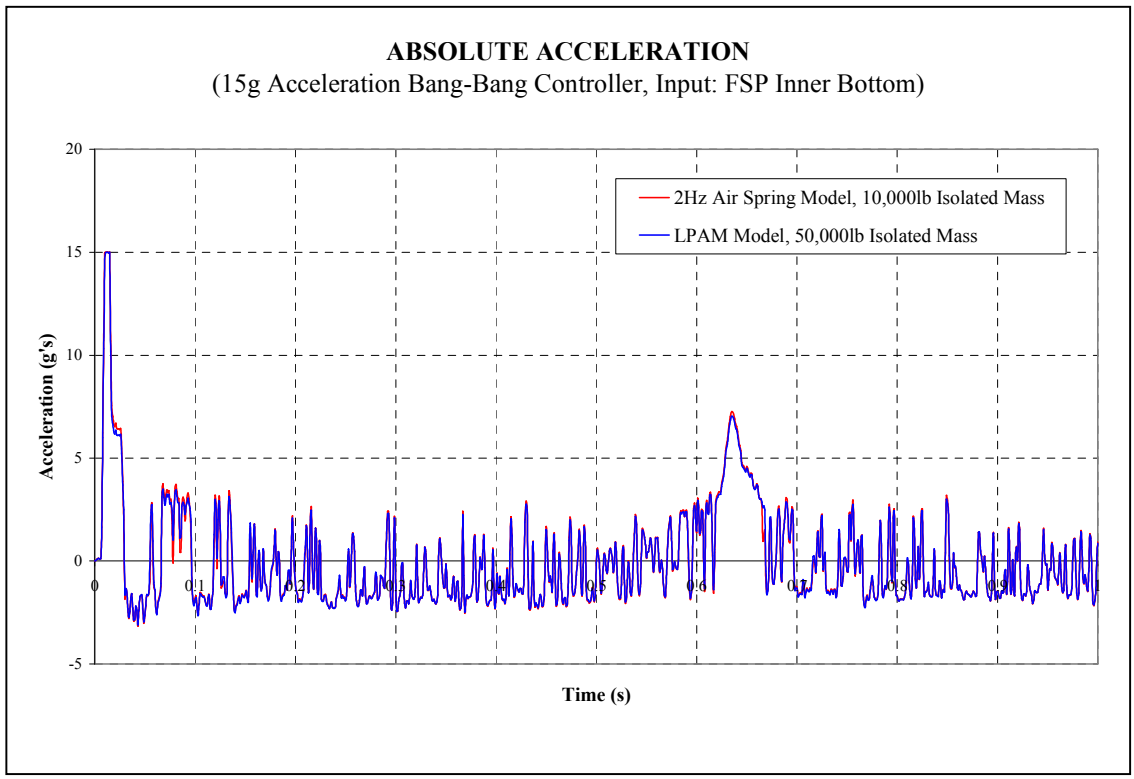


**Figure 6.44** Case Study 2 & 3 (Absolute Acceleration, 15g Controller, FSP IB Input)

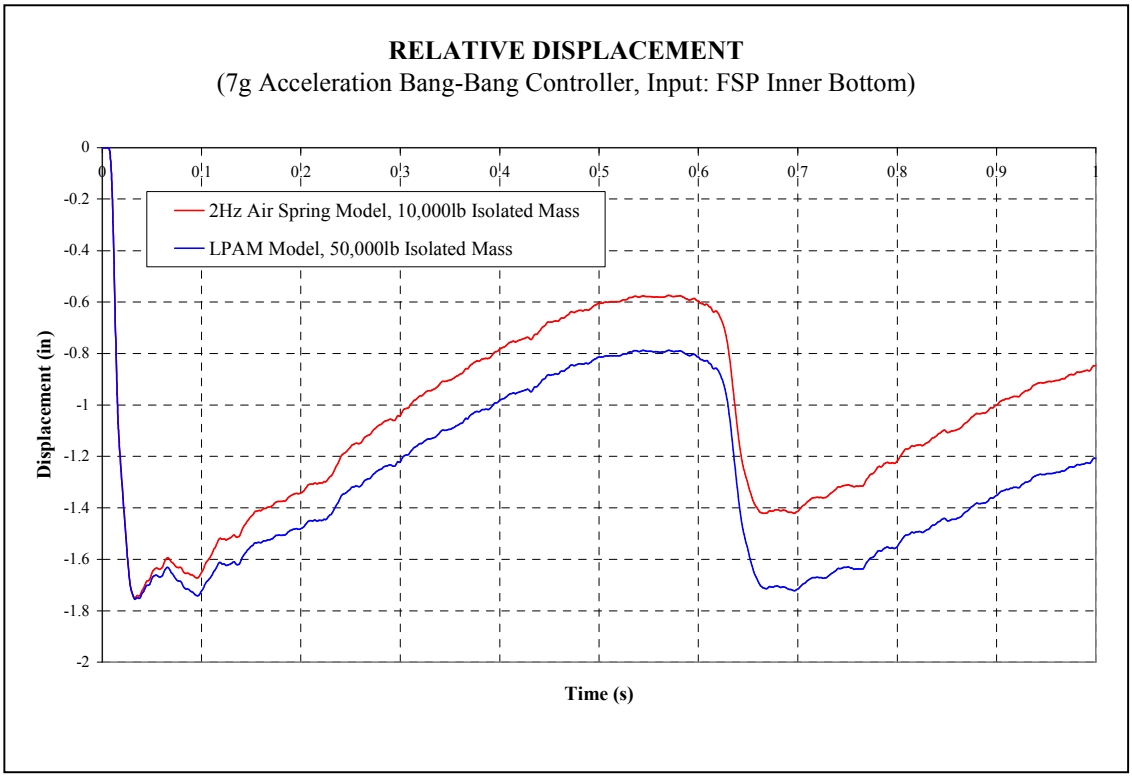


**Figure 6.45** Case Study 2 & 3 (Relative Displacement, 7g Controller, FSP IB Input)

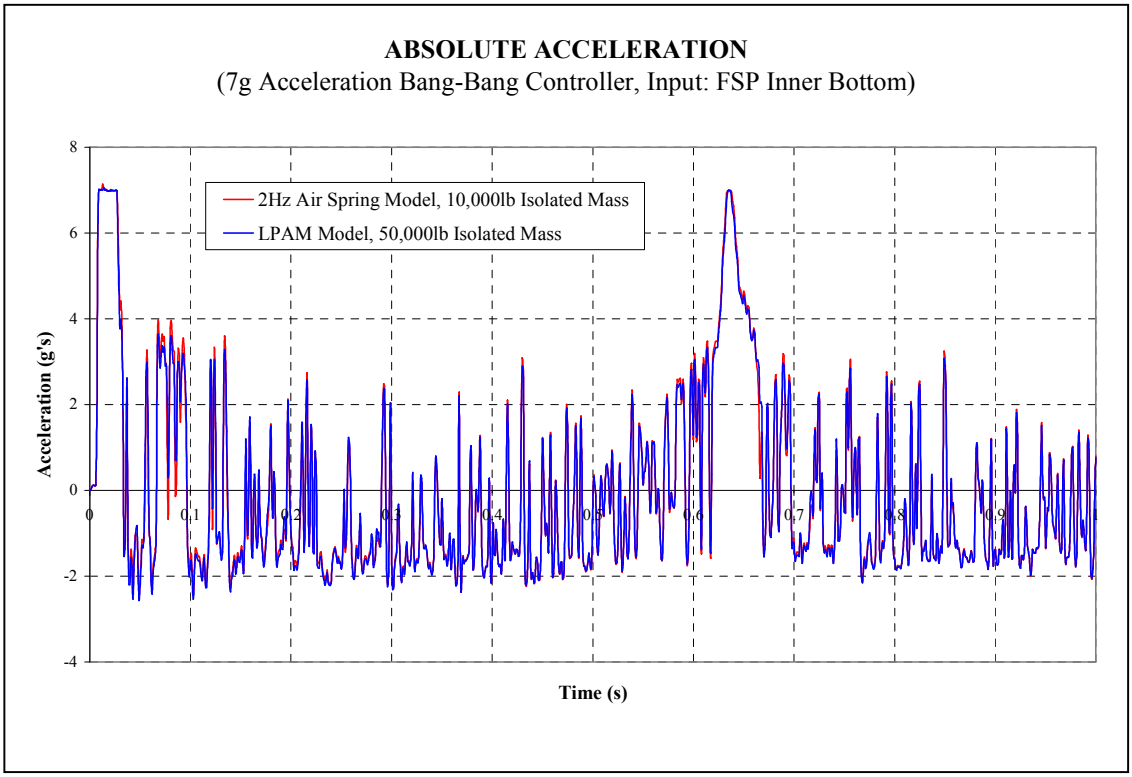


**Figure 6.46** Case Study 2 & 3 (Absolute Acceleration, 7g Controller, FSP IB Input)

# 6.10 Vibration Isolation Performance

In order to examine the vibration isolation performance of the combined isolator, the force transmissibility was plotted for the air spring only and for the air spring with the addition of the MR dampers in passive off (i.e., zero volts applied to the current driver) mode. This was done to determine if there was a negative effect of adding the MR damper on the vibration isolation effectiveness. No voltage was applied to the damper since the most effective vibration isolation performance will be achieved with minimum damping. The input to the model was an above mount sinusoidal force of varying driving frequencies. The transmissibility ratio was then plotted versus the frequency ratio as shown in Figure 6.47.

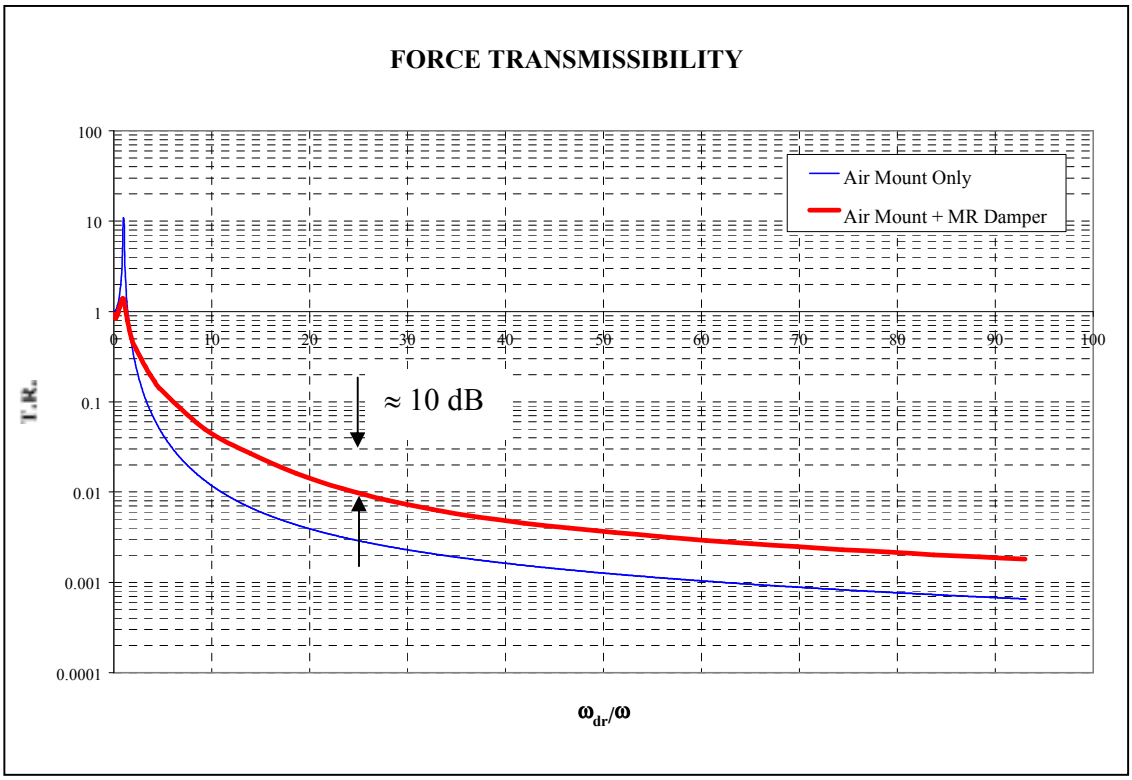


**Figure 6.47**: Force Transmissibility Comparison

From Figure 6.47 it is clear that the addition of the MR damper decreases the transmissibility at resonance and increases the transmissibility at all frequencies above the resonant frequency over the air spring alone. This is the typical result expected of

adding a damper to a SDOF system. While the transmissibility was increased at frequencies above resonance, the magnitude of the increase was only on the order of 10 dB. While a 10 dB degradation in vibration isolation performance is not insignificant, it is not enough to invalidate the effectiveness of this device as a vibration isolator. Actually the 10 dB reduction is surprising as the commercial MR damper is fairly stiff and uses high friction seals. Note that with the MR damper, the combined isolator is still very effective above 10 Hz which corresponds to a frequency ratio of approximately 4.4 based on the 2.27 Hz natural frequency of the air mount.

## 6.11 Chapter Summary

An air mount can be a very effective vibration isolator, but tends to behave poorly as a shipboard shock isolator due to the fact that shock inputs tend to drive an air spring into resonance after the initial shock transient. Air mounts can offer a significant reduction in transmitted acceleration during initial transients, but following the initial transient resonance results in large relative displacements. In many applications these large mount deflections are unacceptable. Adding a controlled MR damper offers a significant reduction in mount deflection and a simultaneous significant reduction in transmitted acceleration. The LQR Optimal, Velocity Feedback and Acceleration Bang-Bang controllers appear to provide very effective control of the MR damper with shock inputs. The results suggest that this hybrid isolation system could reduce transmitted accelerations below the 7 to 8 g level for introduction of so-called Commercial-Grade COTS equipment on ships. Introducing Commercial-Grade COTS equipment could conceivably offer significant reductions in equipment costs. The air spring/MR damper combination with any of the controllers provides excellent isolation performance for both shock and vibration inputs simultaneously.

Combining vibration and shock isolation into a single unit can offer significant advantages in terms of weight and space savings. This is particularly important in submarine applications where space is at a premium. Using semi-active control allows

the isolation system to automatically adjust to variations in the mass and center-of-gravity of the supported payload. This is particularly important as electronic equipment is typically refreshed every 18 months which obviously alters the mass and center-of-gravity of the isolated equipment. This forces a re-evaluation and/or replacement of the isolation system every 18 months. This can be very costly and time consuming. Having an isolation system that automatically accounts for these variations is obviously advantageous.

Although semi-active devices require a power source, MR devices are attractive in that they have low power requirements and without power they still behave as passive dampers. The later affords a degree of fail-safety to an MR damper-based isolation system. Another benefit of having low power requirements is that it may be possible to create a self-powered device. Having a self-powered, self-contained, combined shock and vibration isolator would be especially attractive as it would eliminate the need for external power sources and external controller connections. Chapter 8 explores the scavenging and storage of ambient shipboard vibration energy with the self-powering of this mount in mind.

# Chapter 7

# MRAM Multi-Degree-of-Freedom Performance

## 7.1 Multi-Degree-of-Freedom System Modeling

The results presented in [91, 92] suggested that the subject isolation system consisting of a controllable MR damper in parallel with an air spring was quite effective in controlling the response of an isolated item subjected to a typical ship shock input. Furthermore, it was shown that the addition of the dampers did not significantly decrease the vibration isolation performance of the isolation system. While these results were promising, the performance of the mount in an actual MDOF isolation system as would be encountered in a shipboard application would need to be determined before the system could be considered viable. To determine the MDOF performance of the isolation system, a three degree-of-freedom (3DOF) model of a typical shipboard equipment rack was developed as shown in Figure 7.1. A 3DOF model adequately describes the cabinet motion since the majority of the input energy in a shipboard shock event occurs in the vertical and athwartship directions. Thus very little translation occurs in the excluded axis and very little rotation occurs about the remaining two rotational axes and the full six degrees-of-freedom collapses to three degrees-of-freedom.

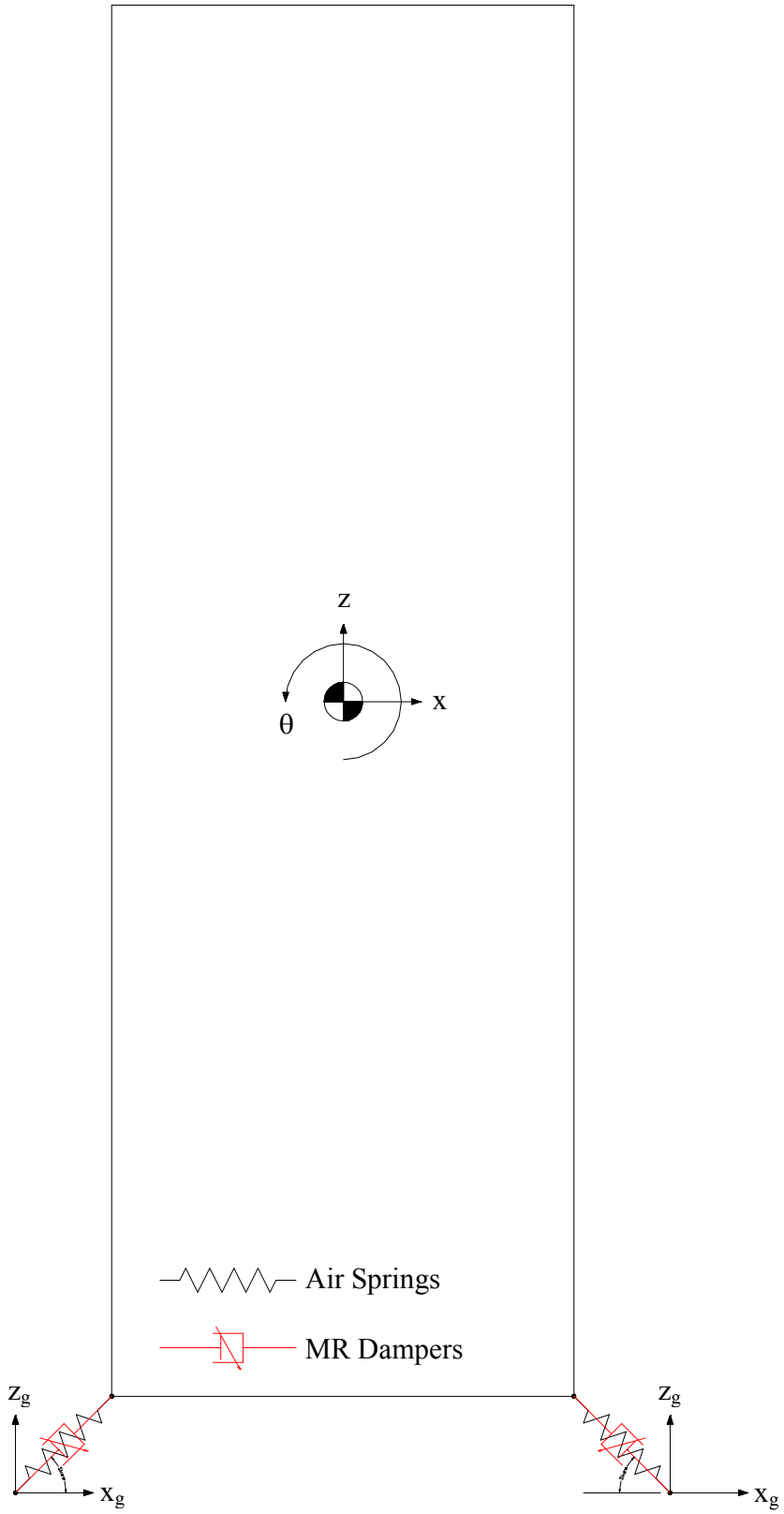


**Figure 7.1**: 3DOF System Model

The model represents a relatively tall and narrow (24 in. wide by 72 in. tall) equipment cabinet weighing 1000 lbs whose center-of-gravity is located at the geometric center of the cabinet. The cabinet is entirely base mounted using four air springs and four MR dampers that have been skewed at an angle as shown in the figure. This allows the dampers to produce force in both axes. Also, skewing the air springs produces a more laterally stable system as air springs tend to be considerable less stiff in the lateral direction. The input to the system consisted of vertical ($z_g$) and athwartship ($x_g$) velocities derived directly from an actual FSP test. The FSP deck was tuned to 14 Hz in this test. The output of the simulation consisted of vertical (z) and lateral (x) displacements and accelerations of the cabinet at the center-of-gravity, rotational angle about the y axis, as well as relative displacements of the cabinet in both the $x$ and $z$ directions.

Figure 7.2 shows how the spring force of the model shown in Figure 7.1 can be broken into $x$ and $z$ components. Among other things, breaking the spring force down into components allows equations of motion to be derived more easily.

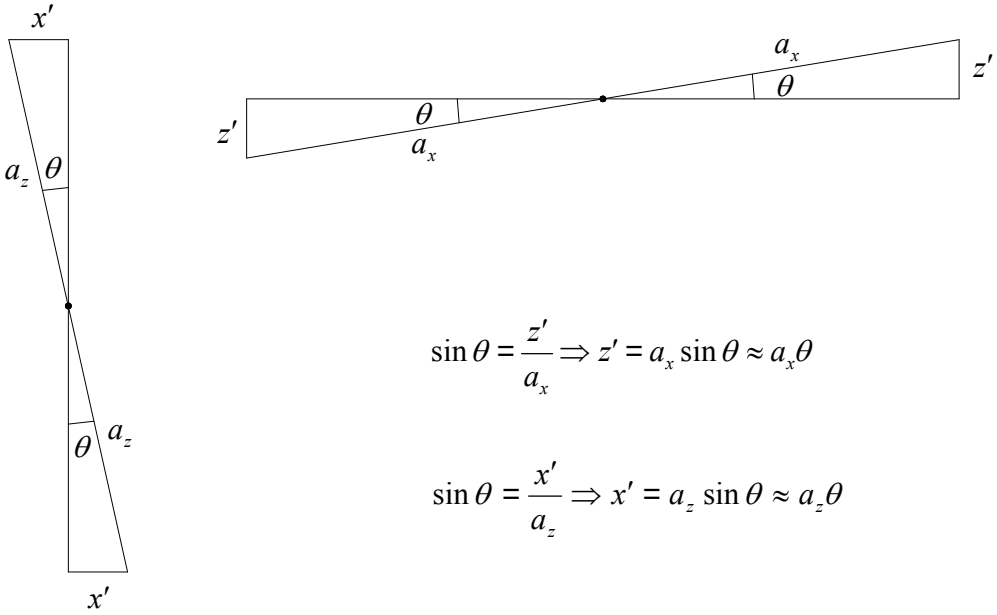


$$\sin\theta = \frac{z'}{a_x} \Rightarrow z' = a_x \sin\theta \approx a_x\theta$$

$$\sin\theta = \frac{x'}{a_z} \Rightarrow x' = a_z \sin\theta \approx a_z\theta$$

**Figure 7.2**: Spring Deflection Due to Cabinet Rotation

Mathematically this system can be described by a system of three differential equations (One describing each degree of freedom) which can be derived using any suitable method. For example, using Lagrange's equations of motion the equations can be derived as follows:

First consider the kinetic energy of the system. The kinetic energy is due to both the translation and the rotation of the cabinet. The kinetic energy due to translation is:

$$T_t = \frac{1}{2} m\dot{x}^2 + \frac{1}{2} m\dot{z}^2 \tag{7.1}$$

where $m$ is the mass of the cabinet and $\dot{x}$ and $\dot{z}$ are the velocities of the center-of-gravity of the cabinet, respectively. The kinetic energy due to rotation is,

$$T_r = \frac{1}{2} I_{yy}\dot{\theta}^2 \tag{7.2}$$

where $I_{yy}$ is the mass moment of inertia of the cabinet about the $y$ axis and $\theta$ is the angle of rotation of the cabinet about the same axis. Therefore, the total kinetic energy of the system is,

$$T = T_t + T_r = \frac{1}{2} m\dot{x}^2 + \frac{1}{2} m\dot{z}^2 + \frac{1}{2} I_{yy}\dot{\theta}^2 \tag{7.3}$$

The potential energy is due entirely to the deflection of the spring elements. The deflection of the spring elements is due to both the translation and rotation of the cabinet. Figure 7.2 graphically depicts the deflection of the spring elements due to the cabinet rotation which must be taken into account in the total defection of each spring.

From the figure it can be seen that the rotation of the cabinet contributes to the $x$ spring deflection as,

$$x' = a_z\theta \tag{7.4}$$

and the $z$ spring deflection as,

$$z' = a_x\theta \tag{7.5}$$

Therefore, the total potential energy due to spring deflection is,

$$V = 2\cdot\frac{1}{2}k_x\left(x - x_g + a_z\theta\right)^2 + \frac{1}{2}k_z\left(z - z_g - a_x\theta\right)^2 + \frac{1}{2}\left(z - z_g + a_x\theta\right)^2 \tag{7.6}$$

where $k_x$ and $k_z$ are the stiffness of the springs in the $x$ and $z$ directions, respectively. Forming the Lagrangian,

$$\begin{aligned} L &= T - V \\ &= \frac{1}{2}m\dot{x}^2 + \frac{1}{2}m\dot{z}^2 + \frac{1}{2}I_{yy}\dot{\theta}^2 \\ &- k_x\left(x^2 - 2xx_g + 2a_z\theta x - 2a_z\theta x_g + a_z^2\theta^2 + x_g^2\right) \\ &- k_z\left(z^2 - 2zz_g + a_x^2\theta^2 + z_g^2\right) \end{aligned} \tag{7.7}$$

Now, Lagrange's equations are,

$$\frac{d}{dt}\left(\frac{\partial L}{\partial \dot{q}_k}\right) - \frac{\partial L}{\partial q_k} = Q_k \tag{7.8}$$

where $q_k$ represents the $k$ generalized coordinates (in this case $x$, $z$ and $\theta$) and $Q_k$ are the non-conservative forces, such as damping forces, associated with each coordinate. Therefore, it follows that Lagrange's equations of motion can be written,

$$1)\ \frac{d}{dt}\left(\frac{\partial L}{\partial \dot{x}}\right) - \frac{\partial L}{\partial x} = F_{d,x} \tag{7.9}$$

$$2)\ \frac{d}{dt}\left(\frac{\partial L}{\partial \dot{z}}\right)-\frac{\partial L}{\partial z}=F_{d,z} \tag{7.10}$$

$$3)\ \frac{d}{dt}\left(\frac{\partial L}{\partial \dot{\theta}}\right)-\frac{\partial L}{\partial \theta}=0 \tag{7.11}$$

or, upon substitution,

$$1)\ \frac{d}{dt}\left(\frac{\partial L}{\partial \dot{x}}\right)-\frac{\partial L}{\partial x}=m\ddot{x}+2k_x x-2k_x x_g+2k_x a_z\theta=F_d\cos\alpha \tag{7.12}$$

$$2)\ \frac{d}{dt}\left(\frac{\partial L}{\partial \dot{z}}\right)-\frac{\partial L}{\partial z}=m\ddot{z}+2k_z z-2k_z z_g=F_d\sin\alpha \tag{7.13}$$

$$3)\ \frac{d}{dt}\left(\frac{\partial L}{\partial \dot{\theta}}\right)-\frac{\partial L}{\partial \theta}=I_{yy}\ddot{\theta}+2k_x a_z x-2k_x a_z x_g+2k_x a_z^2\theta+2k_z a_x^2\theta=0 \tag{7.14}$$

The above can be written in terms of relative motion with respect to ground using the substitutions,

$$x=x_r+x_g \tag{7.15}$$

and,

$$z=z_r+z_g \tag{7.16}$$

where $x_r$ and $z_r$ represent the relative motion of the center-of-gravity (CG) of the cabinet to the base in the $x$ and $z$ (lateral and vertical) directions respectively, $\theta$ is the rotation angle of the cabinet about the CG (in radians), $x_g$ and $z_g$ represent the $x$ and $z$ base motions respectively, $F_d$ represents the damping force, $\alpha$ is the skew angle of the mounts, $m$ is the mass of the cabinet, $k_x$ and $k_z$ represent the stiffness of the air spring in the $x$ and $z$ directions respectively, $a_x$ and $a_z$ is the distance from the CG to the

point of application of the mount force in the $x$ and $z$ directions respectively, and $I_{yy}$ is the mass moment of inertia of the cabinet about the $y$ axis. The resulting equations of motion in terms of relative motion are,

$$1)\ \ddot{x}_r + \frac{2k_x}{m}x_r + \frac{2k_x a_z}{m}\theta = \frac{F_d \cos\alpha}{m} - \ddot{x}_g \tag{7.17}$$

$$2)\ddot{z}_r + \frac{2k_z}{m}z_r = \frac{F_d \sin\alpha}{m} - \ddot{z}_g \tag{7.18}$$

$$3)\ \ddot{\theta} + \frac{2k_x a_z}{I_{yy}}x_r + \left(\frac{2k_x a_z^2 + 2k_z a_x^2}{I_{yy}}\right)\theta = 0 \tag{7.19}$$

Note that Equations (7.17) and (7.19) are coupled, but Equation (7.18) is independent. This makes physical sense as only the lateral base input induces any rotation in the cabinet.

The damper was modeled using the Modified Bouc-Wen model as described in [91, 92]. This model has been previously validated in several papers and independently by the authors under shock loading. The damper, as well as the air springs, were skewed at the angle $\alpha$ to provide multi-axis damping and spring forces.

## 7.2 MDOF Control Algorithms

Three controllers were used in the simulations including two new controller concepts developed by the author. For comparison purposes a Skyhook controller was included that had been modified for MDOF applications. The controllers used in the simulations are described below.

## 7.2.1 MDOF Skyhook Controller

Skyhook controllers have been used in several applications involving the use of MR dampers in SDOF isolation systems. To adapt the Skyhook controller for use in MDOF applications required some slight modification to the SDOF algorithm. First consider the SDOF Skyhook algorithm as shown in Table 7.1.

| $\dot{x}$ | $\dot{x}_r$ | **Damper** |
|---|---|---|
| + | + | ON |
| + | – | OFF |
| – | + | OFF |
| – | – | ON |

**Table 7.1**: Skyhook Control Algorithm

This concept can be extended to the MDOF case by applying the above logic in both $x$ and $z$ directions and then logically combining the resulting output according to the following logic table.

| $x$ | $z$ | **Damper** |
|---|---|---|
| ON | ON | ON |
| ON | OFF | OFF |
| OFF | ON | OFF |
| OFF | OFF | OFF |

**Table 7.2**: MDOF Skyhook Logic Table

Note that the result of the above is to turn the dampers on only if both of the SDOF Skyhook algorithms are “ON” simultaneously.

## 7.2.2 MDOF Velocity Feedback Controller

The Velocity Feedback Controller was shown to be very effective in the SDOF case in the previous testing performed in [92]. Two versions of the Velocity Feedback Controller were considered. In the SDOF case the relative velocity of the CG to the base is equivalent to the relative velocity across the damper. This is not necessarily true in the MDOF case, particularly with a skewed damper. Since it was unknown which definition of relative velocity was responsible for the excellent performance observed in the SDOF case, both definitions of relative velocity will be considered in the simulations. Case 1 will use the relative velocity of the CG to the base and Case 2 will use the relative velocity across the damper.

The implementation of the Velocity Feedback Controller is simple. A voltage is fed to the current drivers for the MR dampers that is proportional to the relative velocity as defined above. A gain is applied to the relative velocity signal such that the maximum voltage to the MR dampers corresponds to the peak relative velocity expected from the given input. In the simulations a gain of 0.0355 V/in/s and 0.0140 V/in/s was applied to the relative velocity signals as defined in Case 1 and 2 above, respectively. Note that implementing this controller would only require a measure of the relative velocity which could be easily determined with a Linear Velocity Transducer (LVT).

## 7.2.3 MDOF Acceleration Bang-Bang Controller

The Acceleration Bang-Bang Controller will be shown to be a very effective controller for the MR damper with ship shock inputs. The controller has the added advantage of allowing the above mount peak accelerations to be preset and the mount deflections to be minimized subject to the selected above mount acceleration. This is a very desirable feature in shipboard applications as the designer can specify the above mount environment while simultaneously minimizing rattle space. This is vital in

shipboard applications, particularly onboard submarines, where space is often at a premium.

The principle behind the Acceleration Bang-Bang controller is as follows. Prior to a shock event the dampers are off to provide the most effective vibration isolation performance. At the instant that a shock is detected the dampers turn full on unless the above mount absolute acceleration exceeds the preset value. When the above mount acceleration exceeds the allowable value the damper is switched off until the acceleration level again falls below the acceptable level and the damper is again switched full on. This process continues throughout the shock event. Mathematically this control algorithm can be described as:

$$V = \begin{cases} V_{\max}, & |\ddot{x}| < A * |\ddot{z}| < B \\ 0, & |\ddot{x}| \geq A + |\ddot{z}| \geq B \end{cases} \tag{6.20}$$

where $\ddot{x}$ and $\ddot{z}$ are the measured above mount absolute accelerations in the $x$ and $z$ directions, respectively, $V$ is the voltage applied to the MR damper current driver, $V_{\max}$ is the voltage applied to the current driver that results in the maximum damping force, and $A$ and $B$ are the prescribed acceleration limits in the in the $x$ and $z$ directions, respectively.

SDOF simulations using actual ship shock inputs showed excellent performance with this controller. Note that implementation of this controller would be very simple requiring only a biaxial accelerometer to sense the above mount accelerations and a simple on-off controller to switch the damper on and off according to the sensed acceleration. The MDOF performance will be discussed in the next section.

## 7.3 MDOF Simulation Results

The model was run using test data from a FSP test which utilized a 14 Hz Deck Simulator Fixture (DSF). The input data is shown in terms of velocity in Figure 7.3. For performance comparison simulations were run with the same input using air springs only and with a typical passive isolation system that is used extensively in shipboard applications. The responses were also determined for the Skyhook controller, the Acceleration Bang-Bang controller, and both of the Velocity Feedback controllers. The response relative displacements in both translation directions are shown in Figures 7.4 and 7.5. The corresponding response absolute accelerations are shown in Figures 7.6 and 7.7. The rotations about the $y$ axis are shown in Figure 7.8. Figure 7.9 summarizes the response peaks for each case and Figure 7.10 shows the input to the MR damper current drivers that is output from each of the controllers.

Figure 7.11 is a sample of a video showing the MDOF response for the cabinet supported with air springs only versus the cabinet supported with the MRAM isolator. The frames are sampled at increments of 0.1 seconds resulting in a somewhat choppy appearance. Also plotted is the maximum excursion envelope for the cabinet, i.e., the required rattle space for the cabinet mounted with the two systems. In addition, the real time acceleration (in g's) is plotted (again sampled every 0.1 seconds) for each isolation system. Figure 7.12 is a similar plot with the exception that the cabinet supported with air springs only has been replaced by the same cabinet supported with a commercial passive isolation system.

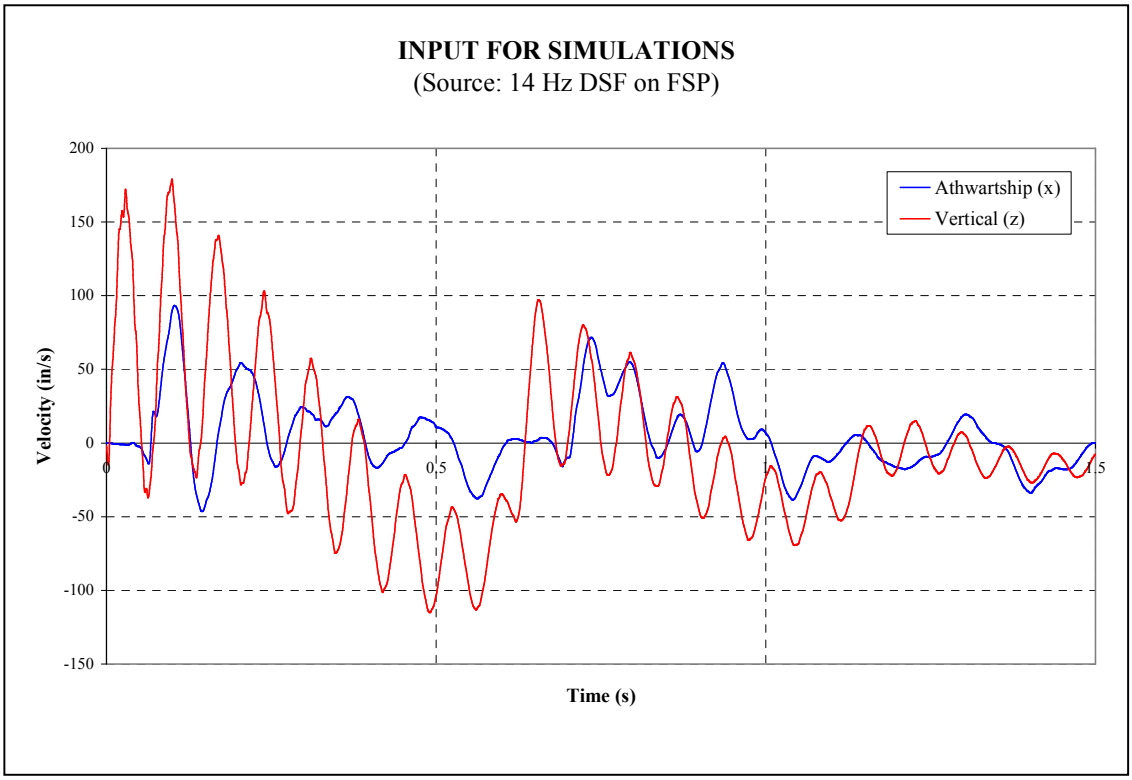


**Figure 7.3**: 14 Hz FSP Input used in the Simulations

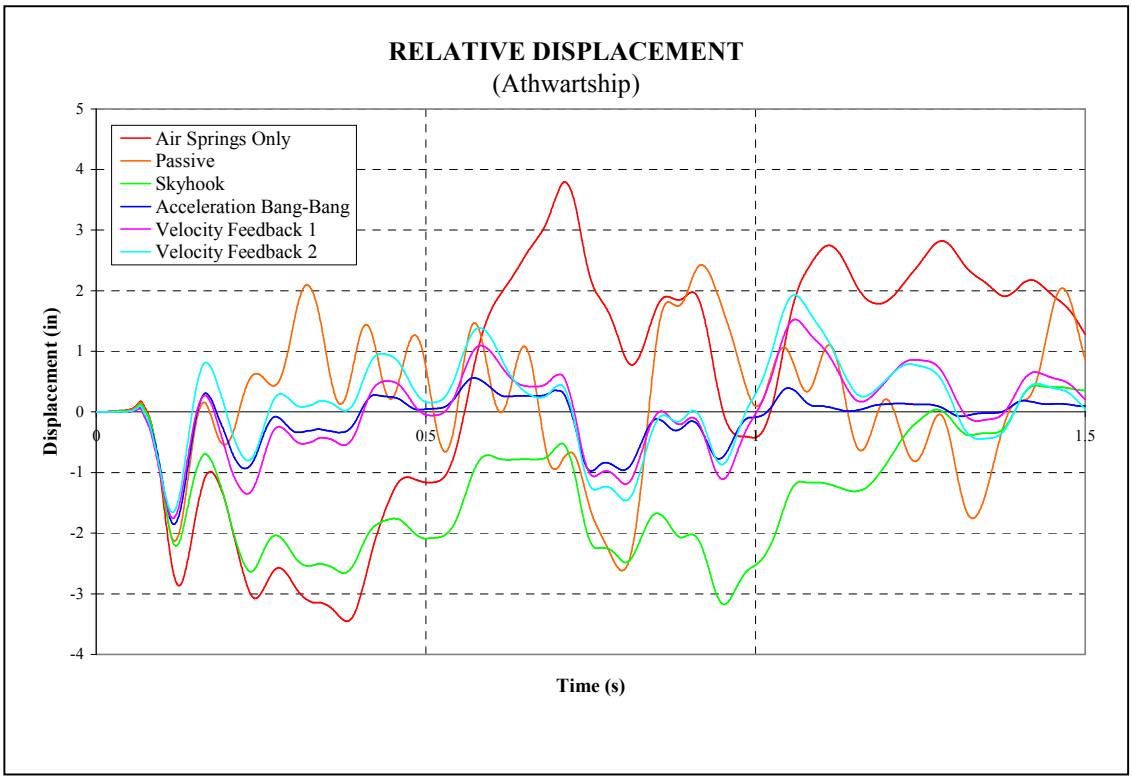


**Figure 7.4**: Athwartship Response (Relative Displacement)

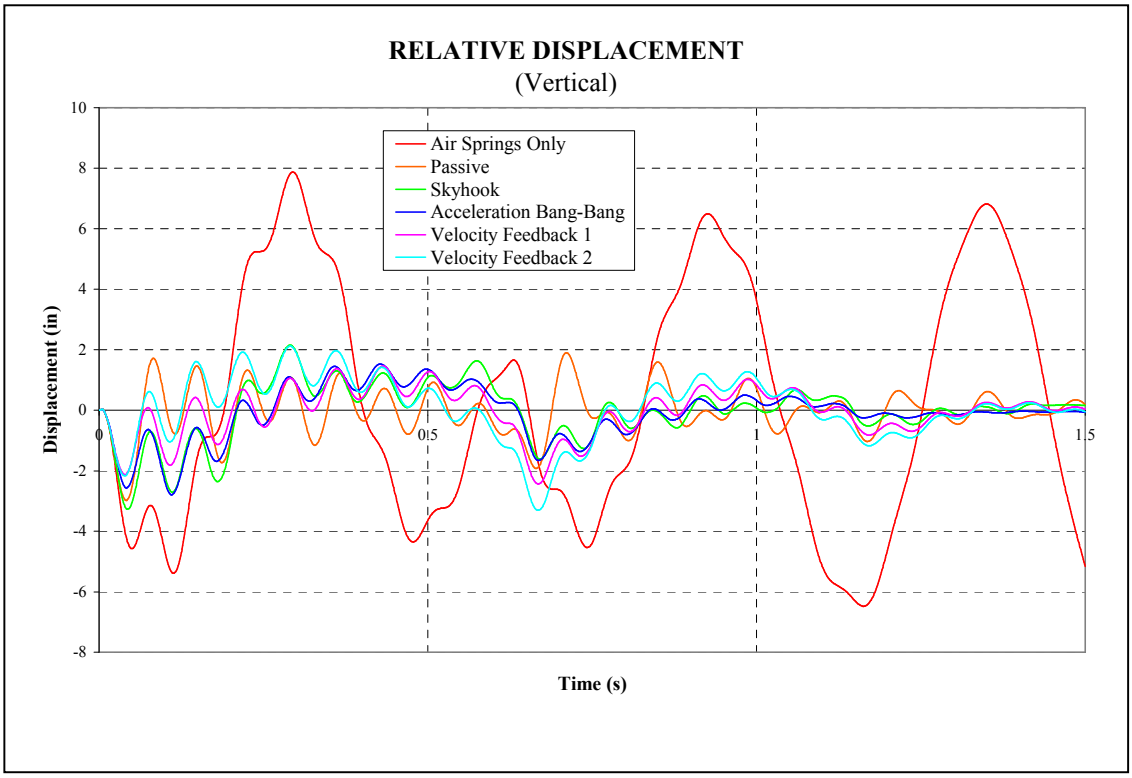


**Figure 7.5**: Vertical Response (Relative Displacement)

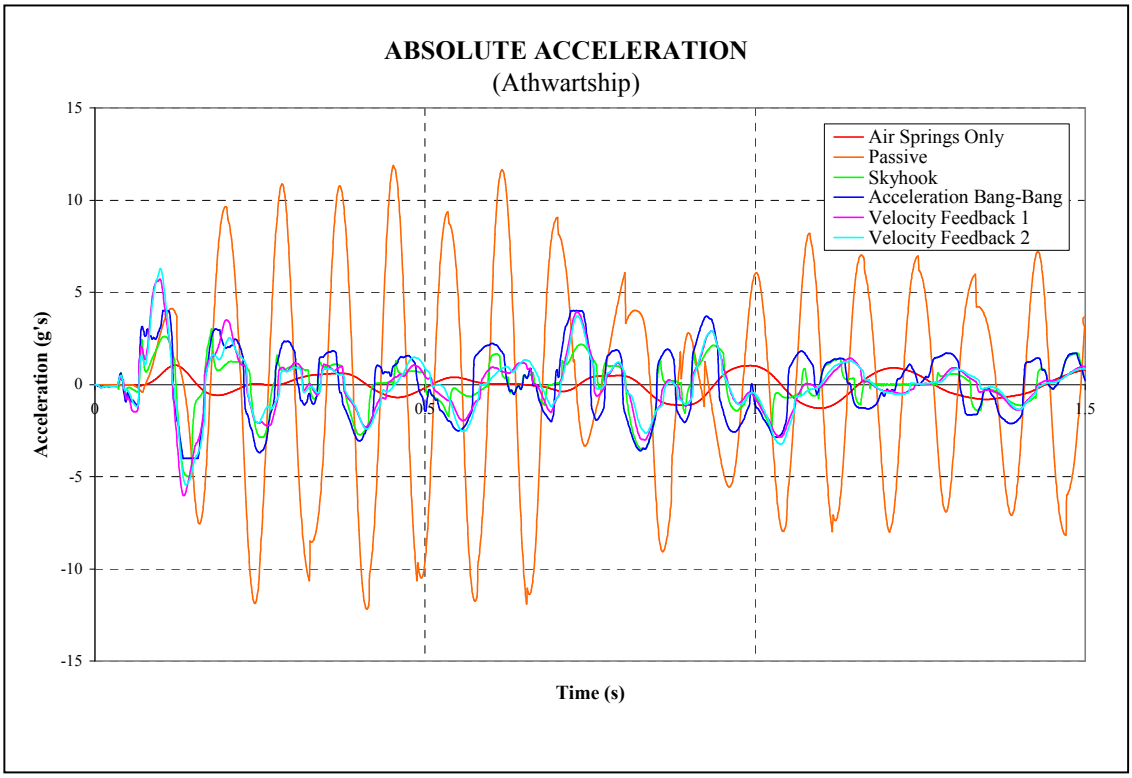


**Figure 7.6**: Athwartship Response (Absolute Acceleration)

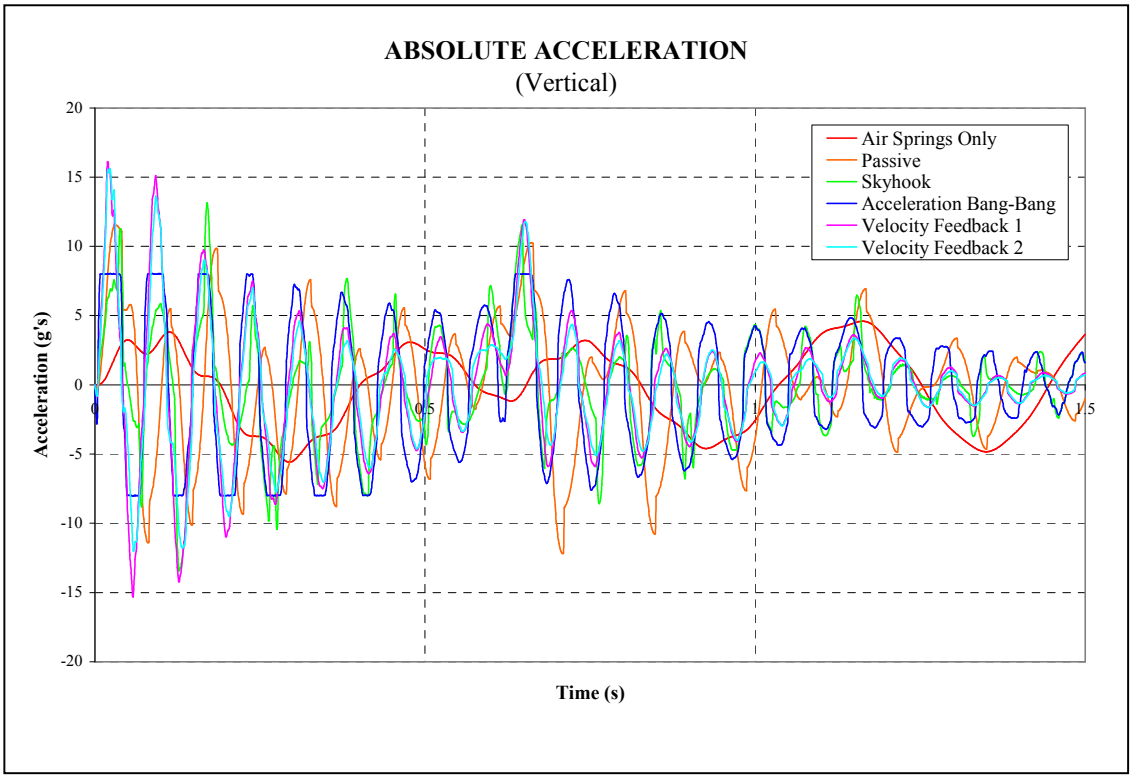


**Figure 7.7**: Vertical Response (Absolute Acceleration)

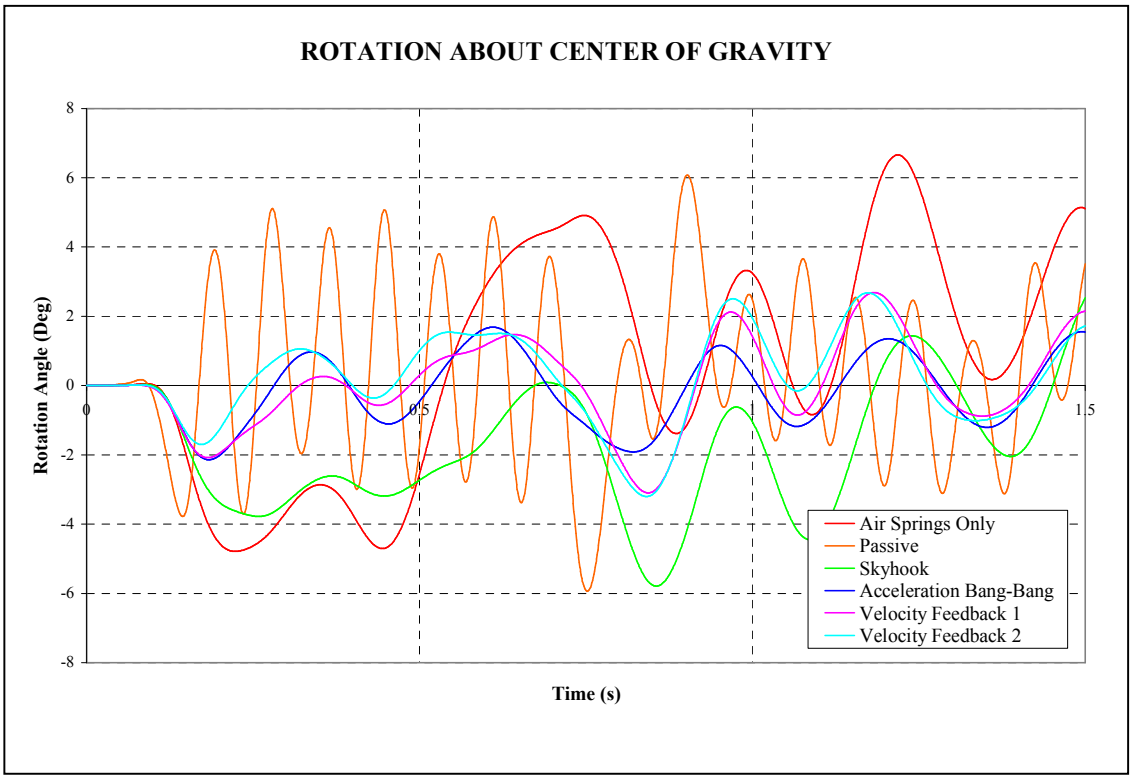


**Figure 7.8**: Rotational Response About the CG

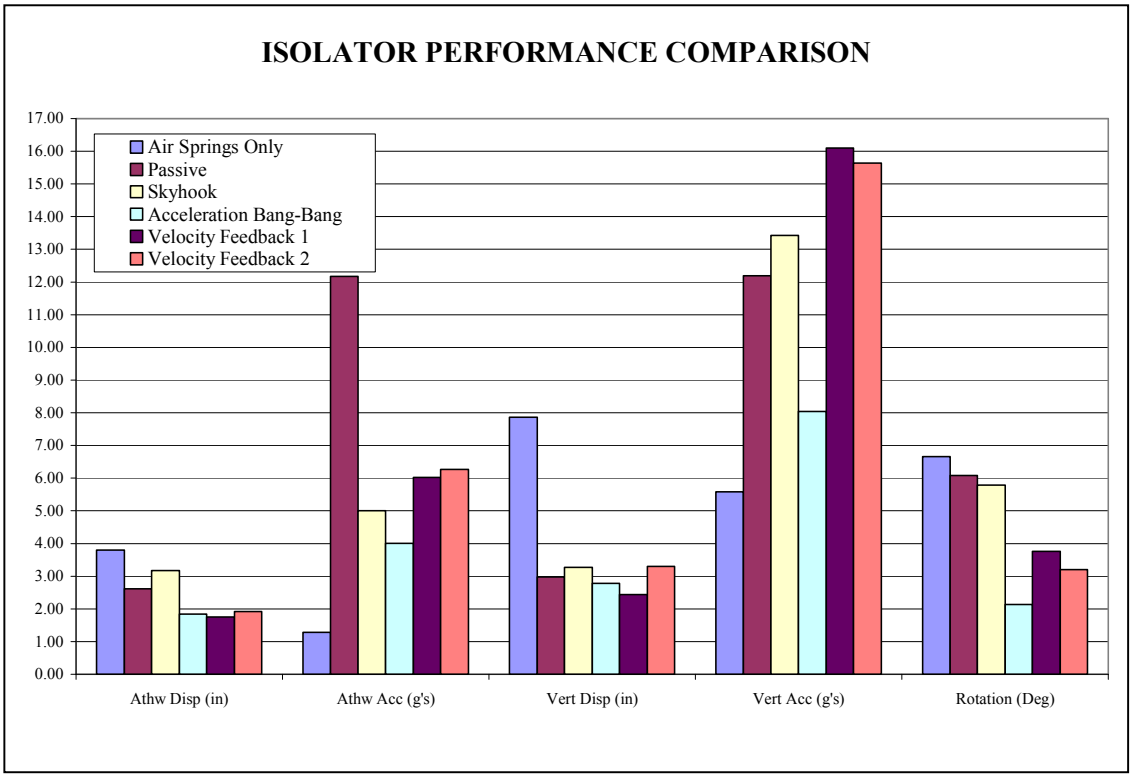


**Figure 7.9**: Response Peaks Comparison

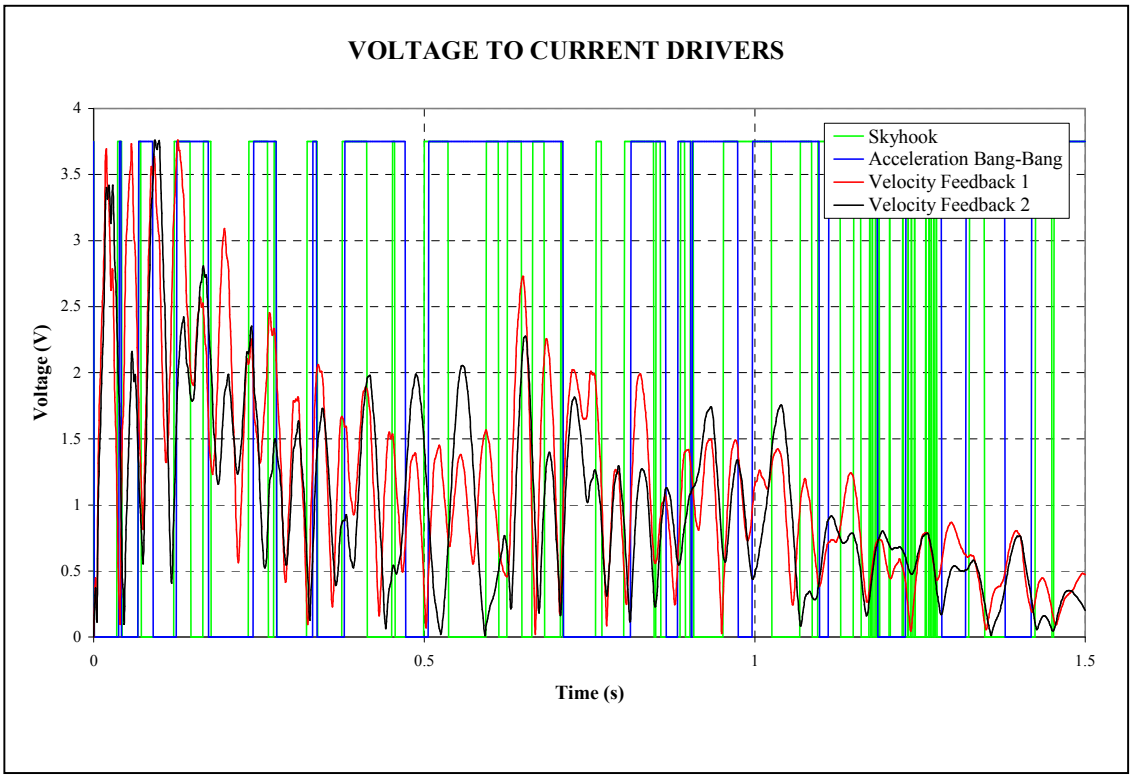


**Figure 7.10**: Voltage Output from Controllers

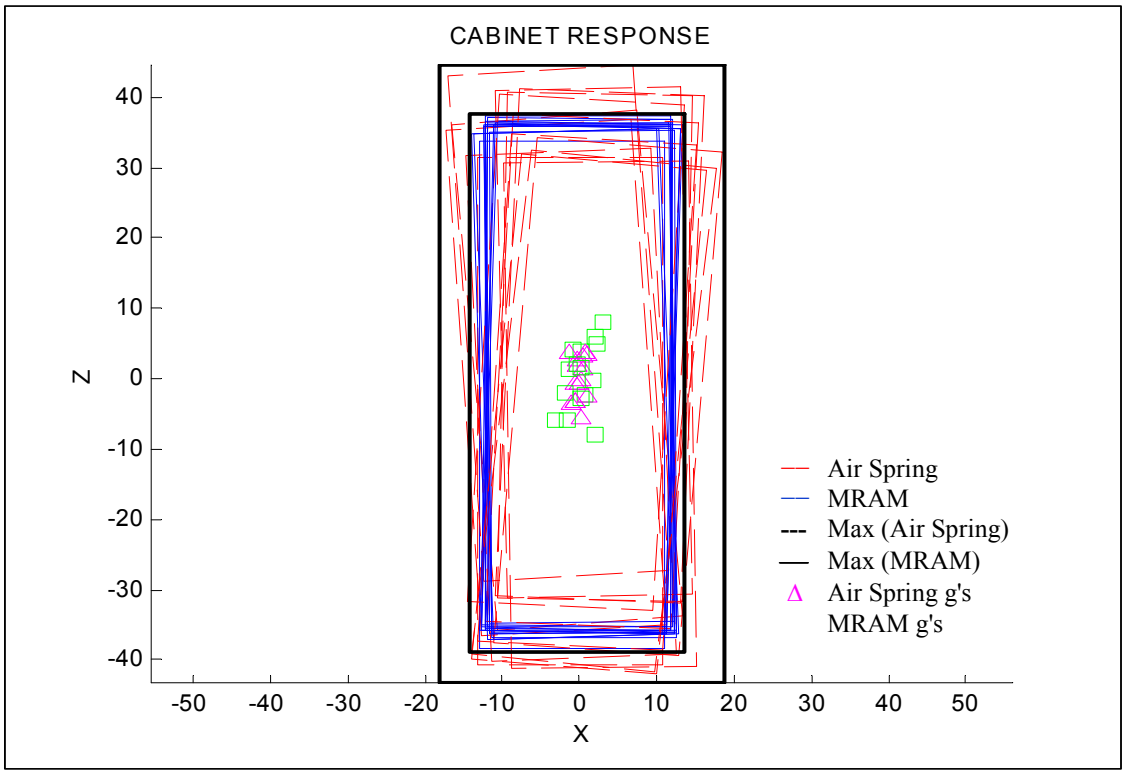


**Figure 7.11**: 3DOF Cabinet Response (Air Spring Only versus MRAM)

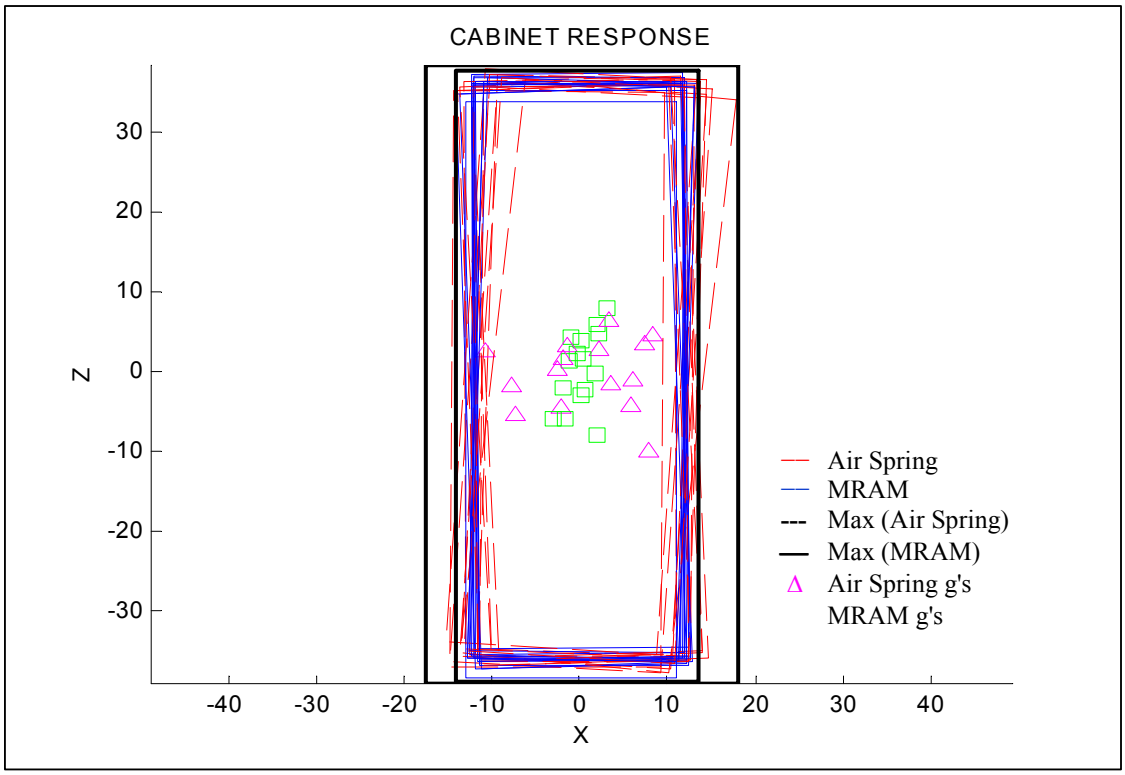


**Figure 7.12**: 3DOF Cabinet Response (Passive Mount versus MRAM)

From the figures it can be seen that the response of the cabinet mounted on air springs only is excellent in terms of above mount acceleration, but the response in terms of relative displacement is unacceptably large, particularly in the vertical direction. Furthermore, the resulting rotation of the cabinet on air springs only is too large to be acceptable for shipboard use. This result was expected as the air springs are essentially very low frequency springs which are very lightly damped.

The surprising result was the relatively poor performance of the standard passive mount when compared to the MRAM mounted cabinet. While the passive mount performed reasonably well in terms of limiting relative displacements, the above mount accelerations were considerably higher than those achieved with the controlled mounts. Also, the resulting cabinet rotations were nearly as large as with air springs only.

In terms of the controlled mounts, the performance of both of the Velocity Feedback controllers was disappointing. This is a good example that what might work well in a SDOF system will not necessarily work as well in a MDOF system. While the relative displacements and cabinet rotation was close to the lowest achieved with the controlled mounts, the above mount accelerations were high, particularly the vertical acceleration. While it is true that the feedback gain could be lowered to achieve a lower above mount acceleration, this would also result in increased relative displacements which would be unacceptable.

The performance of the Skyhook controller was also disappointing. The relative displacements exceeded 3 inches in both translation directions and the above mount vertical acceleration exceeded that of the passive mount. Furthermore, the cabinet rotation was nearly as high as the cabinet mounted with air springs only.

The standout of the controlled mounts was the system controlled with the Acceleration Bang-Bang controller. The surprising result of the simulations with this controller was that while the damping force is controlled based on acceleration inputs in both translation axes, there appears to be no performance detriment of switching the

dampers on and off based on both of these inputs simultaneously. In other words, there appears to be no problems in terms of performance by applying damping force in two directions simultaneously based on limiting above mount accelerations in both directions simultaneously. It was expected that there would have been problems with having the damper turned on based on an acceleration limit in one direction at a time when the damper should be off based on an acceleration limit in the other direction. It appears that the damper can switch on and off fast enough to eliminate these problems. Aside from the advantage of being able to preset the peak above mount accelerations, the resulting relative displacements are also very small. Furthermore, the cabinet rotations were the smallest of all of the controllers. In fact, the cabinet rotations were small enough that it would be possible to entirely base mount this tall, narrow cabinet. This would be very beneficial as adding sway mounts at the top of a cabinet, which is the typical solution for reducing cabinet rotations, presents problems with installation in many cases.

## 7.4 Chapter Summary

The subject isolation system appears to solve many problems associated with isolating shipboard equipment. The performance of the system was verified using a previously validated model of the mount and the simulation results suggest that the Acceleration Bang-Bang controlled mount offers excellent performance with ship shock inputs. An additional advantage to this controller is the ability to "dial in" an above mount acceleration level while simultaneously producing the absolute lowest mount deflections for the selected acceleration level. An additional benefit is that this mount could be used to entirely base mount tall, narrow cabinets. The elimination of sway mounts would make installation of shipboard equipment much easier.

It should be noted that all of these tests and simulations utilized a commercial, off-the-shelf damper that was designed for seat isolation on large Class 8 trucks. A more optimally designed damper for shipboard isolation applications could achieve considerable improvements in performance. It is entirely feasible that 5 g above mount

accelerations could be easily achieved using this technology. The 5 g goal has been mentioned as the ultimate target for shipboard isolation systems. It is anticipated that if a 5 g peak acceleration could be achieved it may be possible in the future to eliminate, or at least minimize, costly shock testing of equipment. As such, this should be a goal of any advanced isolation system for shipboard use.

# Chapter 8

# Power Scavenging System Development

## 8.1 Introduction

Scavenging environmental energy to use for powering various devices has long been a scientific curiosity. Many types of energy have been harvested with varying degrees of success. This experiment was conducted to determine whether ambient shipboard vibration energy could be harvested and stored to power the MR/Air mount or other shipboard devices. Two types of devices were initially considered. The first was a Moving Magnet Linear Generator, essentially a magnet-spring-coil arrangement. The second was a Piezoelectric Stack Generator. Each of these devices will be discussed in detail below.

## 8.2 The Moving Magnet Linear Generator

The Moving Magnet Linear Generator (MMLG) is shown in Figure 8.1. The generator is analogous to a permanent magnet loudspeaker driven in reverse. The device operates through Faraday's Law of Induction. A moving magnet connected to a vibrating structure through a spring(s) would be excited by the vibration of the structure to which it is attached. The base excitation would induce a vibration in the spring-mass(magnet) system. The relative motion of the magnet to the surrounding coil would induce an AC voltage in the coil. By carefully selecting the mass of the magnet and/or the stiffness of the spring(s) the device could be tuned to operate in resonance. Operating in resonance would maximize the energy output of the device.

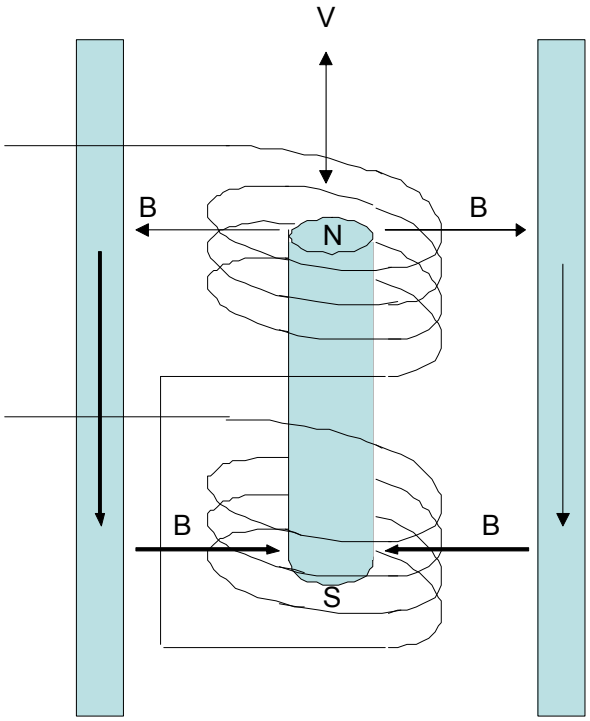


**Figure 8.1**: Moving Magnet Linear Generator

The voltage induced by a MMLG is,

$$\varepsilon = NBL\dot{x} \text{ (V)} \tag{8.1}$$

where,

$N$ = Number of Turns in Coil
$B$ = Magnetic Field Strength (Tesla)
$L$ = Length of Coil (m)
$\dot{x}$ = Relative Velocity of Magnet to Coil (m/s)

The force $F$ in Newtons required to move the magnet relative to coil is,

$$F = NiLB \tag{8.2}$$

where $i$ is the current generated in Amps. Therefore, the current generated by the device is,

$$i = \frac{\varepsilon}{R} = \frac{NBL}{R}\dot{x} \tag{8.3}$$

where $R$ is the coil resistance in Ohms. It follows that the coil/magnet damping force is,

$$F = NLB\left(\frac{NLB}{R}\right)\dot{x} = \frac{(NLB)^2}{R}\dot{x} = c\dot{x} \tag{8.4}$$

Therefore, the damping coefficient $c$ in kg/s of the coil/magnet damping force is:

$$c = \frac{(NLB)^2}{R} \tag{8.5}$$

and it follows that the damping ratio of the effective coil/magnet damping force is,

$$\zeta = \frac{c}{2m\omega} = \frac{(NLB)^2}{2m\omega R} \tag{8.6}$$

For a damped spring-mass system subject to a base excitation equal to the system natural frequency, the transmissibility ratio in terms of displacement is,

$$T.R. = \frac{X}{Y} = \left[\frac{1+4\zeta^2}{4\zeta^2}\right]^{1/2} \Rightarrow X_{rel} = \underbrace{\left[\frac{1+4\zeta^2}{4\zeta^2}\right]^{1/2}}_{X} - Y = \left\{\left[\frac{1+4\zeta^2}{4\zeta^2}\right]^{1/2} - 1\right\}Y \tag{8.7}$$

where,

$X$ = Amplitude of Response
$Y$ = Amplitude of Base Input

Therefore, to maximize the response displacement, and hence the response velocity, it is desirable to minimize the damping ratio (within reason). Looking at Equation (8.6) this can be done by increasing the coil resistance (or adding resistance) to the circuit. However, by Equation (8.3) increasing the resistance decreases the output current. Since current is the quantity that needs to be maximized this requires $R$ to be as small as practicable. However, decreasing $R$ until a reasonable current can be produced leads to a large damping ratio which by Equation (8.7) decreases magnet-to-coil relative velocity. From Equation (8.1) it is clear that decreasing the magnet-to-coil velocity decreases the amplitude of the output voltage. Taking all of these parameters into consideration simultaneously leads to significant difficulty in designing an adequate generator of this type. While it may be possible to design a MMLG that can produce an acceptable level of current at the required 12 - 14 Volts by optimizing the design parameters that can be varied, it turns out that this would be a very difficult optimization problem. Investigation of other potential scavenging devices suggest that a more efficient generator for scavenging ambient shipboard vibration energy can be designed using the technology discussed in the next section. Given this and the difficulty of optimizing the parameters of the MMLG to produce a viable power scavenging device, the MMLG was dropped as a potential solution.

## 8.3 The Piezoelectric Stack Generator

A device more ideally suited to scavenge the minute amplitude vibrations found in shipboard applications is the Piezoelectric Stack Generator (PSG). To understand why this device is more ideally suited to this application requires insight into the transfer of power between the input (source) and the generator (load). Analogous to the result found in electrical circuit theory, the maximum power is transferred from the source to the load when the magnitudes of the source and load mechanical impedances are equal. For this application the source is a small displacement, low frequency, large amplitude force. Thus the source impedance is relatively large. The impedance of the PSG is also large

making the PSG a better impedance match to the available source with the result being a more efficient power transfer.

A piezoceramic is a material that when stressed electrically by a voltage $V_{in}$ changes its dimensions. If the piezoceramic is constrained when the voltage is applied then a force $F_{out}$ is exerted by the material as shown in Figure 8.2.

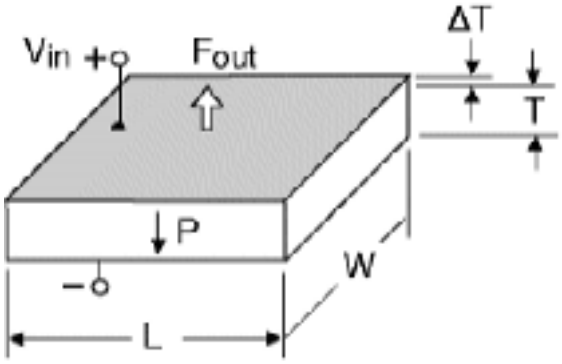


**Figure 8.2**: Behavior of Piezoceramic with Applied Voltage

Furthermore, when a piezoceramic is stressed mechanically by a force $F_{in}$ it generates an electric charge as shown in Figure 8.3.

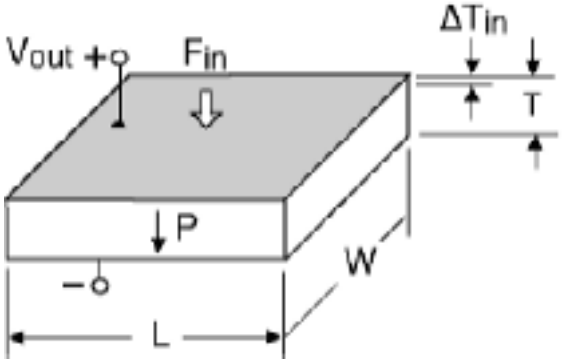


**Figure 8.3**: Behavior of Piezoceramic with Applied Force

If electrodes are placed on the appropriate opposing faces of the piezoceramic crystal, and the electrodes are not short-circuited, a voltage $V_{out}$ associated with the charge appears. This property is termed the piezoelectric effect and these materials are commonly referred to as piezoelectric materials. Thus, a piezoelectric is capable of acting as either an actuator, or a generator, or both.

A single layer of piezoelectric material can produce several hundred Volts for a reasonably small force input, but the charge produced is very small. Since current $i$ is the time derivative of the charge $Q$,

$$i = \frac{dQ}{dt} \tag{8.8}$$

a small charge equates to a small current from the piezoelectric generator. At this point it would be useful to look at the mathematical relationships that govern a piezogenerator.

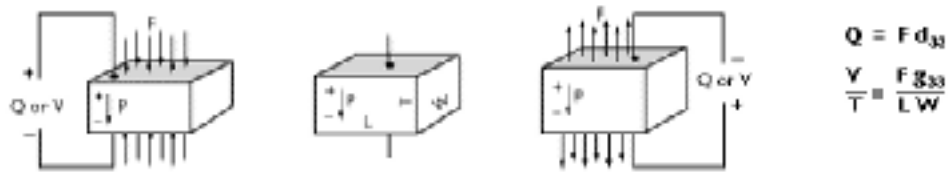


**Figure 8.4**: Piezogenerator Relationships

From Figure 8.4 it can be seen that charge $Q$ is directly proportional to the applied force $F$, or

$$Q = d_{33}F \tag{8.9}$$

The constant of proportionality $d_{33}$ is known as the piezoelectric strain constant and the 33 subscript implies that the constant is associated with a force applied in line with the

axis of polarization. This is the most efficient orientation in terms of charge generation and hence this is the orientation that will be utilized in this experiment.

The voltage produced by a piezogenerator can be derived as follows:

The stress in a piezoelectric crystal due to an applied force is,

$$\sigma = \frac{F}{A} \tag{8.10}$$

where $F$ is the applied force and $A$ is the cross-sectional area of the crystal. There are two governing equations for piezoelectrics. The first describes the strain produced in the material by an applied electric field and the second describes the electric field produced by a stress on the material. The later is the equation that is needed for this application and the mathematical relationship is,

$$\xi = g_{33}\sigma \tag{8.11}$$

where $\xi$ is the field produced by the stress $\sigma$. $g_{33}$ is a constant related to $d_{33}$ by the relation,

$$E = \frac{1}{g_{33}d_{33}} \tag{8.12}$$

therefore,

$$\xi = g_{33}\frac{F}{A} \tag{8.13}$$

Now, the voltage produced by the strained piezoelectric is,

$$V = \xi T \tag{8.14}$$

where $T$ is the thickness of the material, therefore, the voltage produced in the piezoelectric by an applied force $F$ is,

$$V = \frac{FTg_{33}}{A} = \frac{FTg_{33}}{LW} \Rightarrow \frac{V}{T} = \frac{Fg_{33}}{LW} \tag{8.15}$$

which is equivalent to the equation shown in Figure 8.4. Analysis shows that the resulting force in a PSG due to small amplitude ambient shipboard vibrations tend to be small as well. By looking at Equation (8.15) this implies that the voltages produced by a piezoelectric material subjected to these forces will be small as well. This is acceptable as only as small voltage (12 Volts) is needed to power the dampers and associated electronics. Since piezoelectric materials are capable of producing hundred of Volts, producing 12 Volts is not a problem. The real problem with piezoelectric devices is the amount of current that can be produced. From Equations (8.8) and (8.9) the current produced by a piezoelectric due to an applied force is,

$$i = \frac{dQ}{dt} = d_{33}\frac{dF}{dt} \tag{8.16}$$

but, the force in the material is,

$$F = kx \tag{8.17}$$

where $k$ is the stiffness of the material and $x$ is the deflection of the material. Substituting Equation (8.17) into Equation (8.16) gives,

$$i = d_{33}k\dot{x} \tag{8.18}$$

where $\dot{x}$ is the time derivative of the deflection of the material, or the velocity across the material due to the applied force. Thus, the current produced is a function of the stiffness of the material and the velocity with which the material is deflected. Unfortunately, the velocity cannot be varied as it is a function of the available ambient mechanical vibration.

One method to increase the current is to stack up multiple layers of piezoceramic material as shown in Figure 8.5.

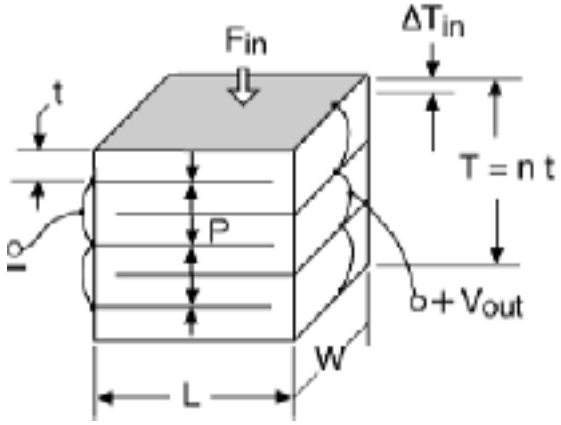


**Figure 8.5**: Piezoelectric Stack Generator

Assuming each layer is the same thickness, for a given force the layers will produce essentially identical currents. If the layers are connected in parallel, these currents can then be summed to increase the total current output of the device. Of course increasing the thickness, and adding insulating material between the layers, decreases the stiffness which may lower the current output slightly, but the increased current obtained by summing the currents produced by each layer far outweighs the effect of this decreased stiffness.

Another method is to place multiple layers of piezoceramic material physically in parallel between the excitation source and supported mass. This increases the stiffness, but simultaneously lowers the force acting on each layer. Furthermore, this reduces the deflection and hence the velocity of deflection of the piezoelectric material. While this

may be a viable arrangement it was decided that a series-stacked arrangement as shown in Figure 8.5 would be used for this experiment.

## 8.4 The Storage of Scavenged Energy

It was decided that storage of the energy scavenged by the PSG would be stored until needed in a bank of ultracapacitors. This is certainly not the only device capable of storing the scavenged energy, but the ultracapacitor was attractive as it is compact and requires minimal maintenance. An ultracapacitor is a chemical capacitor that is capable of storing tremendous amounts of energy. This is accomplished by optimizing the geometrical factors that enter into the capacitance equation for a parallel-plate capacitor. Ignoring fringing of the electric field at the edges of the plates, the capacitance $C$ of a parallel-plate capacitor in Farads can be described by,

$$C = \varepsilon \frac{A}{d} \tag{8.19}$$

where,

$\varepsilon$ is a constant (The permittivity constant)
$A$ is the plate area
$d$ is the distance between the plates

Chemical capacitors can greatly increase the capacitance by decreasing the area between the plates to the atomic level and/or simultaneously increasing the effective plate area by using porous surfaces. Ultracapacitors of 2700 Farads are currently available commercially. One problem with current ultracapacitors is their relatively low operating voltages which is typically no greater than 2.5 Volts. However, considering the energy $E$ in W·s that can be stored in a capacitor is described by,

$$E = \frac{1}{2} C V^2 \tag{8.20}$$

where,

$C$ is the capacitance
$V$ is the voltage (in Volts)

Therefore at 2.5 Volts a 2700 Farad capacitor could store,

$$E = \frac{1}{2}(2700)(2.5)^2 \approx 8400 \text{ Watt·s} = 8.4 \text{ kW·s} \tag{8.21}$$

Thus, this capacitor could produce 8.4 kW of energy for 1 second. This is a tremendous amount of stored energy for a device that is small enough to fit in one hand. Clearly these devices are ideal for storing large amounts of energy.

At peak load an individual MR dampers draws 2 Amps at 12 Volts. For this experiment it was desired to store enough energy to power four dampers through a typical 2 second shock event. The power required to operate four dampers for 2 seconds is,

$$P = 4(12V \cdot 2A) = 96W \tag{8.22}$$

and the required energy is,

$$E = 96W \cdot 2s = 192W \cdot s = 192J \tag{8.23}$$

The energy stored in a capacitor is,

$$E = \frac{1}{2} C V^2 \tag{8.24}$$

Equating Equation (8.23) and (8.24),

$$\frac{1}{2}CV^2 = 192 \Rightarrow C = \frac{2(192)}{12^2} = 2.67F \tag{8.25}$$

Therefore, a 2.67 Farad, 12 Volt capacitor is needed as a minimum. The ultracapacitors that were used in the experiment were supplied by Maxwell Technologies®. Since all of their ultracapacitors are rated for 2.5 Volts it was necessary to use five capacitors in series to achieve the necessary voltage. The capacitance of $n$ series connected capacitors is,

$$C_{eq} = \frac{1}{\sum_n \frac{1}{C_n}} \tag{8.26}$$

and if the capacitors have equal capacitance the series capacitance is,

$$C_{eq} = \frac{1}{\underbrace{\frac{1}{C} + \cdots + \frac{1}{C}}_{n}} = \frac{1}{\frac{n}{C}} = \frac{C}{n} \tag{8.27}$$

Thus, for the five capacitors needed $C_{eq} = C/5$. Maxwell® manufactures ultracapacitors in 5, 10, 100, 1000, 2500 and 2700 Farads. Since five capacitors are needed to satisfy the voltage requirement, and 2.67 Farads are required for combined capacitor stack, the minimum capacitance that will satisfy all of these requirements simultaneously is the 100 Farad ultracapacitor. Five of these in series gives a 5(2.5V) = 12.5V voltage capability and the total capacitance is 100/5 = 20 Farads. Thus, the energy that can be stored in the combined ultracapacitor stack is,

$$E = \frac{1}{2}CV^2 = \frac{1}{2}(20)(12)^2 = 1440\,J > 192\,J \tag{8.28}$$

which is considerably greater than the 192 J necessary to power the four MR dampers for 2 seconds.

## 8.5 Analysis of the Ultracapacitor Stack

To test the charge/discharge behavior as well as the storage capacity of the ultracapacitor stack, the capacitors were charged slowly using a 28 volt peak-to-peak rectified sinusoidal current at 33 Hz. The input was generated by a current source and isolated using a transformer. The PSG was included in the charging circuit to more accurately represent the true capacitance of the charging circuit. The measured capacitance of the PSG was 0.2 microfarads. A schematic of the charging circuit is shown in Figure 8.6 and a photograph of the charging circuit is shown in Figure 8.7.

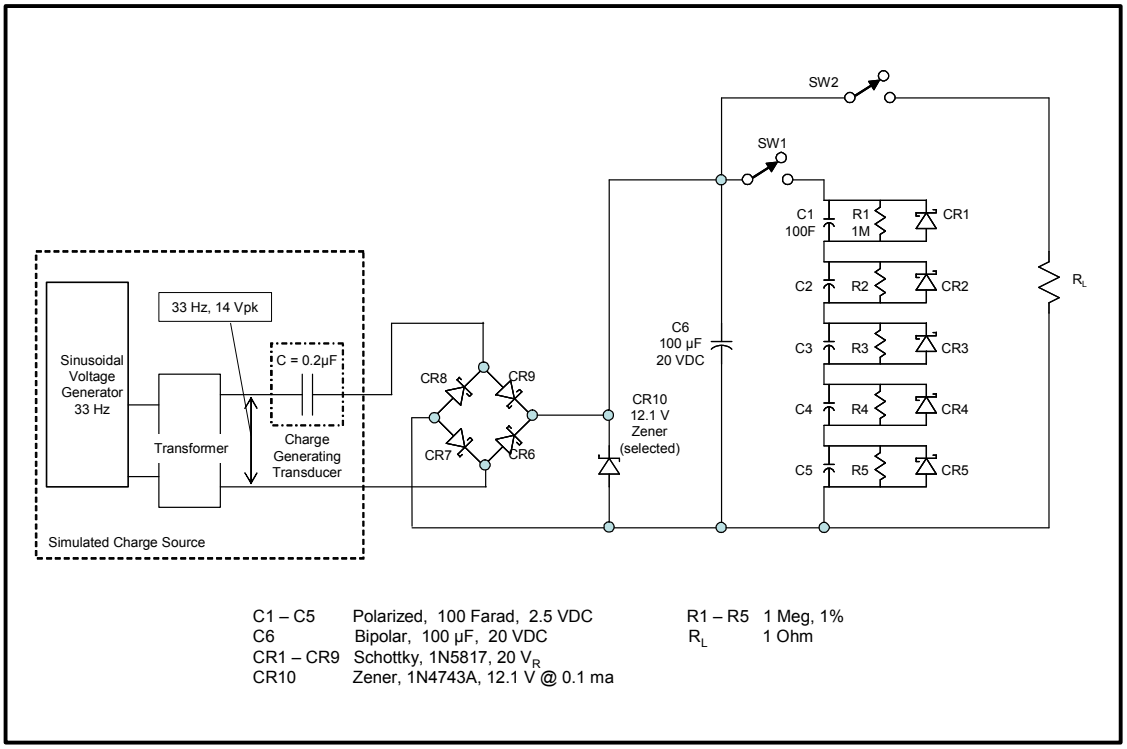


**Figure 8.6**: Schematic of Charging Circuit

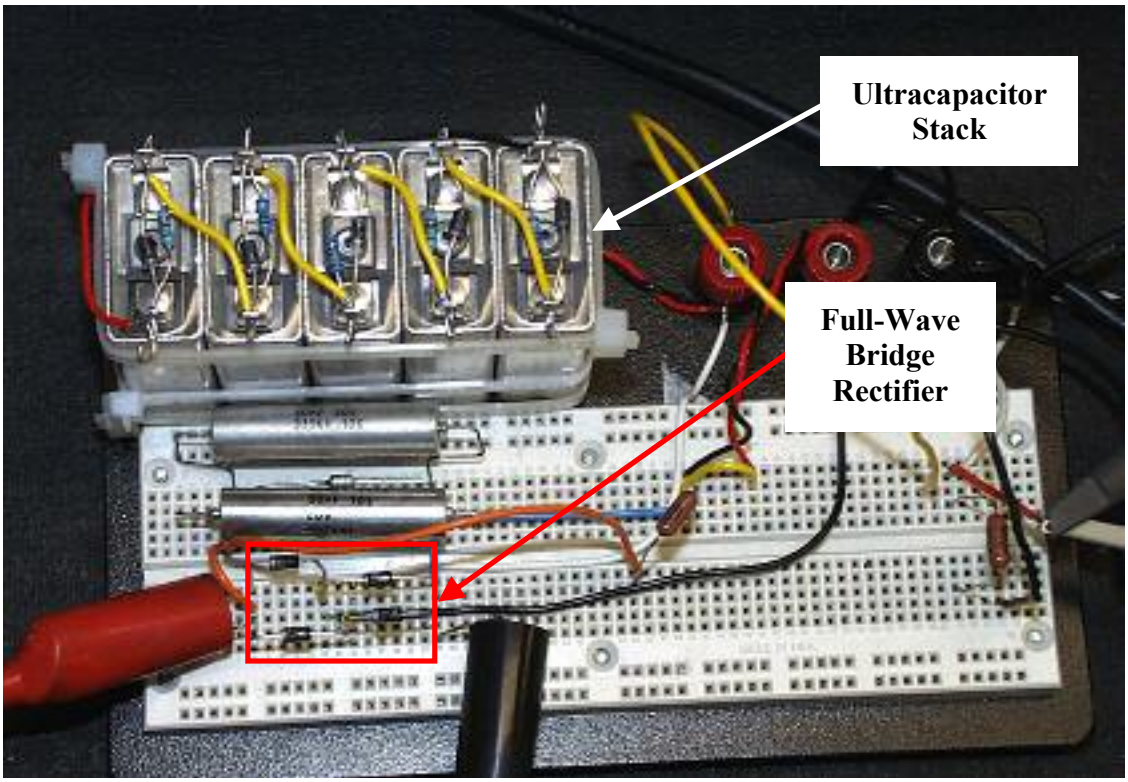


**Figure 8.7**: Ultracapacitor Charging Circuit

Using the charging source described above the ultracapacitor stack was charged very slowly for 440 hours (≈ 18 days). Figure 8.8 shows the charging curve (Voltage versus time) for the ultracapacitor stack. After 440 hours the stack reached a final voltage of 10.6 Volts. Also plotted in the figure is an analytical exponential fit to the data. Note that the analytical exponential fits the data very well until about 170 hours of charge time. After 170 hours the charge curve deviates from the analytical exponential. This shows that the ultracapacitor stack behaves very nearly like an ideal capacitor paralleled by a constant "leakage" resistance until approximately 170 hours. After that time the voltage increases with time at a higher rate than would be predicted by the ideal capacitor model. This is due to changes in the chemical properties of the capacitor which occur after the capacitor has remained charged for an extended period of time.

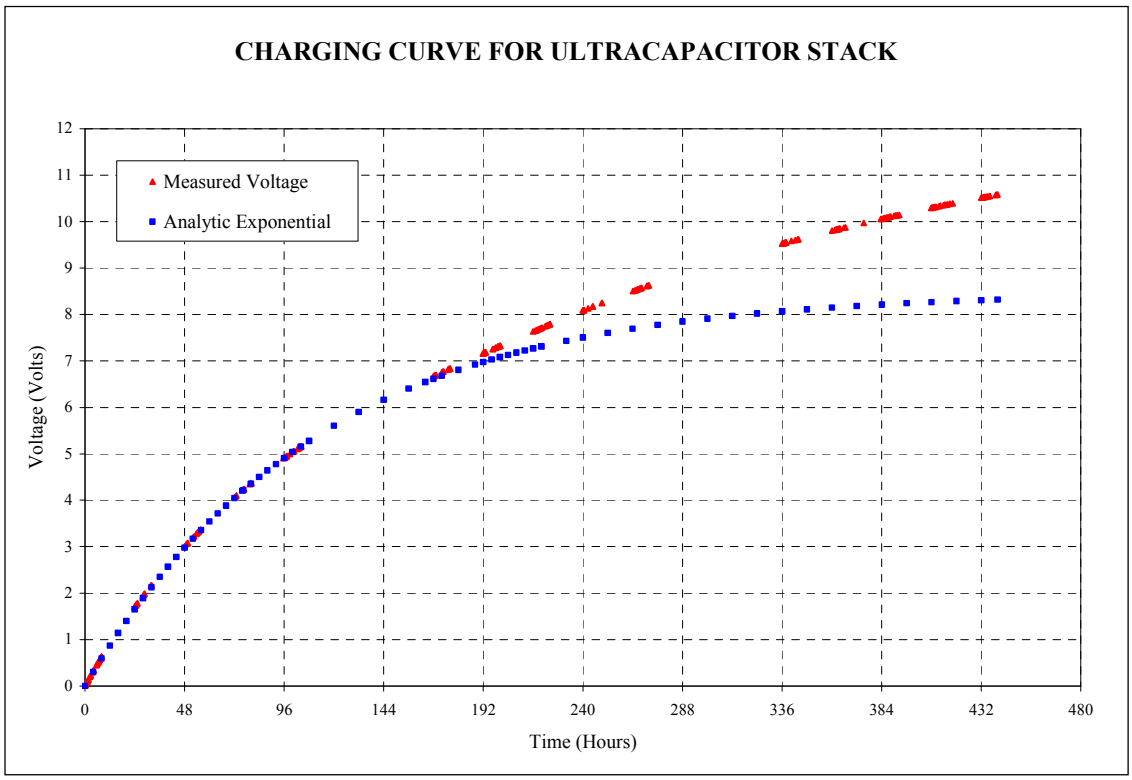


**Figure 8.8**: Charging Curve for the Ultracapacitor Stack

Immediately following the charging test the ultracapacitor stack was discharged through a 1 ohm power resistor. This was done to quantify the amount of energy stored in the ultracapacitor stack as well as the power that could be delivered by the charged stack. No attempt was made to quantify the resistance of the cables in the discharge circuit. Figure 8.9 shows the discharging curve (Current versus time) for the ultracapacitor stack. Since the capacitors were discharged through a 1 Ohm resistor (neglecting the cable resistance) this plot also represents the voltage time history of the ultracapacitor stack during discharge. Also plotted in the figure is an analytical exponential fit to the data. The fact that the analytical exponential fits the data very well suggests that the ultracapacitor stack behaves very nearly like an ideal capacitor during discharge. Furthermore, the detail in the figure shows that the ultracapacitor stack is capable of providing 8 Amps of current for over three seconds. However, the voltage was not quite as high as the 12 Volts desired. Note that this is greater than the design goal of 8 Amps for two seconds thereby validating the storage capability of the ultracapacitor for this application.

Note that this assumes the capacitor stack is only discharged until it reaches 8 Volts. In actuality much more energy is left unused in the stack by taking this approach. Figure 8.10 shows the voltage in the ultracapacitor stack as a function of several constant discharge powers. Note that a constant 100 Watts of power can be drawn from the stack for 10 seconds if the voltage from the stack starts from 10 Volts and is allowed to go to zero.

Considerably more energy can be utilized from the stack if a DC-DC converter is used to maintain the desired output voltage. Connecting a DC-DC converter to the ultracapacitor stack would provide a constant output voltage from the stack until the voltage in the stack reaches some floor level. This floor level is dependent on the design of the DC-DC converter. This allows much more of the stored energy to be used, but the trade-off would be longer recharge times. However, by more efficiently using the available energy, smaller capacitors could be used which could decrease the recharge time considerably.

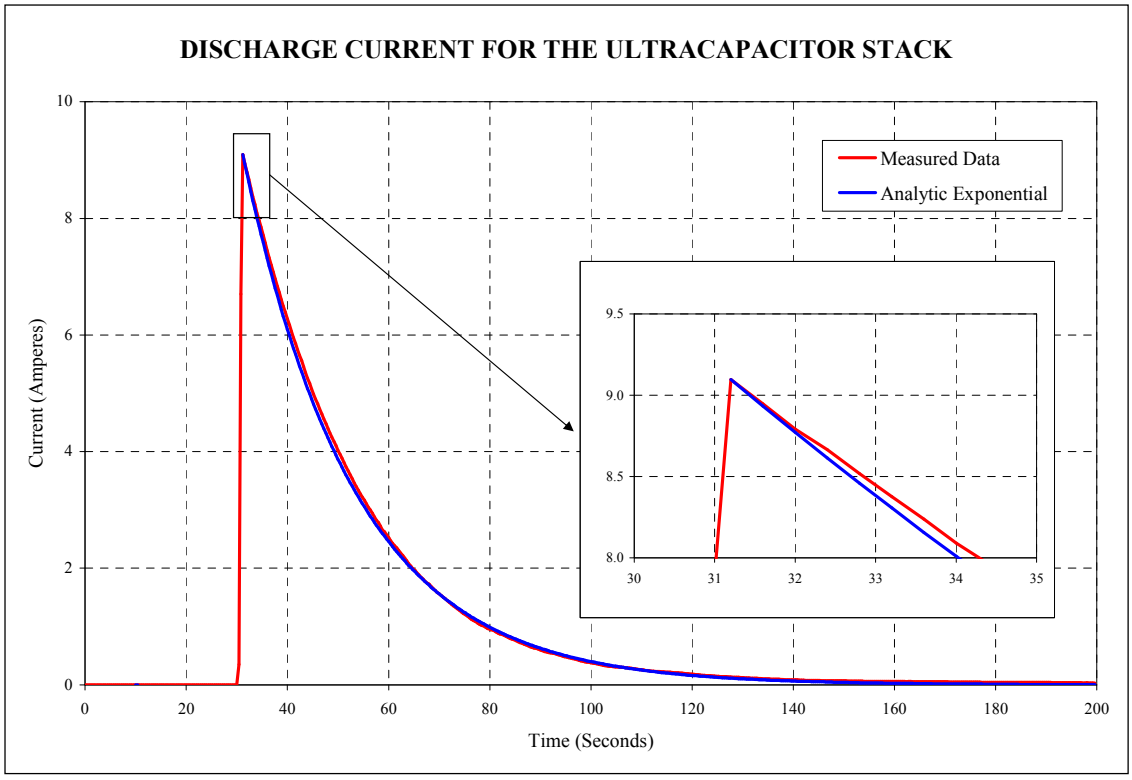


**Figure 8.9**: Discharging Curve for the Ultracapacitor Stack

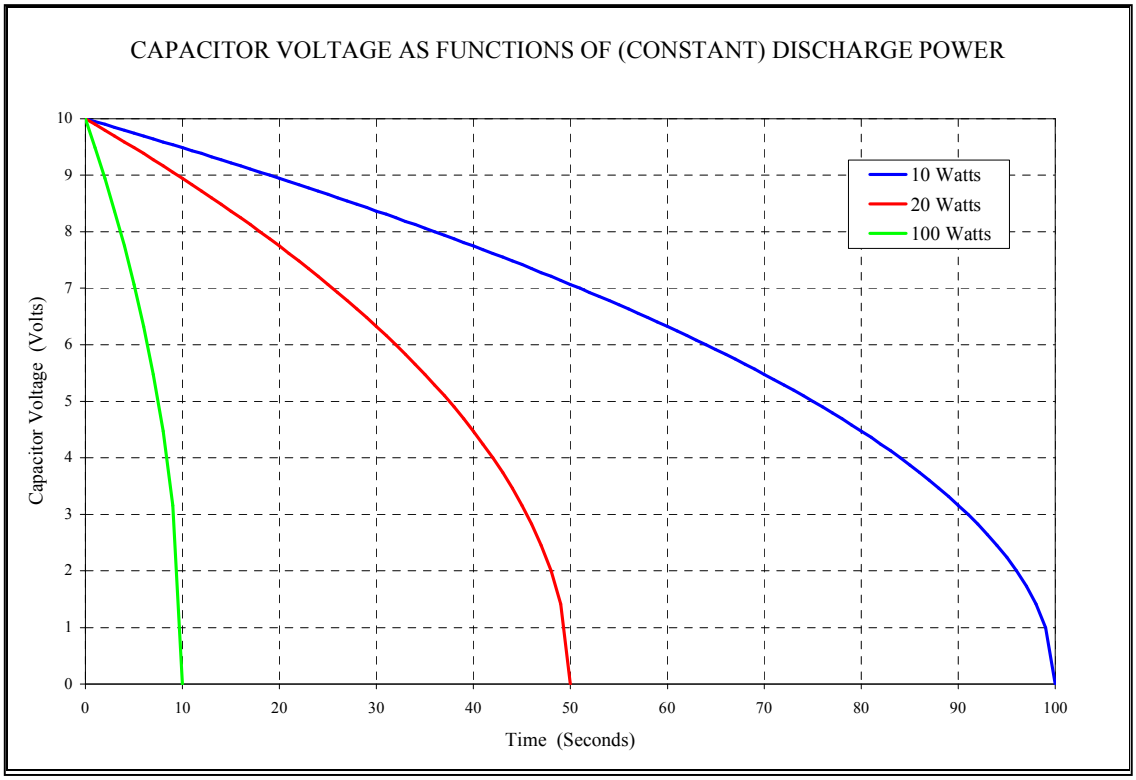


**Figure 8.10**: Capacitor Voltage as a Function of Constant Discharge Power

## 8.6 Empirical Analysis of the Piezoelectric Stack Generator

To evaluate the performance of the PSG (Shown in Figure 8.11) the generator was fixtured in an MTS 810 Material Test System as shown in Figure 8.12. Due to the large (50,000 lbf) capacity of the MTS machine it was decided that the machine would be controlled on displacement as opposed to force. This was necessary as the 50,000 lbf load cell used for force control of the machine is not ideally suited to the low forces required for this test. A relatively compliant spring was placed in series with the load cell to further reduce the applied loads. The actual load applied to the load cell was measured with a 200 lbf load cell which was placed just below the PSG. The MTS machine was programmed to apply a sinusoidally varying axial dynamic force to the PSG over a 100 lbf static preload. The frequency and/or dynamic force amplitude could be varied through the machine's control interface.

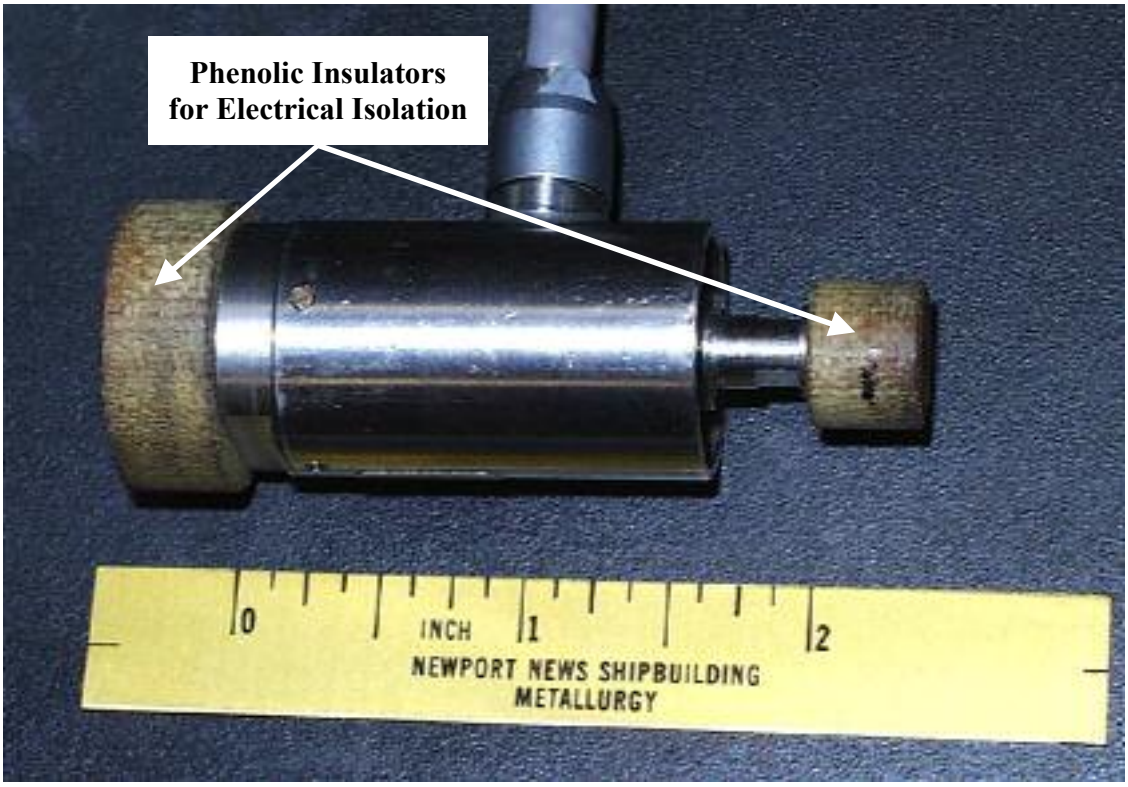


**Figure 8.11**: Kinetic Ceramics Prototype Piezoelectric Stack Generator

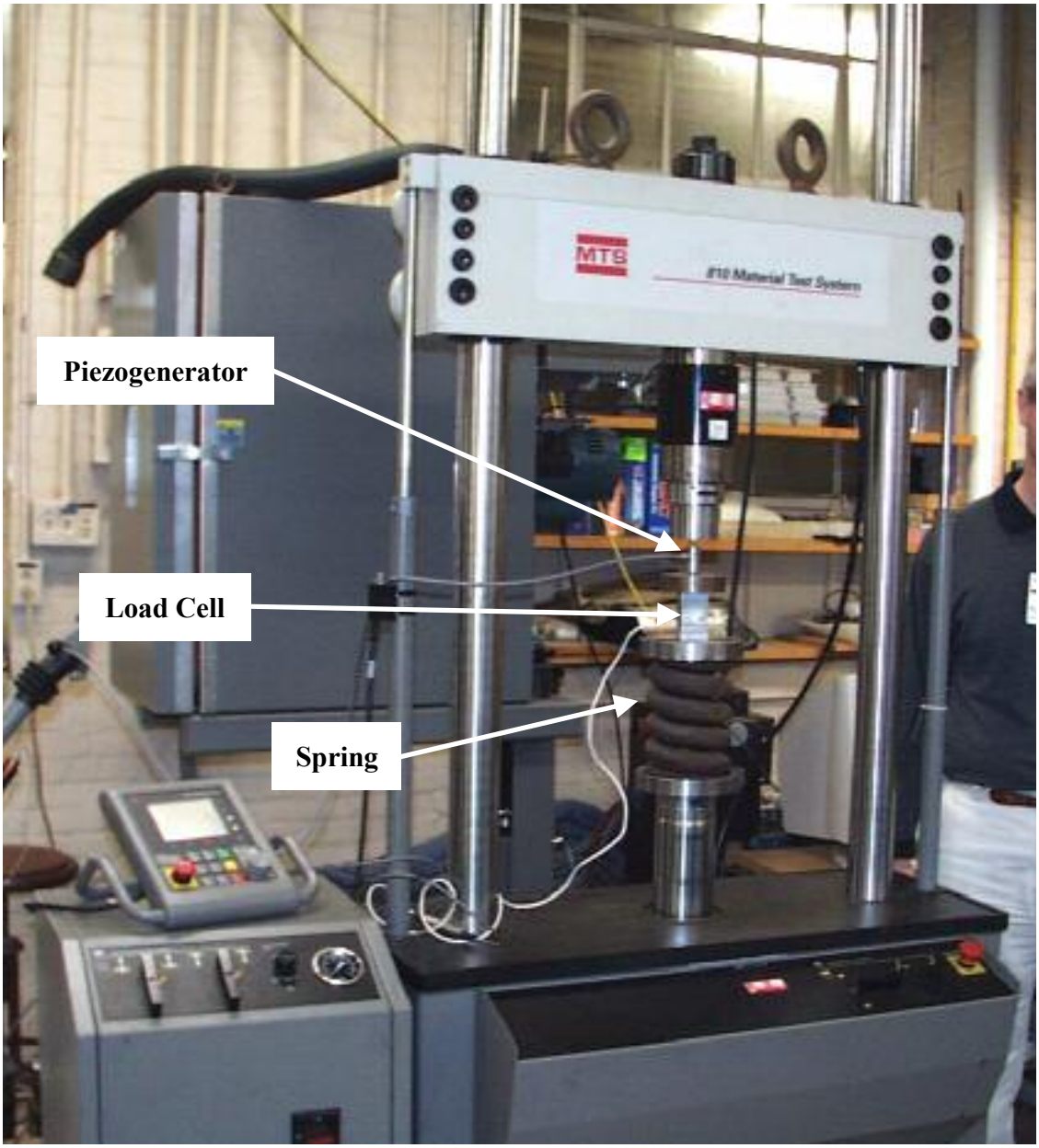


**Figure 8.12**: Piezoelectric Stack Generator in the MTS Load Frame

The data was measured by adjusting the displacement amplitude until the force amplitude measured with the 200 lbf load cell was equivalent to the desired force at the fundamental frequency. This was determined by examining the force amplitude at the fundamental using a spectrum analyzer. When the desired frequency and force amplitude was obtained the AC voltages were measured using a digital oscilloscope and the rectified DC voltages were measured using a digital multimeter. The data acquisition

equipment is shown in Figure 8.13 and a schematic of the data acquisition system is shown in Figure 8.14. Figure 8.15 shows a schematic of the charging circuit used in the PSG test.

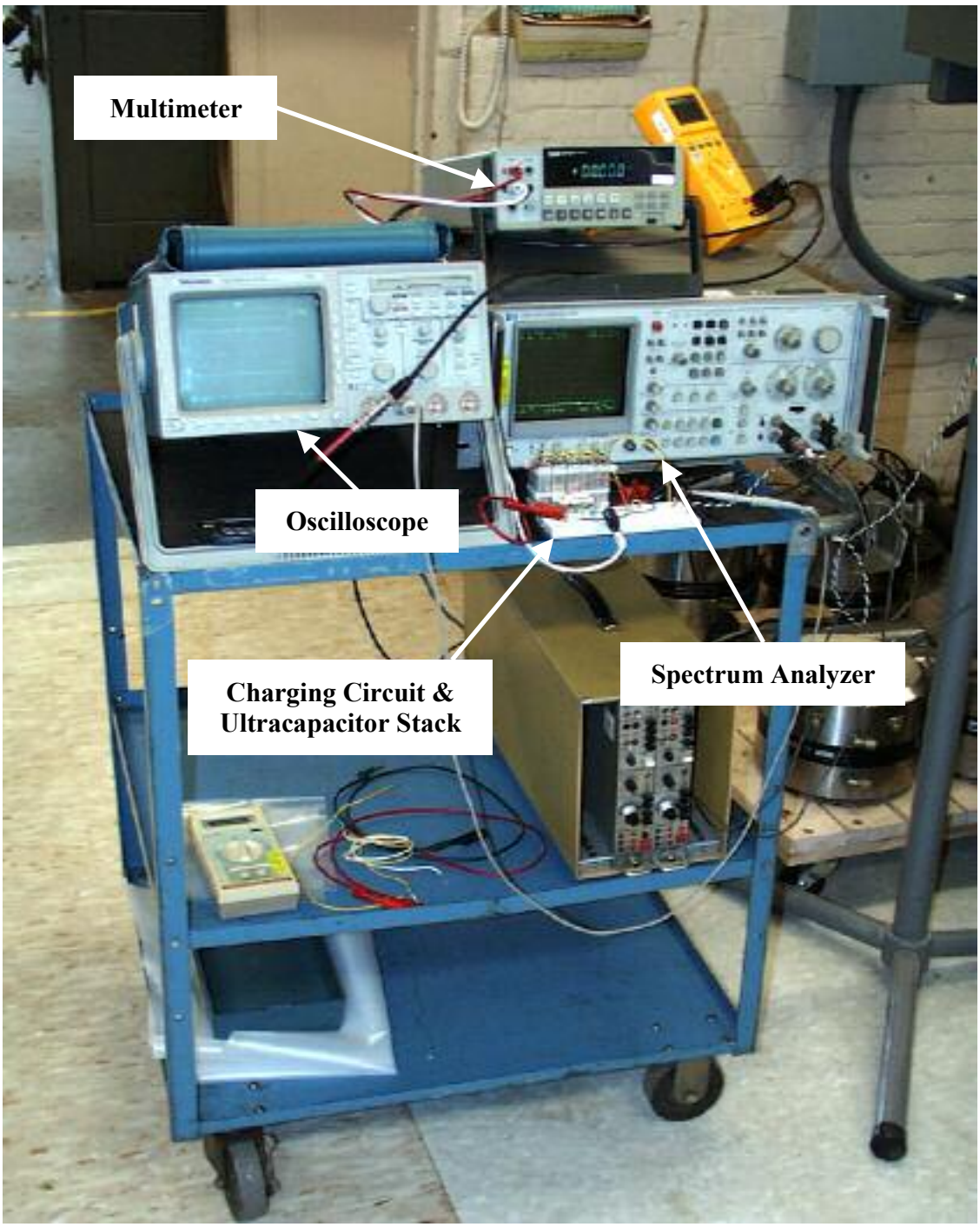


**Figure 8.13**: Data Acquisition Equipment for the Power Scavenging Experiment

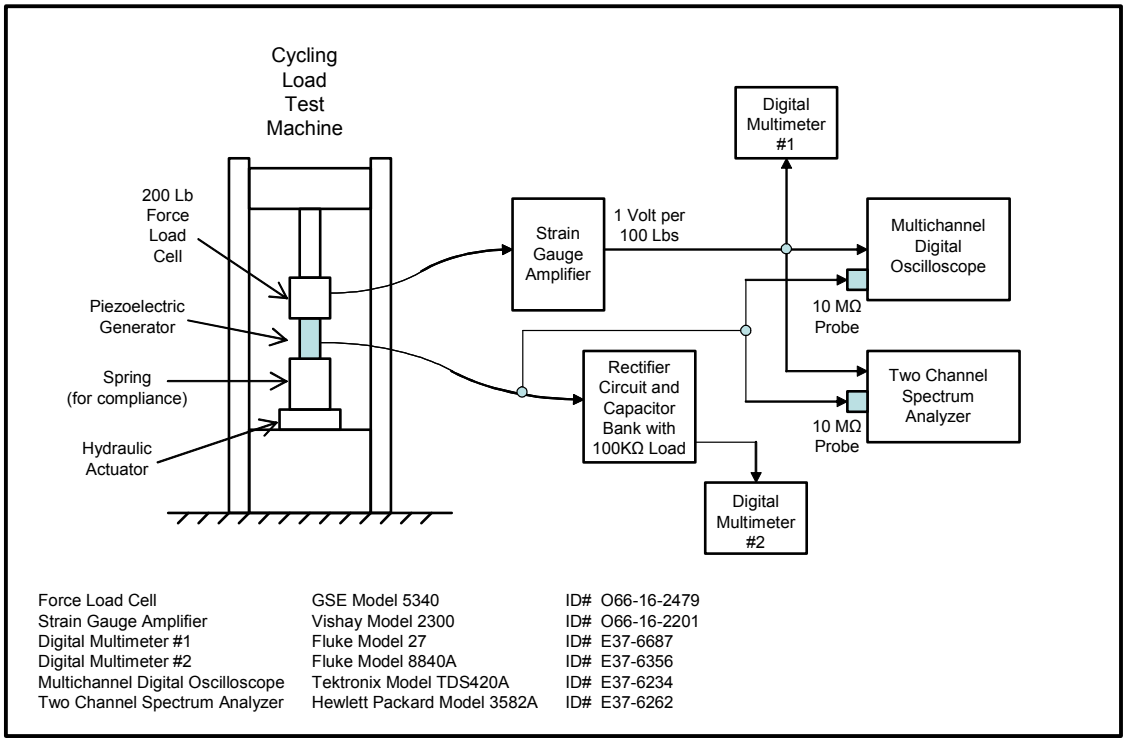


| | | |
|---|---|---|
| Force Load Cell | GSE Model 5340 | ID# O66-16-2479 |
| Strain Gauge Amplifier | Vishay Model 2300 | ID# O66-16-2201 |
| Digital Multimeter #1 | Fluke Model 27 | ID# E37-6687 |
| Digital Multimeter #2 | Fluke Model 8840A | ID# E37-6356 |
| Multichannel Digital Oscilloscope | Tektronix Model TDS420A | ID# E37-6234 |
| Two Channel Spectrum Analyzer | Hewlett Packard Model 3582A | ID# E37-6262 |

**Figure 8.14**: Schematic of the Equipment used in the Power Scavenging Experiment

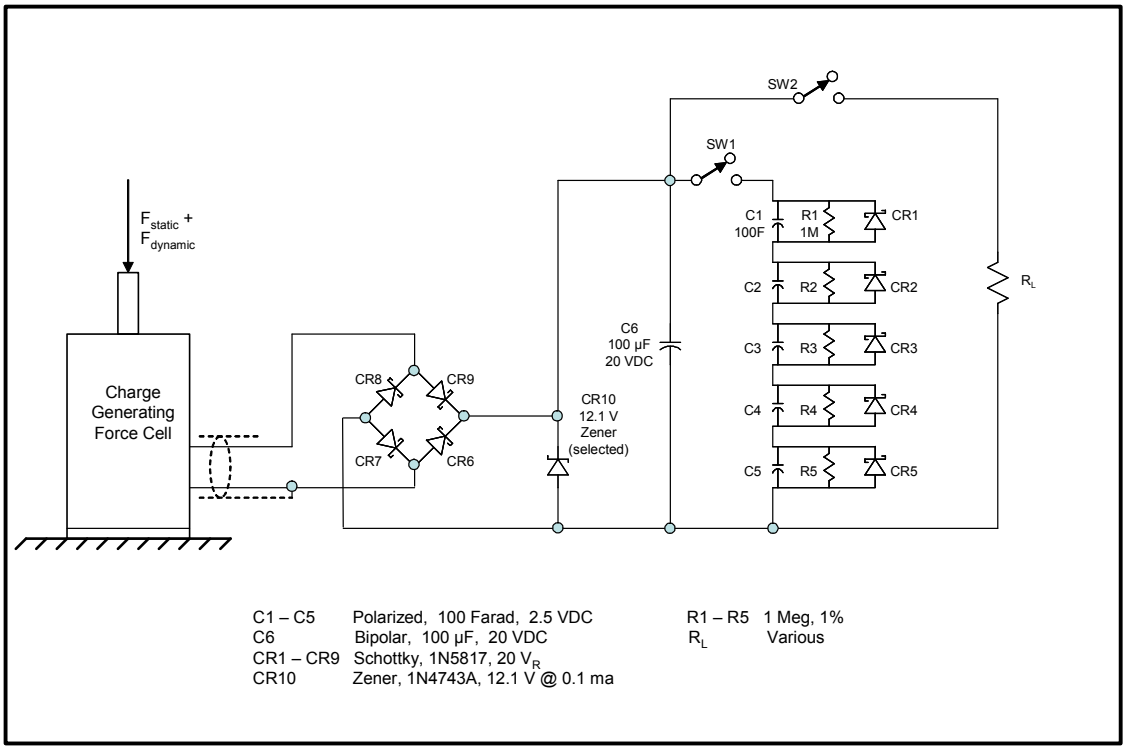


| | | | |
|---|---|---|---|
| C1 – C5 | Polarized, 100 Farad, 2.5 VDC | R1 – R5 | 1 Meg, 1% |
| C6 | Bipolar, 100 µF, 20 VDC | $R_L$ | Various |
| CR1 – CR9 | Schottky, 1N5817, 20 $V_R$ | | |
| CR10 | Zener, 1N4743A, 12.1 V @ 0.1 ma | | |

**Figure 8.15**: Schematic of the Charging Circuit for the PSG Test

Since the frequency and force actually applied to the PSG in a shipboard application could vary depending on the source of the applied load, a simulation was performed in Simulink® (and verified analytically) to determine what force would be applied to the PSG if it was mounted between the base of the isolation system and a 10 Hz deck oscillating with an amplitude of 0.002 in. as shown in Figure 8.16.

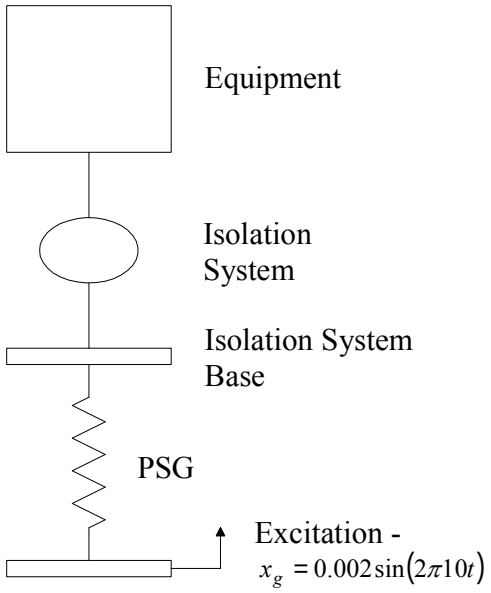


**Figure 8.16**: Model Used to Determine Force in the PSG

This is conservative as more energy would be available to apply to the generator if it was mounted between the vibrating equipment and the isolation system, or if it was mounted on a higher frequency deck. The result of the simulation suggested that a dynamic force of 20 lbf peak could be achieved by installing the PSG between the base of the isolation system and the 10 Hz deck using the deck motion as an input. If it can be shown that sufficient power can be generated using this method then by comparison more power could be generated by installing the PSG between the vibrating equipment and the isolation system. Therefore, the load used for the design of the PSG was a sinusoid of amplitude 20 lbf at a frequency of 10 Hz. The PSG was then designed and built by Kinetic Ceramics, Inc. to generate a minimum of 0.1 mA of current at 12 V when subjected to this input.

To quantify the performance of the PSG a series of tests were performed at various frequencies and force levels. In the following tests the output from the PSG was rectified using a full-wave bridge rectifier and the resulting DC voltage was used to charge a 100 μF capacitor bank. This was done to minimize the amount of time required to reach full charge as the 20 F ultracapacitor stack would take considerably more time to charge.

The effect of the variation in input frequency on the output voltage was explored by applying a sinusoidal force of 20 lbf amplitude at frequencies of 2, 4, 6, 8, 10, 12 14 and 16 Hz and recording the normalized DC output voltage into a 100 kΩ load. The results are plotted in Figure 8.17. From the figure it can be seen that the output voltage increases with increasing input frequency and that this relationship is not linear. In fact it can be shown that the output voltage asymptotically approaches a constant output voltage at which point increases in drive frequency produce no further increase in output voltage.

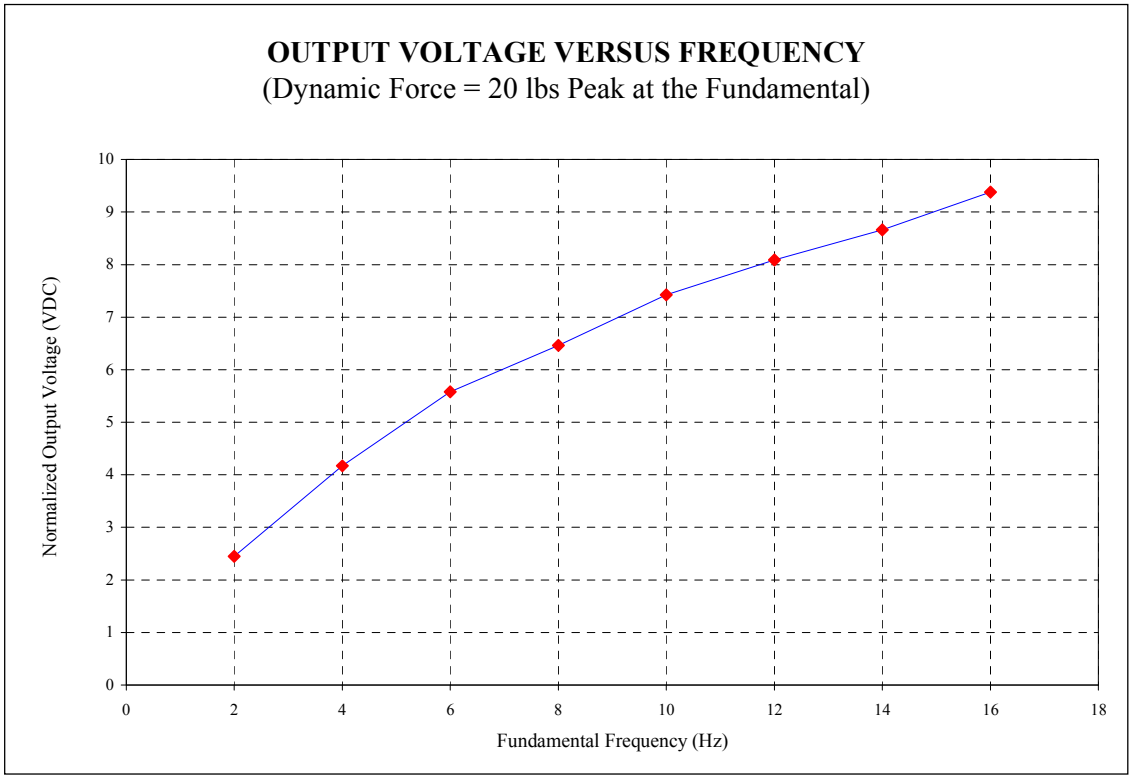


**Figure 8.17**: Output Voltage versus Frequency for the Piezoelectric Stack Generator

To determine what effect increases in applied force have on the output voltage a series of tests were performed at force levels of 5, 10, 15, 20 and 25 lbf and frequencies of 1, 5, 10 and 15 Hz. As can be seen in Figure 8.18 the relationship between input force and DC output voltage is essentially linear. Other parameters being equal, an increase in dynamic force results in a linear increase in voltage. This relationship tended to deviate from a linear relationship at an input frequency of 15 Hz, which was unexpected, but the trend is still nearly linear. There is obviously some other phenomenon present that is not being taken into consideration. One possible explanation is that the true peak force amplitude was greater than that obtained from the spectrum analyzer and the input force tended to deviate more from a true sinusoid at higher frequencies.

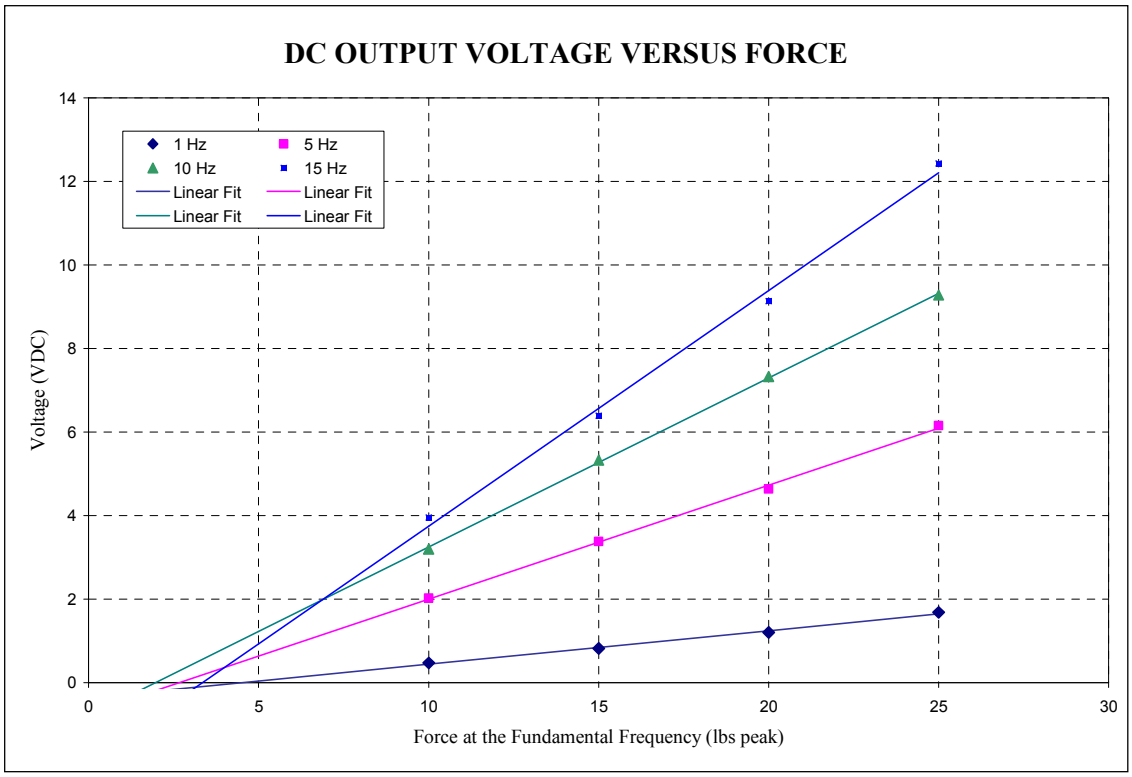


**Figure 8.18**: Output Voltage versus Force for the Piezoelectric Stack Generator

In addition to the DC tests the RMS AC output of the PSG was measured with various loads, forces and frequencies. The results for the design force amplitude of 20 lbf and design frequency of 10 Hz into a 5 MΩ load are shown in Table 8.1. The results for

the design force amplitude of 20 lbf and design frequency of 10 Hz into a 10 kΩ load are shown in Table 8.2.

| **Frequency** (Hz) | **Force** (lbf) | | | |
|---|---|---|---|---|
| | **10** | **15** | **20** | **25** |
| 1 | 4.85 | 7.48 | 10.2 | 13.3 |
| 5 | 4.79 | 7.73 | 10.6 | 13.5 |
| 10 | 4.97 | 7.83 | 10.6 | 13.2 |
| 15 | 5.14 | 7.88 | 11.0 | 14.4 |

**Table 8.1**: RMS AC Voltage (Volts) from PSG into a 5 MΩ Load

| **Frequency** (Hz) | **Force** (lbf) | | | |
|---|---|---|---|---|
| | **10** | **15** | **20** | **25** |
| 1 | 0.073 | 0.120 | 0.170 | 0.228 |
| 5 | 0.362 | 0.595 | 0.840 | 1.110 |
| 10 | 0.734 | 1.180 | 1.630 | 2.100 |
| 15 | 1.120 | 1.750 | 2.490 | 3.360 |

**Table 8.2**: RMS AC Voltage (Volts) from PSG into a 10 kΩ Load

A final test was performed by charging the actual ultracapacitor stack using the PSG as a charge source. The input to the PSG was the design force of 20 lbf peak at a frequency of 10 Hz. The test was allowed to run for 3 days before being terminated due to time constraints. The resulting charging curve is shown in Figure 8.19. Also plotted in the figure is an analytical exponential which fits the data very well. It would be expected that if the test was allowed to run longer that the actual charging curve would begin to deviate from the analytical exponential after approximately 170 hours of charge time as was seen in Figure 8.8.

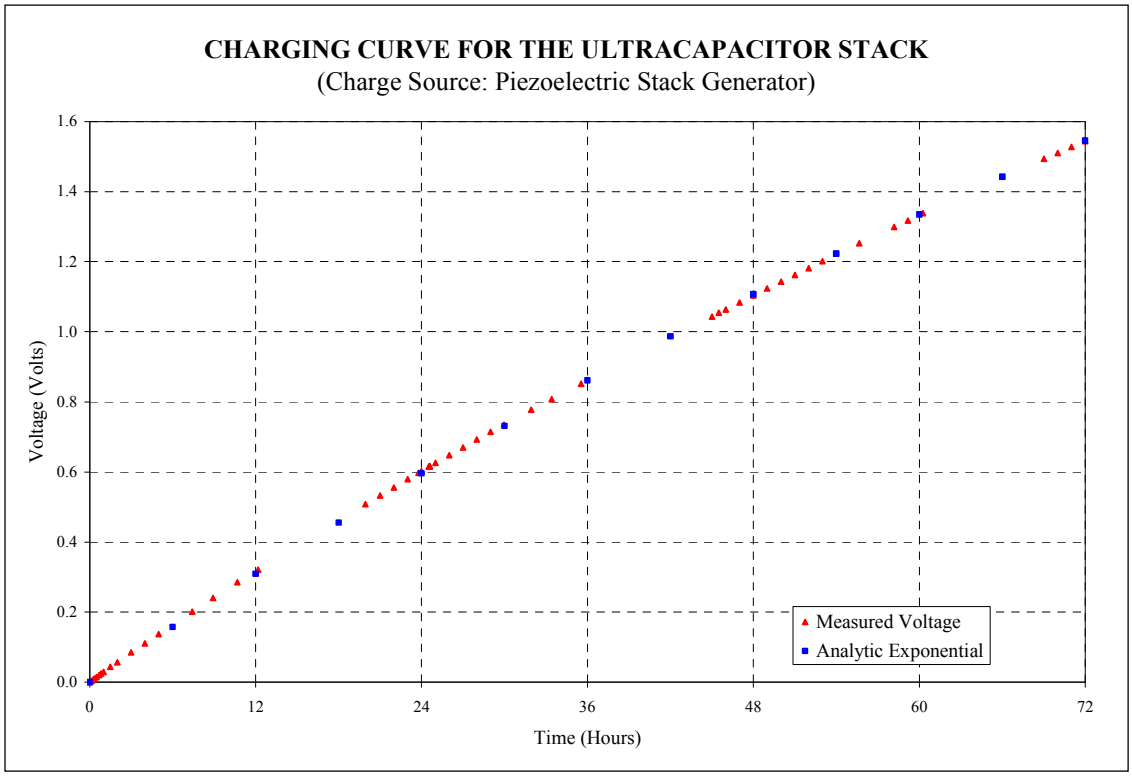


**Figure 8.19**: Charging Curve for the Ultracapacitor with PSG as the Charge Source

To accurately model the PSG installed in a system it is necessary to know its force-deflection behavior. To determine the force-deflection behavior of the PSG it was placed into a load test machine and loaded at increments of 200, 400, 600, 800 and 1000 lbf. At each force increment the deflection of the PSG and its capacitance were measured and recorded. The resulting force deflection plot is shown in Figure 8.20.

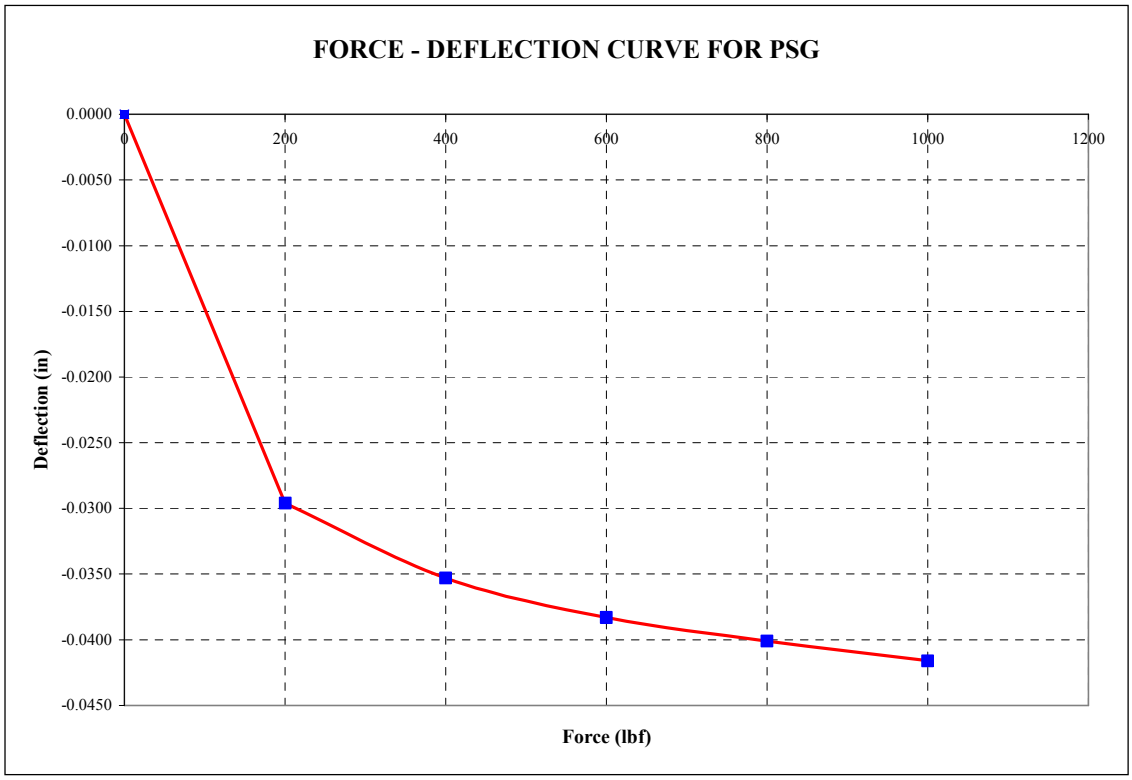


**Figure 8.20**: Force – Deflection Plot for the PSG

Note that there is an offset in the force-deflection curve that appears to be due to some mechanical property inherent to the device. After a significant load was applied to the PSG the force-deflection curve smoothed out, but was nonlinear. However, it did appear that the force-deflection behavior was very nearly linear around the design load of 1000 lb.

Also measured and recorded was the capacitance of the PSG at various loads as shown in Figure 8.21. The capacitance tended to increase with increasing load with the exception of a slight offset at 800 lbf which could not be explained. Since larger capacitance results in an increase in the charge output of the device, it is desirable to operate the device with the largest allowable preload. In this experiment all of the tests were performed with a preload of 100 lbf. In hindsight the design preload of 1000 lbf should have been used to increase the efficiency of the PSG. Following this test series the PSG was disassembled in an attempt to determine what was causing the offsets in

both force-deflection and force capacitance. Nothing was visible in the device to indicate what was causing these offsets.

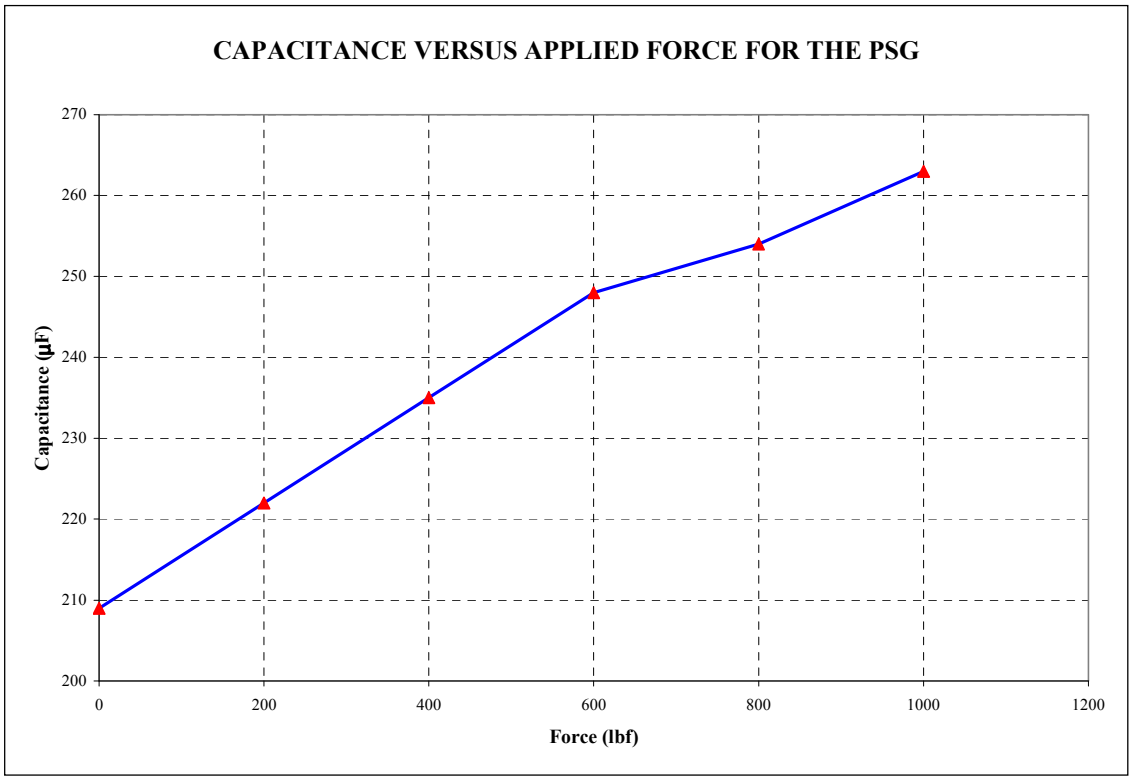


**Figure 8.21**: Load – Capacitance Behavior of the PSG

## 8.7 Chapter Summary

To utilize the subject isolation system on existing ships requires the addition of a power source and the associated cabling necessary to bring power to the device. It would be very desirable if the isolation was simply a drop-in replacement for the existing passive systems. If semi-active isolation systems are to be backfit on existing ships it would be beneficial to develop a system that could generate and store its own power. This was the goal of this power scavenging work. Of course this is not necessarily as big a problem on new construction ships as the additional power systems can be designed in from the beginning.

The results of the power scavenging experiment suggests that sufficient energy could be generated with a suitable PSG(s) and stored in an ultracapacitor stack(s) to power the MRAM through several shock events. A more efficient storage device could conceivably be developed by utilizing a DC-DC converter to use more of the available energy stored in the ultracapacitor stack. Furthermore, the use of a DC-DC converter would allow the required capacitance to be optimized. Minimizing the capacitance to just the value needed to power the MRAM through the number of events deemed necessary could considerably reduce the time required to recharge the capacitor stack. Pre-charging the capacitors prior to installation would also result in less required charging time than charging them from 0 Volts. The PSG could then be used to trickle charge the capacitors thus keeping them "topped off". It should be noted that some constant current must be generated to power the controller in its dormant mode. Using capacitors with minimum leakage current also is desirable as any charge lost through leakage must be replaced though recharging by the PSG.